NANOSCALE ELECTROSTATIC ACTUATORS IN LIQUID ELECTROLYTES:

ANALYSIS AND EXPERIMENT

A Dissertation

by

DOYOUNG KIM

Submitted to the Office of Graduate Studies of
Texas A&M University
in partial fulfillment of the requirements for the degree of

DOCTOR OF PHILOSOPHY

December 2005

Major Subject: Aerospace Engineering

NANOSCALE ELECTROSTATIC ACTUATORS IN LIQUID ELECTROLYTES:

ANALYSIS AND EXPERIMENT

A Dissertation

by

DOYOUNG KIM

Submitted to the Office of Graduate Studies of
Texas A&M University
in partial fulfillment of the requirements for the degree of

DOCTOR OF PHILOSOPHY

Approved by:

Chair of Committee,   James G. Boyd
Committee Members,   John D. Whitcomb
                                   John E. Hurtado
                                   Won-jong Kim
Head of Department,   Helen L. Reed

December 2005

Major Subject: Aerospace Engineering

ABSTRACT

Nanoscale Electrostatic Actuators in Liquid Electrolytes:

Analysis and Experiment. (December 2005)

Doyoung Kim, B.S.; M.S., Korea University, Seoul, Korea

Chair of Advisory Committee: Dr. James G. Boyd

The objective of this dissertation is to analytically model a parallel plate electrostatic actuator operating in a liquid electrolyte and experimentally verify the analysis.

The model assumes the system remains in thermodynamic equilibrium during actuation, which enables the ion mass balance equations and Guass' Law to be combined into the Poisson-Boltzmann equation. The governing equations also include the linear momentum equation including the following forces: the electric force, the osmotic force, the spring force, the viscous damping force, and the van der Waals force. Equations are also derived for the energy stored in the actuator. The analytical results emphasize the stored energy at mechanical equilibrium and the voltage versus electrode separation behavior including the instability. The analytical results predict that the system may not be a good actuator because the displacement has a very limited stable range, although the actuator would be suitable for bistable applications.

The experiment consisted of a fixed flat gold electrode and a movable gold electrode consisting of a gold sphere several micrometers in diameter mounted on the

end of an Atomic Force Microscope (AFM) cantilever, which serves as the spring. The electrodes were separated by approximately 100nm of 1mM NaCl aqueous solution.

The analytical results were not verified by the experiment. Relative to the analysis, the experiments did not show distinct critical points, and the experiments showed less electrode separation for a given applied electric potential. The experiments did show points at which the electrode separation versus electric potential rapidly changed slope, which may be instability points.

It is suggested that this phenomenon may be due to coalesced gas bubbles on hydrophobic regions of the electrode surfaces, which are not included in the model. Although clean gold surfaces are hydrophilic, gold surfaces may become hydrophobic due to impurities.

To my wife, two sons, my parents, and God.

ACKNOWLEDGMENTS

First of all, I would like to thank my research advisor, Dr. James G. Boyd, for his consistent support and encouragement for years. It was very fortunate for me to meet him when I came to Texas A&M University and I cannot forget the excitement when he suggested this challenging project. I admire his competence throughout continuum theory, electrical, electrochemical and mechanical engineering disciplines. Whenever I had a problem and whatever it was, he gave me a right way and advice to solve it. I sincerely would like to give my best regards to him.

I am grateful to Dr. Kim for his serving on my doctoral committee and giving me lots of advice about my research and private things. He taught me much about electromagnetic theory and electromechanical system analysis. Dr. John D. Whitcomb and Dr. John E. Hurtado have shown their great interest since the earliest stage of my doctoral work. I appreciate their taking time to read my dissertation and giving me precious comments.

I would like to thank Dr. William Lackowski, the manager of the MCF (Materials Characterization Facility), who gave me a lot of knowledge about electrochemical and AFM experiments. I thank everyone else in MEMS/NEMS lab and MCF lab for the friendly environment they created.

My special appreciation goes to my beloved wife, Jungnam Kwon, and my children, Youngsoo and Youngseok, for their love, patience, and encouragement. I can never

thank my wife enough for her patience, understanding and prayer to God. She has always been a great friend and wonderful counselor of mine.

I am deeply grateful to my father, Jongsun Kim, my mother, Youngsoon Choi, and my sister, Sun Kim, for their endless love and support. Also, I would like to thank Jungnam's parents, Ohkun Kwon and Minja Chang. Without their love and support, this work would not have been possible.

Finally, I would like to thank God.

TABLE OF CONTENTS

LIST OF FIGURES

Page

LIST OF TABLES

I. INTRODUCTION

A. *Background*

Actuators are devices that convert nonmechanical energy into mechanical energy. Types of nonmechanical energy include electric, magnetic, chemical, and thermal energy. Electrostatic actuators are the most common type of actuator in Micro Electromechanical Systems (MEMS), for three reasons: 1) They are easy to manufacture using standard surface micromachining methods; 2) They are easily controlled and can be actuated at very high frequencies; and 3) The electrostatic force per unit area increases with decreasing size. The electrostatic force acting between two parallel plates of a capacitor is given by

$$\text{Force} = -\frac{1}{2}\frac{\varepsilon\varepsilon_0 A}{h^2}\psi^2 \tag{1}$$

where A is the electrode area, ε is the permittivity of the material between the two electrodes, h is the distance between the two electrodes, and ψ is the electric potential difference between the two electrodes.

This dissertation follows the style and format of *Journal of Microelectromechanical Systems*.

Note that the electrostatic force per unit area is proportional to the inverse of the square of the distance (h^2) between the two electrodes. Standard surface micromachining technologies now enable the distance h to be approximately one micrometer.

Electrostatic MEMS actuators are usually made in one of two configurations: the parallel plate actuator and the comb drive actuator.

MEMS comb drive actuators (Fig. 1) are used in rate gyroscopes [1], accelerometers [2], rotating mirrors for scanners in Micro Electrooptomechanical Systems (MOEMS) [3], and tunable capacitors [4].
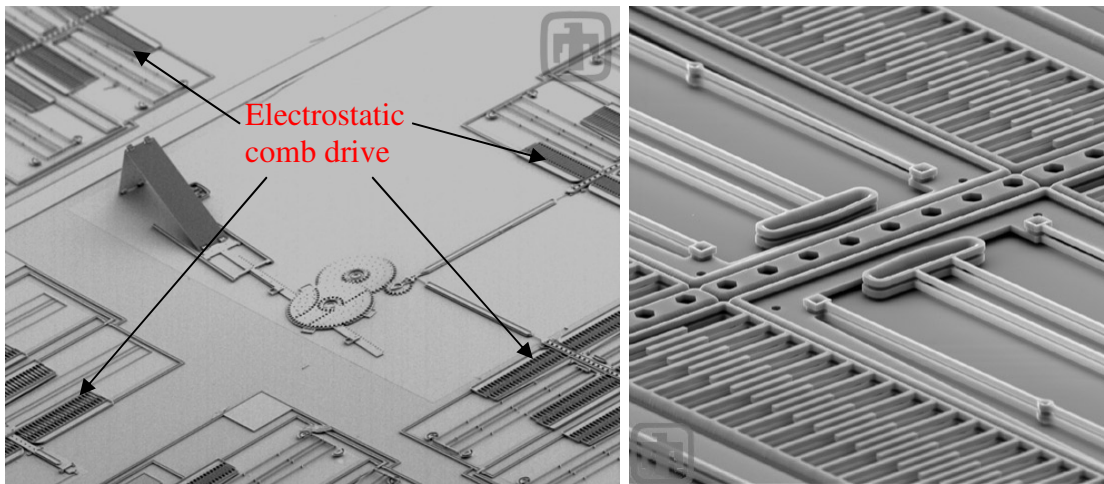
Fig. 1. Electrostatic comb drive from the Sandia National Laboratory [5].

MEMS parallel plate actuators are the most common method of actuating micromirrors that are used in optical scanners, including scanning confocal microscopes [6]. Economically, the largest success for parallel plate actuators is in the digital light processing chip made by Texas Instruments (Fig. 2), which is used in projection displays and is expected to become the industry standard for high definition televisions [7].
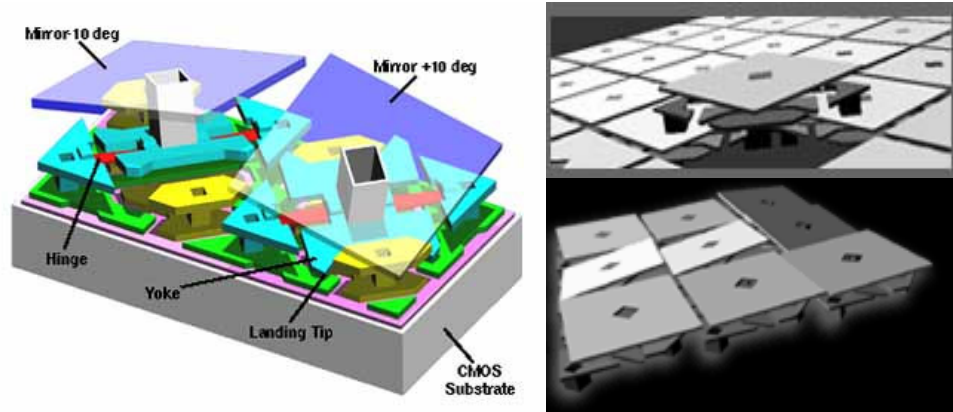
Fig. 2. DLP (Digital Light Processing) from Texas Instruments [8].

The parallel plate actuators undergo a "snap-down" or "pull-in" instability in which the two electrodes spontaneously come into contact when the distance between the two actuators is less than 2/3 of the initial distance. This instability occurs because the force given by equation (1) results in two equilibrium values of *h* when one of the parallel plate electrodes is fixed and the other electrode is connected to a linear spring. The most recent and rigorous study of these "pull-in" instabilities is provided in the sequence of papers by Degani [9]-[13].

A schematic of a parallel plate electrostatic actuator is shown in Fig. 3. When a potential difference ψ is applied between the two electrodes, the spring of constant *K* is stretched downward from its initial distance h_0 to its current distance of *h(t)*.
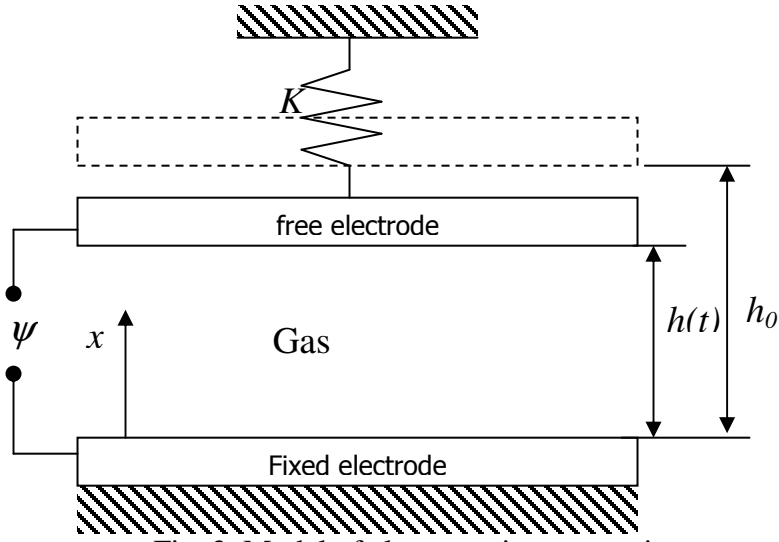
Fig. 3. Model of electrostatic actuator in gas.

The mechanical equilibrium equation is given by

$$0 = K(h_o - h) - \frac{1}{2}\frac{\varepsilon\varepsilon_0 A}{h^2}\psi^2 .$$

(2)

Fig. 4 shows the elastic spring force and electrostatic force vs. electrode separation, h. In Fig. 4, when the applied potentials are below the critical potential ($\psi < \psi_{cri}$), there are two equilibrium positions of the free electrode. The one near the initial separation is the stable equilibrium position and the other is unstable. If the separation h is decreased below the stable equilibrium point (for a fixed potential), then the restoring spring force is greater than the attractive electric force. However, if the separation is decreased below the unstable equilibrium point (for a fixed potential), then the restoring force is less than the attractive force. At the critical potential, only one intersection exists, and it is critical

point. When the applied potential is above the critical potential, the attractive electrostatic force is always greater than the elastic spring force and the free electrode is in contact with fixed electrode.
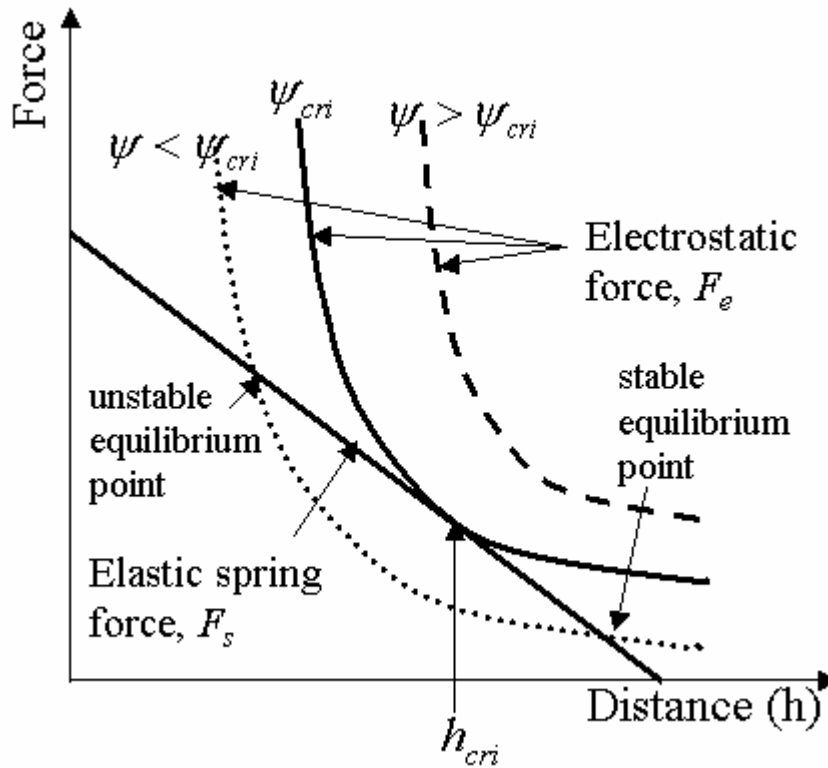
Fig. 4. Elastic spring force and electrostatic force vs. distance of electrostatic actuator in the gas.

The equilibrium equation yields the electric potential as a function of the electrode separation as

$$\psi(h) = \sqrt{\frac{2K}{\varepsilon\varepsilon_0 A} h^2 (h_0 - h)} \tag{3}$$

which is plotted in Fig. 5.
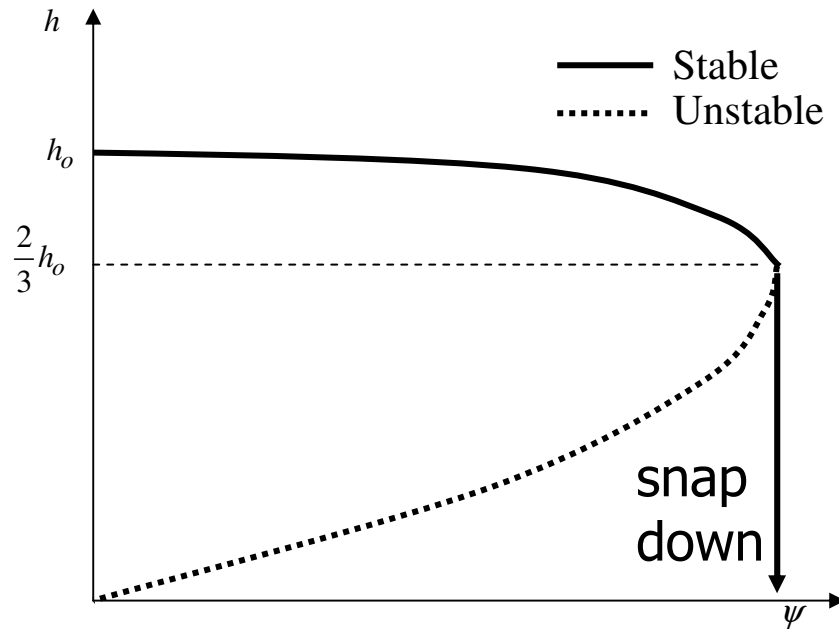
Fig. 5. Equilibrium position (h) of the free electrode vs. external potential (ψ) for a parallel plate electrostatic actuator.

Fig. 6 shows the curves of the potential energy for the electromechanical device in gas with elastic spring force versus separation. The potential energy of the electromechanical system in gas is

$$U(h) = \int_{h}^{h_0} \left(F_s(h') - F_e(h') \right) dh'. \tag{4}$$
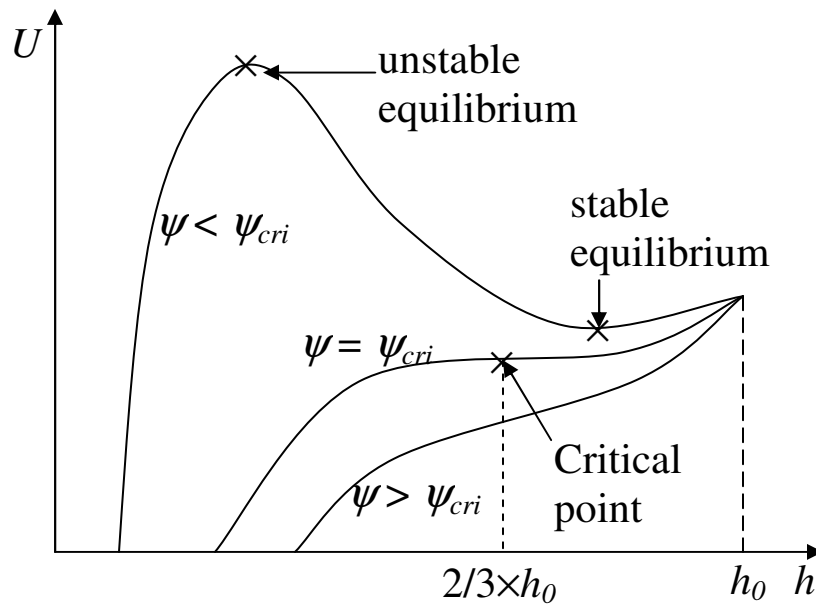
Fig. 6. Potential energy (*U*) vs. separation (*h*).

The two intersections of the elastic spring force and electrostatic force below the critical pull-in potential in Fig. 5 correspond to the maximum and minimum point in the potential energy curve as shown in Fig. 6. The minimum point of these two equilibrium points in potential energy curve of Fig. 6 is the stable equilibrium, while the maximum point is the unstable equilibrium. Potential energy curves of the voltage above the critical pull-in potential have no maximum nor minimum point.

Actuators similar to parallel plate actuators have been extended to Nano Electromechanical Systems (NEMS). Kim in 1999 "nanotweezers" NEMS based on carbon nanotubes for manipulation and interrogation of nano-structures. The tweezers have two carbon nanotubes attached to a glass rod as electrodes. The potential difference

between the two carbon nanotube tweezer arms produces an attractive electrostatic force that can overcome the elastic restoring force of the carbon nanotubes in closing the tweezers. Through experiment with carbon nanotubes (length = 5 μm, nanotube diameter = 45 nm, separation of two carbon nanotubes = 1 μm), the tweezer arms suddenly closed as the voltage was increased further to 8.5 V. An analytical approach with elastic energy and electrostatic energy was carried out to understand the response and sudden closure of the nanotweezers. They demonstrated the nanotweezer manipulation of polystyrene nanoclusters containing fluorescent dye molecules [14]. Akita in 2001 did similar experiments and analysis for nanotweezers consisting of carbon nanotubes in an AFM (Atomic Force Microscope). Two nanotube arms were fixed at the most appropriate position on the silicon cantilever tips used as the substratum of the nanotweezers for the AFM. Their length was 2.5 μm and the separation between their tips was 780 nm. They determined a pull-in voltage (or critical voltage) of 4.5 V at 500 nm separation [15]. Dequesnes in 2002 analytically studied the pull-in instability of carbon nanotube switches, using the parameterized continuum models for three coupled energy domains: the elastic energy domain, the electrostatic energy domain, and the van der Waals energy domain [16].

Electrostatic actuators are typically used in gas or vacuum. Evidently, there has been little attempt to develop MEMS and NEMS actuators to operate in liquids. Sounart and Michalske (2003) did test a MEMS comb drive actuator in various liquids, including ethylene glycol, HeOH, isopropyl alcohol, EtOH, EG, H2O, and MeNO. Applied DC voltages were below the threshold that initiates electrolysis and electrochemical

reactions. It was demonstrated that minute concentrations of ionic impurities were sufficient to disable the actuators. However, when an AC voltage was applied, the actuators worked above a critical frequency that varied by four orders of magnitude among the liquids tested [17].

A logical application for MEMS and NEMS actuators is in body fluids, which are typically 0.2 M ionic solutions, mainly NaCl or KCl. The design of nano electromechanical machines – such as actuators, switches, tweezers, valves, gears, linkages, etc. – that operate in liquid electrolytes must account for osmotic and electric forces due to the ions, as well as damping forces due to the liquids.

In addition to biomedical applications, ionic liquid applications of MEMS and NEMS actuators may include fuel cells, batteries, supercapacitors, filters, electro-osmotic pumping, storage of hydrogen, electroactive polymer actuators, electroosmosis, and electrocapillarity.

Nanoscale electric and osmotic forces have been studied in detail in biochemistry and electrochemistry. But there has been almost no continuum mechanics effort to understand the dynamics of NEMS in liquid electrolytes, particularly with the motivation to develop nano scale machines.

B. *Objective and organization of the dissertation*

The **<u>objective</u>** of this dissertation is to analytically model a parallel plate electrostatic actuator operating in a liquid electrolyte and experimentally verify the analysis.

There is no separate section for the literature review. Instead, the relevant literature is cited as needed within each section.

The analytical model is presented in section II. A parallel plate actuator is chosen because it is easier to experimentally test the parallel configuration than the comb drive. The model assumes the system remains in thermodynamic equilibrium during actuation, which amounts to a quasi-static analysis with respect to the diffusion of ions. The governing equations include the ion mass balance and Gauss' law combined in the Poisson-Boltzman equation, and the linear momentum equation including the following forces: the electric force, the osmotic force, the spring force, the viscous damping force, and the van der Waals force. Equations are also derived for the energy stored in the actuator. The analytical results are presented in section II, with an emphasis on the voltage-separation behavior, the instability, and the stored energy at mechanical equilibrium.

The experimental procedure and background are described in section III A, B and the experimental results are given in section III C and discussed in section III D.

Finally, conclusions and recommendations for future work are made in section IV.

C. *Contribution of the dissertation*

The contribution of this dissertation is to bring together the work of the colloidal science community and the MEMS and NEMS electrostatic actuator community.

As discussed in various sections of this dissertation, researchers in colloidal science have analytically modeled the electric, osmotic, and van der Waals force between

surfaces in liquids, but these studies did not include the spring force that is necessary to make an actuator.

Researchers in the MEMS and NEMS actuator communities have analytically modeled the electric, van der Waals, and spring force on actuators, but their analyses were for air or vacuum and did not include the effects of ions, which modify the electric field and introduce the osmotic force.

Experimentalists in the colloidal science community have measured the force versus separation curves between surfaces in liquid electrolytes, but to our knowledge, no one has experimentally determined the electric potential versus separation curves.

II. ANALYSIS

A. Analytical model and governing equations
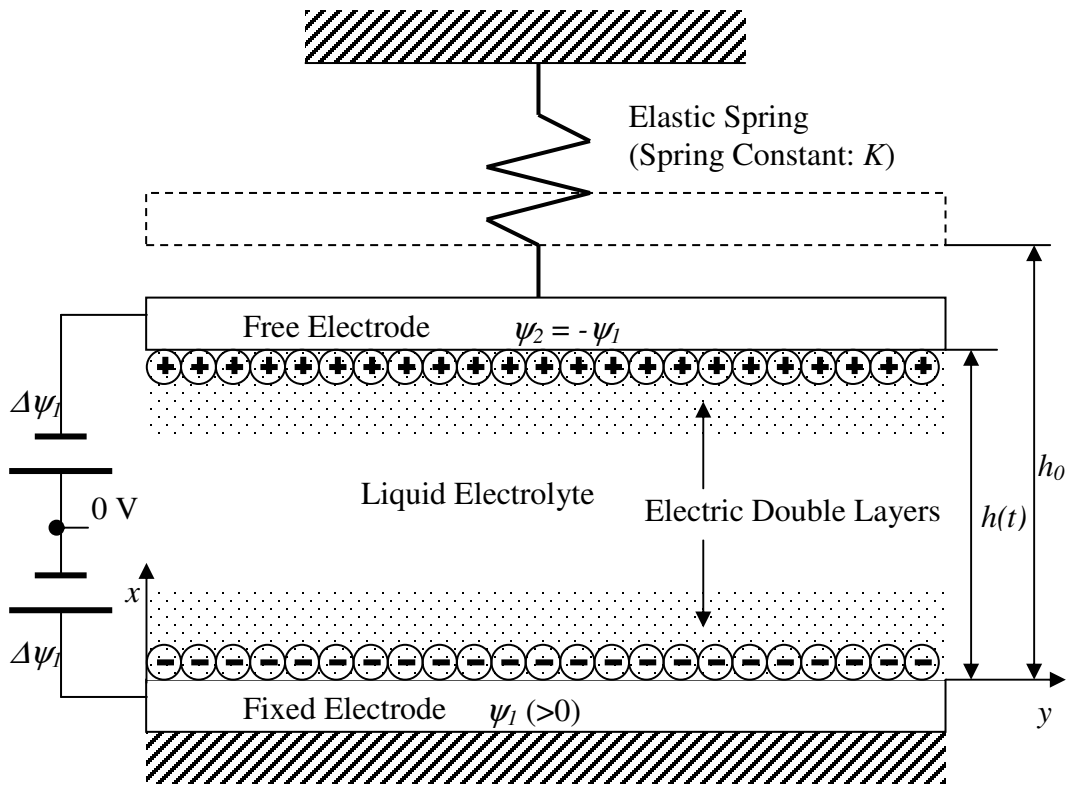
Fig. 7. Model of Nano Electromechanical System (NEMS) in liquid electrolyte.

An electrostatic actuator consists of two or more electrodes, one of which is free to move and connected to a spring which is fixed at its opposite end. Fig. 7 depicts the actuator model used in this research. The other electrode is fixed. The spring returns the actuator to its original position after actuation. Part of the spring constant can be

attributed to the external load against which the actuator is moving. Alternatively, an external load could be applied directly to the free electrode. In the relevant literature, there is usually no external load applied to the free electrode of the actuator model. The electrodes are assumed to be planar and parallel. The electrodes are separated by a distance $h(t)$, where t is time. The initial separation is $h(0)$. The volume between the two electrodes is filled with a liquid electrolyte, i.e. a liquid that does not conduct electricity by electronic conduction, but contains ions that can diffuse. The bulk electrolyte, far from the electrodes, is assumed to be at a potential of 0 volts. The fixed electrode is at a potential of ψ_1 (>0), and the free electrode is at a potential of $-\psi_1$. The accumulation of ions of a given charge near (within a few nanometers) of an electrode is called a "double layer".

The following manipulation of the governing equations, including the derivation of the Poisson-Boltzmann equation, can be found in standard texts on electrochemistry [18] and colloidal science [19].

Mass transfer between the electrodes occurs due to diffusion, migration (ion drift), and convection. The flux J_i^s of species s is given by

$$J_i^s = -\left(\frac{n^s D^s}{RT}\right)\nabla_i \mu^s + n^s V_i \tag{5}$$

where n^s, μ^s, and D^s are the concentration, electrochemical potential, and diffusion coefficient of species s, V_i is the velocity of the mass point in the fluid, R is the gas

constant, and T is the absolute temperature. For the case of an ideal solution, the electrochemical potential is given by

$$\mu^s = \mu^{s0} + RT \ln n^s + z^s F \psi \tag{6}$$

where μ^{s0} is chemical potential at standard state, z^s is the valence of species s, F is the Faraday constant, and ψ is the electric potential. Finally the flux J_i^s of an ion of species s in electrolyte is governed by diffusion, drift, and convection like following equation,

$$J_i^s = D^s \left(-\nabla_i n^s \right) + D^s \frac{z^s F}{RT} \left(-\nabla_i \psi \right) n^s + n^s V_i \tag{7}$$

where the first term on the right hand side represents ion diffusion arising from a concentration gradient, the second term represents migration (ion drift, conduction) arising from an electric field, and the third term represents ion convection arising from motion of the bulk solution.

The balance of species can be expressed as:

$$\frac{\partial n^s}{\partial t} + \nabla_i J_i^s = P^s \tag{8}$$

where n^s is local concentration of species s and P^s is the molar rate of the production per unit volume due to the chemical reactions. In this research it is assumed that there are no chemical reactions, so $P^s = 0$, and (8)

$$\frac{\partial n^s}{\partial t} + \nabla_i J_i^s = 0 . \tag{9}$$

Gauss' law is given by

$$\nabla_i D_i = \rho^f \tag{10}$$

where D_i is the electric displacement and ρ^f is the free charge density. In electrostatics the electric field E_i is given by the electric potential as

$$E_i = -\nabla_i \psi \tag{11}$$

The electric permittivity ε is the material property that relates the electric displacement to the electric field:

$$D_i = \varepsilon \varepsilon_0 E_i \tag{12}$$

where the medium is assumed to be isotropic. The equations can be combined to yield, for a homogeneous medium,

$$\varepsilon \varepsilon_0 \nabla_i \nabla_i \psi = -\rho^f \tag{13}$$

The free charge density arising from N ionic species can be expressed as

$$\rho^f = \sum_1^N e z^N n^N \tag{14}$$

With (13) and (14), Poisson equation for the excess charge density can be expressed as

$$\varepsilon \nabla_i \nabla_i \psi = -\sum_1^N e z^N n^N \tag{15}$$

Assuming that convection vanishes, using the Nernst-Planck equation (7), the conservation of mass (9) can be expressed as:

$$\frac{\partial n^s}{\partial t} = -\nabla_i J_i^s = \nabla_i \left(D^s \nabla_i n^s + D^s \frac{z^s F}{RT} n^s \nabla_i \psi \right). \tag{16}$$

We will limit the diffusion analysis to the case where the electrolyte is symmetrical, i.e., cations and anions have the same valence between two infinite flat plates. Furthermore, due to the symmetry of the problem, there is diffusion only in the x direction, i.e. normal to the plane of the electrodes:

$$\varepsilon\varepsilon_0 \frac{\partial^2 \psi}{\partial x^2} = -ezn^+ + ezn^- \tag{17}$$

$$\frac{\partial n^+}{\partial t} = D^+ \frac{\partial}{\partial x}\left(\frac{\partial n^+}{\partial x} + \frac{zF}{RT}n^+ \frac{\partial \psi}{\partial x}\right) \tag{18}$$

$$\frac{\partial n^-}{\partial t} = D^- \frac{\partial}{\partial x}\left(\frac{\partial n^-}{\partial x} - \frac{zF}{RT}n^- \frac{\partial \psi}{\partial x}\right) \tag{19}$$

where n^+ is ion concentration with positive valence and n^- is ion concentration with negative valence. Equations (17), (18), and (19) are to be solved for the electric potential ψ and the ion concentrations n^+ and n^- as functions of time and space. The governing equations are completed by the three initial conditions ($\psi(t = 0, x)$, $n^+(t = 0, x)$, $n^-(t = 0, x)$) and the six boundary conditions $\psi(t, x = 0)$, $\psi(t, x = h)$, $J^+(t, x = 0)$, $J^+(t, x = h)$, $J^-(t, x = 0)$, $J^-(t, x = h)$.

1) Thermodynamic equilibrium

In thermodynamic equilibrium, the gradient of the electrochemical potential vanishes, and

$$\frac{\partial n^s}{\partial t} = 0, \; J^s = 0 \tag{20}$$

Equations (18) and (19) reduce to

$$\frac{dn^s}{dx} + \frac{z^s F}{RT} n^s \frac{d\psi}{dx} = 0 \qquad (21)$$

Using above equation, we can derive the relationship between concentration and potential as

$$\frac{dn^s}{n^s} = -\frac{z^s F}{RT} d\psi$$

$$\ln n^s = -\frac{z^s F}{RT} \psi + C_1$$

$$n^s = n_\infty^s \exp\left(-\frac{z^s F}{RT}\psi\right) = n_\infty^s \exp\left(-\frac{ez^s}{kT}\psi\right)$$

where $\dfrac{zF}{RT} = \dfrac{ez}{kT}$, and we have assumed that $\psi(t, x = \infty) = 0$ Therefore, for a asymmetrical electrolyte,

$$\varepsilon\varepsilon_0 \frac{d^2\psi}{dx^2} = -\sum_1^N ez^N n^N = -\sum_1^N ez^N n_\infty \exp\left(-\frac{ez^N}{kT}\psi\right)$$

$$\varepsilon\varepsilon_0 \frac{d^2\psi}{dx^2} = -ezn_\infty \exp\left(-\frac{ez}{kT}\psi\right) + ezn_\infty \exp\left(\frac{ez}{kT}\psi\right)$$

$$= 2ezn_\infty \frac{\exp\left(\frac{ez}{kT}\psi\right) - \exp\left(-\frac{ez}{kT}\psi\right)}{2}.$$

Finally, the Poisson-Boltzmann equation can be obtained as

$$\frac{d^2\psi}{dx^2} = \frac{2ezn_\infty}{\varepsilon\varepsilon_0} \sinh\left(\frac{ez}{kT}\psi\right). \tag{22}$$

The principal assumptions thus far are that the electrolyte is an ideal solution with homogeneous dielectric and transport properties and the ions are point charges. The Poisson-Boltzmann equation provides very accurate results when electrolyte concentrations do not exceed 1 M and surface potentials are less than 200 mV [18]-[20].

The Poisson-Boltzmann equation can be expressed in terms of non-dimensional variables:

$$\frac{d^2\phi}{dX^2} = \sinh\phi \tag{23}$$

where the non-dimensional potential $\phi = \dfrac{ez}{kT}\psi$, non-dimensional distance $X = \kappa x$, and

$\dfrac{1}{\kappa^2} = \dfrac{\varepsilon\varepsilon_0 kT}{2e^2 z^2 n_\infty}$. $1/\kappa$ may be called Debye length or the thickness of the double layer and

the center of gravity of the space charge coincides with this length.

Under the condition where the potential is small (<25 mV), the Poisson-Boltzmann

equation can be linearized (the Debye-Hückel approximation) to yield

$$\frac{d^2\psi}{dx^2} = \frac{2e^2 z^2 n_\infty}{\varepsilon\varepsilon_0 kT}\psi \tag{24}$$

which is called the Debye-Hückel equation. In non-dimensional form,

$$\frac{d^2\phi}{dX^2} = \phi \ . \tag{25}$$

For the general case of two dissimilar plates a distance h apart, the solution of (24) and

(25) must satisfy the following boundary condition: i) $\psi(t, x = 0) = \psi_1$ at $\phi(X = 0) = \phi_1$,

and ii) $\psi(t, x = h) = \psi_2$ or $\phi(X = \xi = \kappa h) = \phi_2$. Applying these conditions, the general

solutions of (24) and (25) become

$$\psi = \psi_1 \cosh \kappa x + \left(\frac{\psi_2 - \psi_1 \cosh \kappa h}{\sinh \kappa h}\right)\sinh \kappa x \tag{26}$$

or for non-dimensional form

$$\phi = \phi_1 \cosh X + \left(\frac{\phi_2 - \phi_1 \cosh \xi}{\sinh \xi} \right) \sinh X \; . \tag{27}$$

2) *Separation of time scales for diffusion and convection*

As shown in the chapter on analytical results, the electrode velocity $\frac{dh}{dt}$ and therefore the convection velocity V_i is very slow compared to the diffusion of each ion species. Therefore, the convection term of the Nernst-Planck equation can be neglected at this moment ($n^s V_i = 0$), and it can be assumed that the system remains in thermodynamic equilibrium when $\frac{dh}{dt} \neq 0$, i.e. the system is in thermodynamic equilibrium while the electrode is moving. Therefore, the Poisson-Boltzmann equation can be used to obtain the forces that will be used in the linear momentum equation to solve for $h(t)$.

3) *Electrochemical force*

The forces due to the electric and concentration effects are composed of two parts: an electrical force F_e and a chemical (or osmotic) force F_c that results from the difference in concentration of any ionic species in the diffuse layer and in the bulk solution. The net force due to the double layer interaction F_E can be expressed:

$$F_E = F_c + F_e .$$ (28)

This net force is sometimes called the "double layer interaction" force.

The electrochemical force is discussed in standard texts on colloidal science. Derjaguin in 1954 was the first researcher to analytically determine the electrochemical forces between surfaces at unequal potentials [21]. Nine years later, Devereux and de Bruyn in 1963 published extensive formulae and tables for the electrochemical forces acting between parallel plates at unequal potentials [22]. Two years after the work of Devereux and Bruyn, Hogg in 1965 used the linearized Poisson-Boltzmann (Debye-Hückel equation) equation (Debye-Hückel equation) to derive forces between spheres of unequal size and potential [23].

The chemical component of the interaction force is the difference in the osmotic pressure of the interstitial solution and the bulk solution with which it is in contact. The osmotic pressure of the interstitial solution acts in a positive direction and that of the bulk solution in a negative direction like

$$F_c = (P_i - P_o) A .$$ (29)

By combining the general expression for the osmotic pressure of an electrolyte solution

$$P_i = (n^+ + n^-) kT$$ (30)

$$n^+ = n_\infty \exp\left(-\frac{ez\psi}{kT}\right)$$

$$n^- = n_\infty \exp\left(\frac{ez\psi}{kT}\right).$$

Therefore,

$$P_i = \left(n_\infty \exp\left(-\frac{ez\psi}{kT}\right) + n_\infty \exp\left(\frac{ez\psi}{kT}\right)\right)kT = 2n_\infty kT \frac{\exp\left(-\frac{ez\psi}{kT}\right) + \exp\left(\frac{ez\psi}{kT}\right)}{2}$$

$$P_i = 2n_\infty kT \cosh\left(\frac{ez\psi}{kT}\right). \tag{31}$$

Also the osmotic pressure at the bulk solution with zero potential can be obtained

$$P_o = 2n_\infty kT.$$

Then,

$$F_c = \left(2n_\infty kT \cosh\left(\frac{ez\psi}{kT}\right) - 2n_\infty kT\right)A$$

or

$$F_c = 2n_\infty kTA\left(\cosh\left(\frac{ez\psi}{kT}\right)-1\right). \tag{32}$$

For non-dimensional variables,

$$F_c = 2n_\infty kTA\left(\cosh\phi-1\right). \tag{33}$$

If it is assumed that surface potential is small (<25mV), F_c can be changed using the Taylor series expansion only with the first non-zero term

$$\left(Q\cosh\phi = 1+\frac{\phi^2}{2!}+\frac{\phi^4}{4!}+\frac{\phi^6}{6!}L\right),$$

$$F_c = n_\infty kTA\phi^2. \tag{34}$$

The electrical force is given by

$$F_e = -\frac{1}{2}\varepsilon\varepsilon_0 AE^2 \tag{35}$$

The electric field can be obtained from the solution to the Poisson-Botzman equation as

$$E = \frac{d\psi}{dx} = \pm\sqrt{\frac{2n_\infty kT}{\varepsilon\varepsilon_0}}\sqrt{2\cosh\left(\frac{ez\psi}{kT}\right)+C}$$

where $C = \left(\dfrac{d\phi}{dX}\right)^2 - 2\cosh\phi$.

$$F_e = -\frac{1}{2}\varepsilon\varepsilon_0 A \frac{2n_\infty kT}{\varepsilon\varepsilon_0}\left(2\cosh\left(\frac{ez\psi}{kT}\right) + C\right) = -n_\infty kTA\left(2\cosh\left(\frac{ez\psi}{kT}\right) + C\right)$$

$$F_e = -n_\infty kTA\left(2\cosh\phi + C\right) = -n_\infty kTA\left(\frac{d\phi}{dX}\right)^2. \qquad (36)$$

The total electrochemical force is now

$$F_E = F_c + F_e$$

$$= 2n_\infty kTA\left(\cosh\left(\frac{ez\psi}{kT}\right) - 1\right) - n_\infty kTA\left(2\cosh\left(\frac{ez\psi}{kT}\right) + C\right)$$

$$= -n_\infty kTA(C + 2) \quad \left(\because C = \left(\frac{d\phi}{dX}\right)^2 - 2\cosh\phi\right)$$

$$= -n_\infty kTA\left(\left(\frac{d\phi}{dX}\right)^2 - 2\cosh\phi + 2\right),$$

therefore,

$$F_E = 2n_\infty kTA\left(\cosh\phi - 1 - \frac{1}{2}\left(\frac{d\phi}{dX}\right)^2\right). \tag{37}$$

Also in case of small potentials at the boundaries, the electrochemical force can be reduced with the (34) and (36):

$$F_E = n_\infty kTA\left[\phi^2 - \left(\frac{d\phi}{dX}\right)^2\right]. \tag{38}$$

The exact solution (27) of linearized Poisson-Boltzman equation can be used for the potential distribution and gradient of potential:

$$\phi = \phi_1\cosh X + \left(\frac{\phi_2 - \phi_1\cosh\xi}{\sinh\xi}\right)\sinh X \,,$$

$$\frac{d\phi}{dX} = \phi_1\sinh X + \left(\frac{\phi_2 - \phi_1\cosh\xi}{\sinh\xi}\right)\cosh X \,.$$

So the electrochemical force derived from the linearized Poisson-Boltzman equation can be obtained with theses three equations above:

$$F_E = \frac{\varepsilon\varepsilon_0\kappa^2 A}{2}\frac{2\psi_1\psi_2\cosh\kappa h - \left(\psi_1^2 + \psi_2^2\right)}{\sinh^2\kappa h}, \tag{39}$$

or for the non-dimensional variables,

$$F_E = 2n_\infty kTA\phi_1^2 \; \frac{\phi_2/\phi_1 \cosh\xi - \frac{1}{2}\left[1+\left(\phi_2/\phi_1\right)^2\right]}{\sinh^2\xi} \; .$$

(40)

4) Van der Waals force

For a non-polar atom, the time average of its dipole moment is zero. At any instant, there exists a finite dipole moment given by the instantaneous positions of electrons about the nuclear protons. This instantaneous dipole generates an electric field that polarizes any nearby neutral atom, including a dipole moment in it. This resulting interaction between the two atoms, gives rise to instantaneous attractive force between the two atoms, and the time average of this force is finite [20]. Therefore the attractive van der Waals force arises because local fluctuations in the polarization within one particle induce, via the propagation of electromagnetic waves, a correlated response in the other. The associated free energy decreases with decreasing separation. Phase shifts introduced at large separations by the finite velocity of propagation reduce the degree of correlation, and, therefore, the magnitude of the attraction [19]. Like the gravitational force, van der Waals force is always present and acts between all atoms and molecules.

According to the Lifshitz theory used in this research, the atom structure is ignored and the forces between large bodies, now treated as continuous media, are derived in terms of such bulk properties as their dielectric constants and refractive indices. The continuum theory accounts naturally for many body effects by treating the particle and

the intervening fluid as individual macroscopic phases characterized by dielectric permittivities. All the expressions of conventional van der Waals interactions remains valid even within the framework of continuum theories. The only thing that changes in the way the Hamaker constant is calculated [20].

The van der Waals interaction potential is largely insensitive to variations in electrolyte concentration and pH, and so may be considered as fixed in a first approximation [20].

The van der Waals force for two flat surfaces used in this research is following as:

$$F_{vdW} = -\frac{AA_h}{6\pi h^3} \tag{41}$$

where A_h is Hamaker constant.

5) Viscous damping force

The viscous damping force or squeeze-film damping force acts opposite to the direction of motion of the moving electrode and is particularly important when the separation of the two electrodes is very small compared to the length and width of the electrodes.

In case of the solid circular plate and flat plate, viscous damping force

$$F_d = -\frac{3\mu R^2 A}{2h^3}\frac{dh}{dt}, \tag{42}$$

where μ is the viscosity of media, R is the radius of circle disk, A is area of circular disk, and h is the distance between circular disk and flat plate.

6) Conservation of linear momentum

Initially the moving electrode of NEMS in the liquid electrolyte will experience elastic spring forces, viscous damping forces and van der Waals force at the spring's unstretched length 'L' as shown in Fig. 8. For the dynamic analysis, it is assumed that the electrodes remain parallel and the liquid between them is an incompressible Newtonian fluid. There are no potentials applied to the both electrodes in this case. Before potentials are applied to two electrodes, moving electrode goes to the first equilibrium position (h_0). The linear momentum equation for this case is following as:

$$m\frac{d^2h}{dt^2} = F_s + F_d + F_{vdW} \tag{43}$$

where elastic spring force $F_s = -K(h - h_0)$, and van der Waals force $F_{vdW} = -\dfrac{AA_h}{6\pi h^3}$. its initial gab distance, h_0.
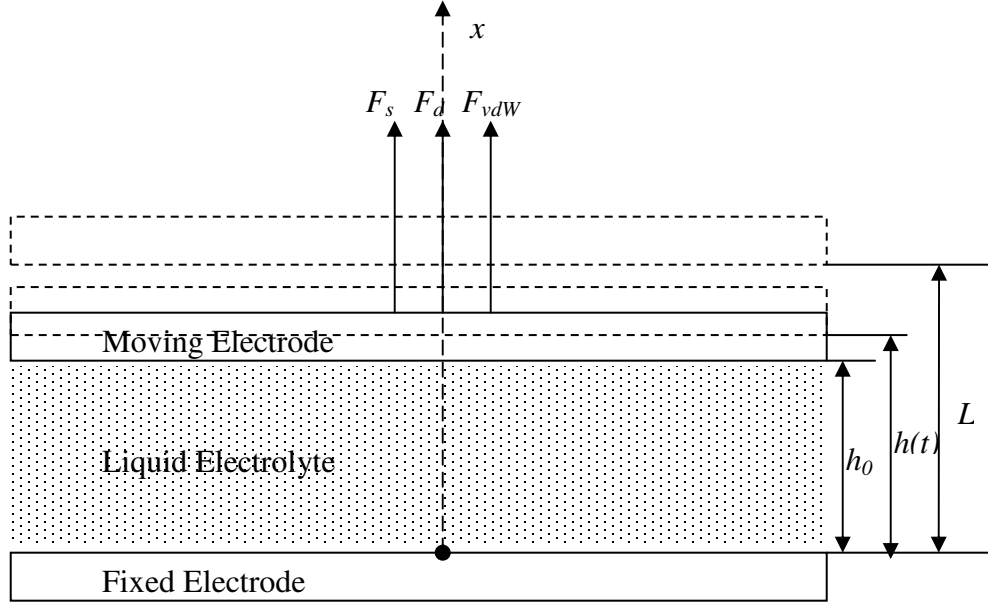
Fig. 8. Free body diagram in case of no external potentials.

Elastic spring force, viscous damping force, and van der Waals force, which are mentioned before can be used for this linear momentum equation like:

$$m\frac{d^2h}{dt^2} = K(L-h) - \frac{3\mu R^2 A}{2h^3}\frac{dh}{dt} - \frac{AA_h}{6\pi h^3}. \tag{44}$$

In equilibrium, $\frac{dh}{dt} = 0$ and $\frac{d^2h}{dt^2} = 0$ and the first equilibrium position (h_0) of moving electrode can be calculated like:

$$K(L-h_0) = \frac{AA_h}{6\pi h_0^3}. \tag{45}$$
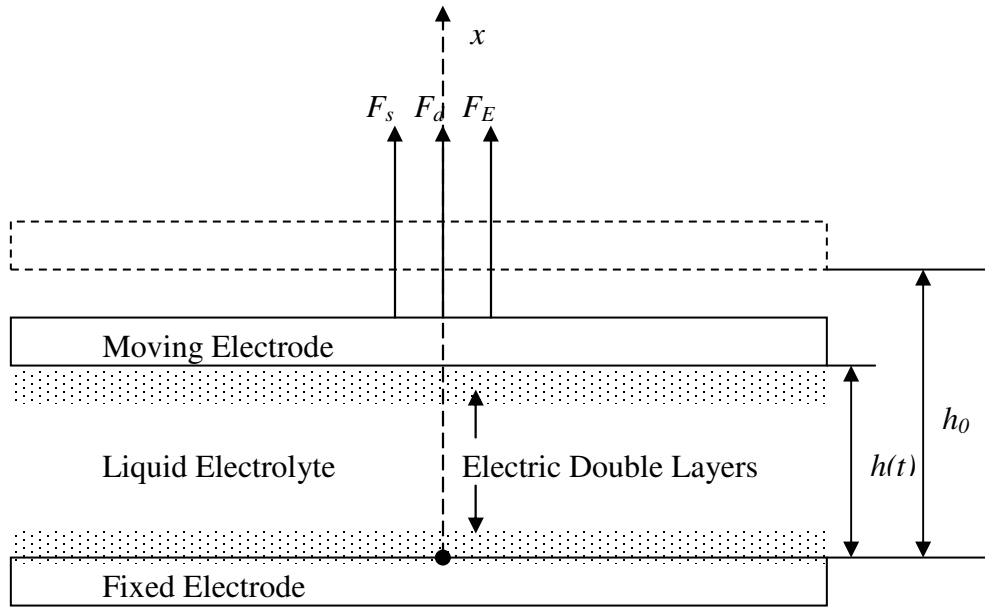
Fig. 9. Free body diagram of a moving electrode after external potentials are applied.

At the first equilibrium position of moving electrode, potentials are applied to two electrodes then the moving electrode experiences double layer interaction force together with elastic spring force, viscous damping force, and van der Waals force like Fig. 9. Therefore another linear momentum equation can be expressed like:

$$m \frac{d^2 h}{dt^2} = F_s + F_d + F_{vdW} + F_E \tag{46}$$

or

$$m\frac{d^2h}{dt^2} = K(L-h) - \frac{3\mu R^2 A}{2h^3}\frac{dh}{dt} - \varepsilon\varepsilon_0\kappa^2 A\psi_1^2\frac{1+\cosh\kappa h}{\sinh^2\kappa h} - \frac{AA_h}{6\pi h^3}. \qquad (47)$$

This linear momentum equation can be expressed with the first equilibrium position (h_0) instead of initial separation (L) like:

$$m\frac{d^2h}{dt^2} = K(h_0-h) - \frac{3\mu R^2 A}{2h^3}\frac{dh}{dt} - \varepsilon\varepsilon_0\kappa^2 A\psi_1^2\frac{1+\cosh\kappa h}{\sinh^2\kappa h} - \frac{AA_h}{6\pi}\left(\frac{1}{h^3}-\frac{1}{h_0^3}\right) \qquad (48)$$

The linear momentum equation including van der Waals force can be rearranged with the non-dimensional variables and non-dimensional parameters like:

$$B\frac{d^2h^*}{dt^{*2}} + \frac{dh^*}{dt^*} + h^* = 1 - \frac{\phi^2\xi_0^2}{K^*}\frac{1+\cosh(\xi_0 h^*)}{\sinh^2(\xi_0 h^*)} - A_h^*\left(\frac{1}{h^{*3}}-1\right) \qquad (49)$$

where non-dimensional potential, $\phi = \frac{ez}{kT}\psi_1$, non-dimensional force $B = \frac{m}{K\tau^2}$, non-dimensional spring constant $K^* = (Kh_0)\left/\left(\frac{\varepsilon\varepsilon_0 A}{h_0^2}\left(\frac{kT}{ez}\right)^2\right)\right. = \frac{e^2 z^2 Kh_0^3}{\varepsilon\varepsilon_0 k^2 T^2 A}$, non-dimensional initial distance $\xi_0 = \kappa h_0$, non-dimensional Hamaker constant $A_h^* = \left(\frac{A_h A}{6\pi h_0^3}\right)\left/(Kh_0)\right. = \frac{A_h A}{6\pi K h_0^4}$, non-dimensional separation $h^* = \frac{h}{h_0}$, Debye length, $\frac{1}{\kappa^2} = \frac{\varepsilon\varepsilon_0 kT}{2e^2 z^2 n_\infty}$, non-dimensional time, $t^* = t/\tau$, time constant $\tau = \frac{C}{K} = \frac{3\mu R^2 A}{2h^3 K}$, and

damping coefficient $C = \dfrac{3\mu R^2 A}{2h^3}$. In this case, this NEMS system has the dynamic

characteristics of first order system, then non-dimensional time, $t^* = t/\tau$ can be used for

the dynamic analysis of this system instead of $t^* = \omega_n t$ $\left(\omega_n = \sqrt{\dfrac{K}{m}} \right)$.

7) Electrochemical stored energy

The electrochemical free energy of the system (Π_F) is the amount of work to be performed in building up the double layers of the system by some reversible and isothermal process. The stored energy, (Π_E), has same magnitude as that of free energy with the negative sign ($\Pi_E = -\Pi_F$). First the free energy of a double layer system will be discussed and then stored energy will be obtained with this free energy. The work consists of a chemical part and electric part.

If in the final equilibrium state there is an excess of one of the ion species in the surface, there is obviously a chemical preference of these ions for the surface above the solution. Hence, if the ions go from one medium to another, in each step of the process considered above a constant amount of free energy is gained, corresponding to the chemical free energy difference, $\Delta \pi_F$ per ion. In the final state this free energy difference $\Delta \pi_F$ exactly outweighs the electric potential difference due to the double layer, and therefore equals $-e\psi_1$, or $\Delta \pi_F + e\psi_1 = 0$. Eventually the chemical part of the free energy of the double layer is $-e\psi_1$ per ion, or $-\sigma_1 \psi_1$ per m^2 surface, in which σ_1 is the surface charge density [24].

The previous discussion can also be understood in terms of (4) and (5), for the case in which there is no convection and the system is at thermodynamic equilibrium. In this case the gradient of the electrochemical potential is zero, and one obtains the result $\Delta\pi_F + e\psi_l = 0$ when it is assumed that the electric potential is zero at the second point at which this energy difference is calculated. Therefore,

$$\text{Chemical free energy} = -\sigma_1\psi_1. \tag{50}$$

Calling the surface potential at an arbitrary stage of the charging process ψ_1^* $\left(0 < \psi_1^* < \psi_1\right)$, we observe that ψ_1^* increases gradually from 0 to ψ_l, and the electrical charge σ_1^*, at 1 m^2 surface in an analogous way from 0 to σ_l. This potential ψ_1^* counteracts the ionic transport from of the solution to the particle surface. Hence, a gradually increasing amount of electric work has to be done $\psi_1^* d\sigma_1^*$ for each step, and for the whole charging process we find the purely electrical work quantity.

$$\text{Electric free energy} = \int_0^{\sigma_1} \psi_1^* d\sigma_1^*. \tag{51}$$

The electrochemical free energy (for 1 m^2 surface) is given by

$$\pi_F = -\sigma_1\psi_1 + \int_0^{\sigma_1} \psi_1^* d\sigma_1^*$$

in which the first term (chemical part of free energy) is larger than the second term (electric part of free energy). By partial integration both terms can be summarized into one single term like:

$$\pi_F = -\int_0^{\psi_1} \sigma_1^* d\psi_1^* \, .$$

If the electric surface potential is small, so that the linear approximation can be applied, the above equation simplifies to:

$$\pi_F = -\frac{1}{2}\sigma_1\psi_1 \, . \tag{52}$$

Also in this research, we have two electrodes:

$$\pi_F = -\frac{1}{2}\left(\sigma_1\psi_1 + \sigma_2\psi_2\right) \, . \tag{53}$$

With this free energy, the stored energy can be obtained like:

$$\Pi_E = \frac{1}{2}A\left(\sigma_1\psi_1 + \sigma_2\psi_2\right) \tag{54}$$

Where $\qquad \sigma_1 = -\varepsilon\varepsilon_0\left(\dfrac{d\psi}{dx}\right)_{x=0}$, $\qquad \sigma_2 = \varepsilon\varepsilon_0\left(\dfrac{d\psi}{dx}\right)_{x=h}$, and

$\dfrac{d\psi}{dx} = \psi_1\kappa\sinh\ \kappa h + \kappa\dfrac{\psi_2 - \psi_1\cosh\ \kappa h}{\sinh\ \kappa h}\cosh\ \kappa h$ from the exact solution of the

linearized Poisson-Boltzman equation. So, $\sigma_1 = -\varepsilon\varepsilon_0\kappa\left(\psi_2\cos ech\ \kappa h - \psi_1\coth\ \kappa h\right)$

and $\sigma_2 = \varepsilon\varepsilon_0\kappa\left(\psi_2\cot h\ \kappa h - \psi_1\cos ech\ \kappa h\right)$.

Therefore, stored electrochemical energy between two plates with linearized PB equation can be obtained as

$$\Pi_E = \frac{\varepsilon\varepsilon_0\kappa A}{2}\left[\left(\psi_1^2 + \psi_2^2\right)\coth\kappa h - 2\psi_1\psi_2\cos ech\kappa h\right]. \tag{55}$$

For the non-dimensional variables,

$$\Pi_E = \frac{n_\infty kTA}{\kappa}\left[\left(\phi_1^2 + \phi_2^2\right)\coth\xi - 2\phi_1\phi_2\cos ech\xi\right]. \tag{56}$$

8) *Double layer interaction force from the electrochemical stored energy*

The double layer interaction force can also be derived from the electrochemical energy [25]. The potentials of the electrodes are kept constant as the position of the moving electrode is changed. These potentials can only be maintained constant if the charges on the electrodes are changed. But the charges can be changed only if some agent external to the electrodes (like a battery) provides the charge. If one of the

electrodes is permitted a virtual displacement and an increment of mechanical work $dW^{(mech)}$ is done by the electrostatic forces in the process, additional work ($dW^{(B)}$) must be done to maintain all the electrodes at a constant potential. This additional work ($dW^{(B)}$) is equal to twice the change in the stored energy of double layer. So the total work by the external agents ($-dW^{(mech)} + dW^{(B)}$) equals the increase in stored energy of double layer (energy balance equation):

$$-dW^{(mech)} + dW^{(B)} = +d\Pi_E. \tag{57}$$

If the change in the charge on conductor m is called dQ_m, then $d\Pi_E = \frac{1}{2}\sum \psi_m dQ_m$ and $dW^{(B)} = \sum \psi_m dQ_m$ at constant potential. Therefore the energy balance equation above can be calculated

$$-dW^{(mech)} = -dW^{(B)} + d\Pi = -\sum \psi_m dQ_m + \frac{1}{2}\sum \psi_m dQ_m = -\frac{1}{2}\sum \psi_m dQ_m$$

or

$$dW^{(mech)} = d\Pi_E |_\psi. \tag{58}$$

If one of electrodes moves through a slight displacement *dh* under the influence of the double layer interaction force F_E, then $dW^{(mech)} = F_E\, dh$. The result of (58) leads to the expression:

$$F_E = \left.\frac{d\Pi_E}{dh}\right|_\psi .$$

(59)

Therefore, double layer interaction force derived from the linearized PB equation can be obtained with (55) and (59):

$$F_E = \frac{\varepsilon\varepsilon_0 \kappa^2 wb}{2} \frac{2\psi_1\psi_2 \cosh \kappa h - \left(\psi_1^2 + \psi_2^2\right)}{\sinh^2 \kappa h}.$$

(60)

9) Van der Waals energy

The van der Waals energy between the two electrode plates is equal to the integral of the van der Waals force with respect to the separation, *h*, between the to plates [20]. In general, the van der Waals energy for the two flat plates is given by

$$\Pi_{vdw}(h) = -\frac{A_h A}{12\pi h^2}$$

(61)

where A_h is Hamaker constant and A is area of flat plate. The difference of the van der Waals energy between h_0 and h is given by

$$\Delta\Pi_{vdw}(h) = \Pi_{vdw}(h) - \Pi_{vdw}(h_0)$$
$$= \frac{A_h A}{12\pi h^2}\left(\frac{1}{h_0^2} - \frac{1}{h^2}\right) \quad . \tag{62}$$

10) Spring energy

The elastic energy difference of the spring between positions from h_0 to h is given by

$$\Delta\Pi_s(h) = \frac{1}{2}K(h_0 - h)^2 . \tag{63}$$

11) Effect of the natural double layer

In the real world, an electrode in a liquid electrolyte can have a charge on its surface naturally, i.e. without an externally applied potential. The charging of a surface in an electrolyte can come about in two ways: i) by the ionization or dissociation of surface groups and ii) by the adsorption (binding) of ions from solution onto a previously uncharged surface [20].

With this charging process, two identical electrodes have the same charges on their surfaces in the same liquid electrolyte in the absence of an externally applied potential. The potential of the electrode due to these surface charges is the natural double layer

potential, $\psi_{natural}$. So, initially, before the application of the external potential, the free electrode feels another repulsive force due to the same charges on two electrodes

$$m\frac{d^2h}{dt^2} = F_s + F_d + F_{vdW} + F_E. \tag{64}$$

At equilibrium, the elastic spring force (F_s) and the viscous damping force (F_d) are canceled, and the linear momentum equation is given by

$$K\left(L-h_0\right) = \frac{A_h A}{6\pi h_0^3} - \varepsilon\varepsilon_0\kappa^2 A\psi_{natural}^2 \frac{\cosh \kappa h_0 - 1}{\sinh^2 \kappa h_0}. \tag{65}$$

After external potentials are applied to the two electrodes, the electrode surface potentials are $\psi_1 = \psi_{natural} + \psi_1$', and $\psi_2 = \psi_{natural} - \psi_1$'. Therefore, the linear momentum equation at equilibrium after the external potentials are applied is expressed as

$$K\left(L-h\right) - \frac{A_h A}{6\pi h_0^3} + \varepsilon\varepsilon_0\kappa^2 A \frac{\psi_{natural}^2\left(\cosh \kappa h - 1\right) - \psi_1'^2\left(\cosh \kappa h + 1\right)}{\sinh^2 \kappa h} = 0. \tag{66}$$

where L is the separation before the external potential is applied. Using (65) and (66), we can substitute the initial separation (L) with initial equilibrium distance (h_0), and finally we can get the linear momentum equation like

$$K\left(h_0 - h\right) + \frac{A_h A}{6\pi}\left(\frac{1}{h_0^3} - \frac{1}{h^3}\right)$$

$$+ \varepsilon\varepsilon_0\kappa^2 A\left\{\psi_{natural}^2\left[\frac{\cosh\kappa h - 1}{\sinh^2\kappa h} - \frac{\cosh\kappa h_0 - 1}{\sinh^2\kappa h_0}\right] - \psi_1'^2\frac{\cosh\kappa h + 1}{\sinh^2\kappa h}\right\} = 0$$

. (67)

This equation was used in order to compare the experimental result with the analytical results.

B. *Results*

1) *Transient analysis*

Equation (48) in the Analysis chapter is a differential equation for the electrode separation h as a function of the time. The double layer force used in this equation is derived from the Poissson-Boltzmann equation, which assumes that the system is in thermodynamic equilibrium. Thus, implicit in this equation is the assumption that, after the electrode electric potential is changed, the time required to complete the diffusion is much faster than the time required to complete the motion of the movable electrode.
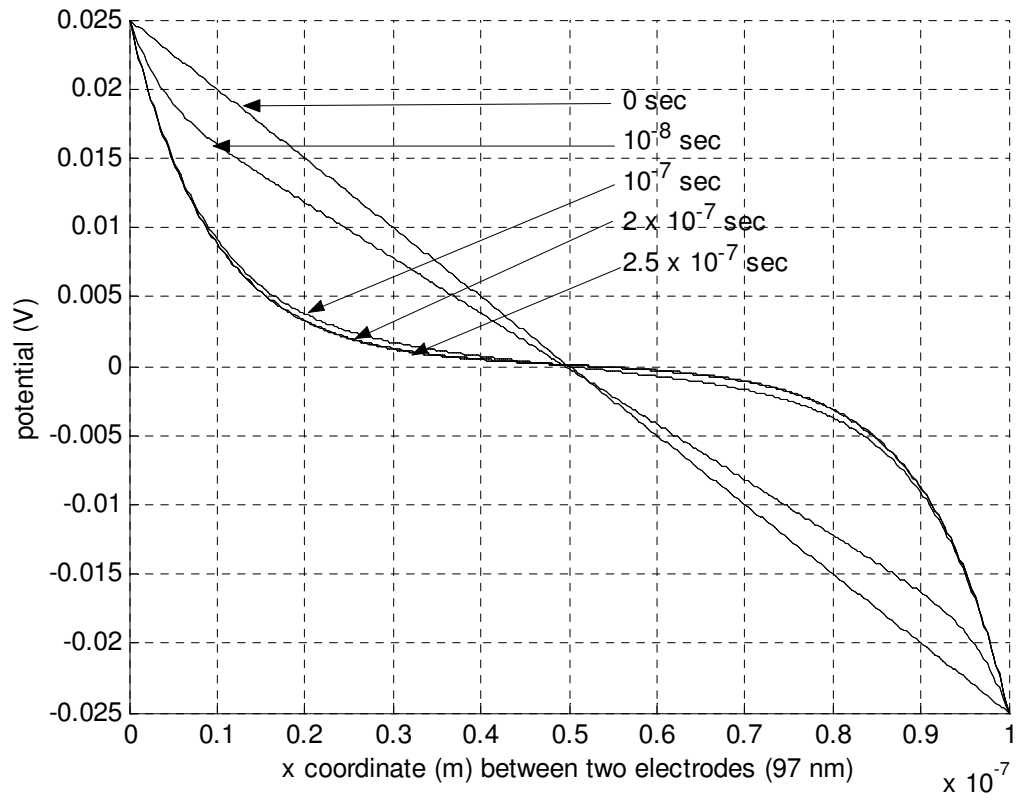
Fig. 10. Potential distribution between two electrodes (97 nm) with respect to time.
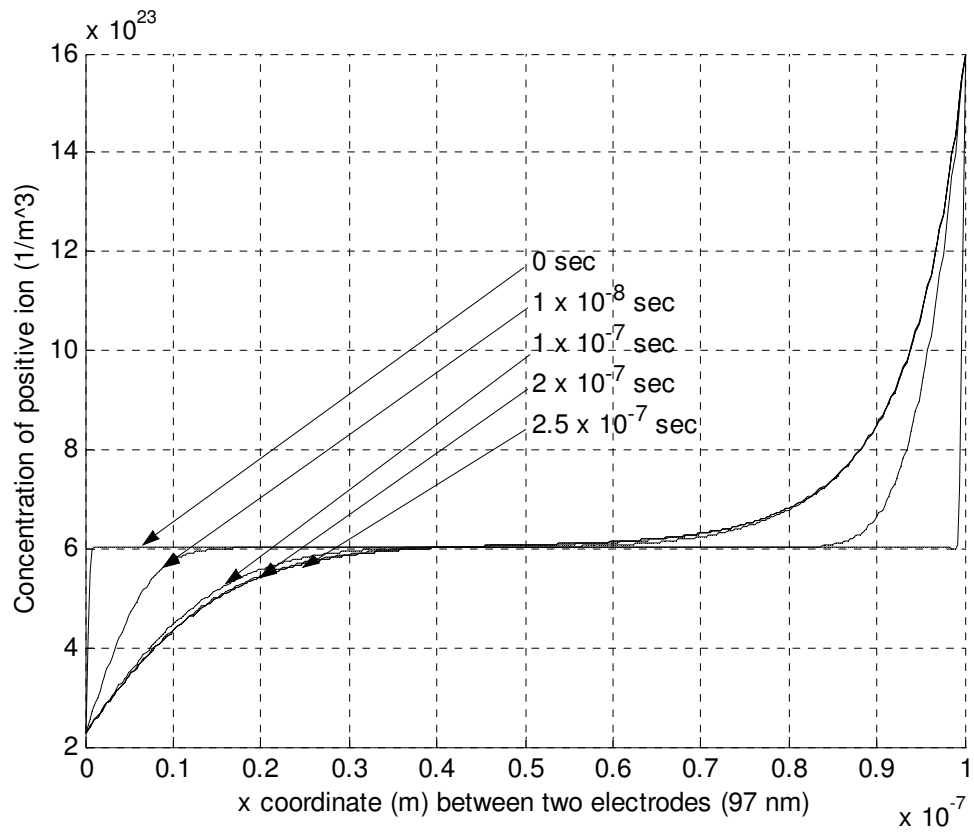
Fig. 11. Concentration of positive ion between two electrodes (97 nm)

with respect to time
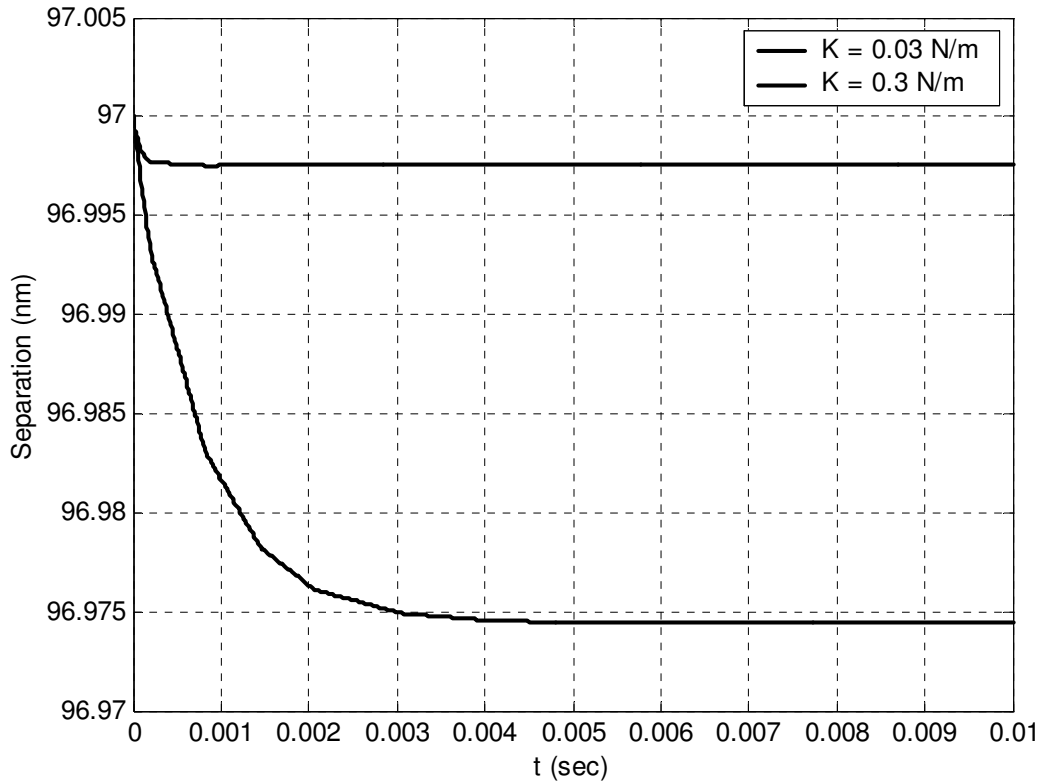
Fig. 12. Separation between two electrodes vs. time with respect to spring constant.

To test this assumption, the transient diffusion equations (17), (18), and (19) were solved using a commercially available finite element software, FEMLab, for the following conditions: ψ_1 = 0.025 V, h_0 = 97 nm, ρ_{Au} = 19.3 × 10^3 Kg/m^3, A (Area) = 1.72 μm^2 (from experiment, R (radius of gold sphere) = 2.83 μm, with Langbein approximation), $mass$ = 2.0 × 10^{-11} kg (effective mass from experiment, R (radius of gold sphere) = 2.83 μm), n_∞ = 0.001 M, T = 298 K D^+ = 1.334 × 10^{-9} m^2/s for Na$^+$, D^- = 2.032 × 10^{-9} m^2/s for Cl$^-$. Fig. 10 shows the potential distribution between two electrodes with a separation of 97 nm. It shows potential distribution due to ionic diffusion is

completed in about 2×10^{-7} seconds. Fig. 11 shows that the concentration diffusion of positive ion is completed in about 2×10^{-7} seconds. For the same conditions, the linear momentum equation was solved using the using Runge-Kutta method, and the moving electrode reached its mechanical equilibrium in approximately 0.001 seconds in the case of an elastic spring constant of 0.3 N/m and 0.005 seconds in case of elastic spring constant of 0.03 N/m in Fig. 12. Thus, because the ion diffusion is so much faster than the mechanical motion, it is assume that the system remains in chemical equilibrium throughout its motion, and that the Poisson-Boltzmann equation may therefore be used.

2) *The double layer interaction force*

The double layer interaction force per unit of electrode area is plotted in Fig. 13 as a function of the initial (or "bulk") ion concentration. The double layer interaction force rapidly decreases with increasing bulk ion concentration. Note that, for a given electrode potential, as the bulk ion concentration increases, both the electric and the osmotic forces increase. However, the osmotic force increases at a greater rate than the electric force. That means the derivative of osmotic force with respect to the bulk concentration is greater than that of electrostatic force with respect to the bulk concentration like

$$\left|\frac{\partial F_c}{\partial n_\infty}\right| > \left|\frac{\partial F_e}{\partial n_\infty}\right|. \tag{68}$$

The osmotic force is repulsive, whereas the electric force is attractive.
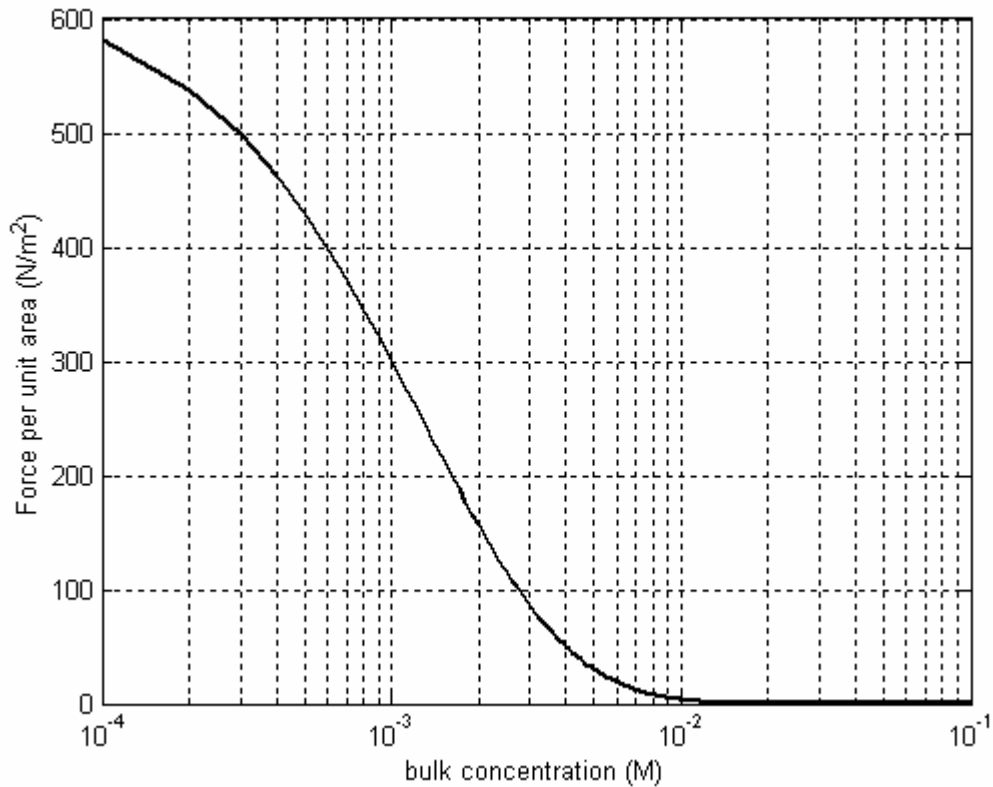
Fig. 13. Double layer interaction force per unit area vs. bulk concentration

for given $h_0 = 30$ nm, $\psi_1 = 0.02$ V.

3) Pull-in instability

At mechanical and chemical equilibrium, for the case that the electrode potentials are small (<25mV) and the potential (ψ_2) applied at the moving electrode has the same magnitude but opposite sign as that of fixed electrode $(\psi_2 = -\psi_1)$, the equilibrium equation simplifies to

$$K\left(h_0 - h\right) = \varepsilon\kappa^2 A\psi_1^2 \frac{\cosh \kappa h + 1}{\sinh^2 \kappa h} + \frac{A_h A}{6\pi}\left(\frac{1}{h^3} - \frac{1}{h_0^3}\right) \qquad (69)$$

which can be non-dimensionalized as

$$\left(1 - h^*\right) = \frac{\phi^2 \xi_0^2}{K^*} \frac{1 + \cosh\left(\xi_0 h^*\right)}{\sinh^2\left(\xi_0 h^*\right)} + A_h^*\left(\frac{1}{h^{*3}} - 1\right) \qquad (70)$$

where ϕ is the non-dimensional potential, h^* is a non-dimensional electrode separation, K^* is the non-dimensional elastic spring constant, A_h^* is the non-dimensional Hamaker constant, and ξ_0 is the non-dimensional initial electrode separation.

Fig. 14 shows the non-dimensional elastic spring force and the non-dimensional double layer interaction force plus the van der Waals force as functions of the electrode separation (h^*). The non-dimensional spring force is

$$F_s^* = \left(1 - h^*\right)$$

and summation of non-dimensional double layer interaction force and van der Waals interaction force is

$$F_E^* + F_{vdw}^* = \frac{\phi^2 \xi_0^2}{K^*} \frac{1 + \cosh\left(\xi_0 h^*\right)}{\sinh^2\left(\xi_0 h^*\right)} + A_h^*\left(\frac{1}{h^{*3}} - 1\right).$$
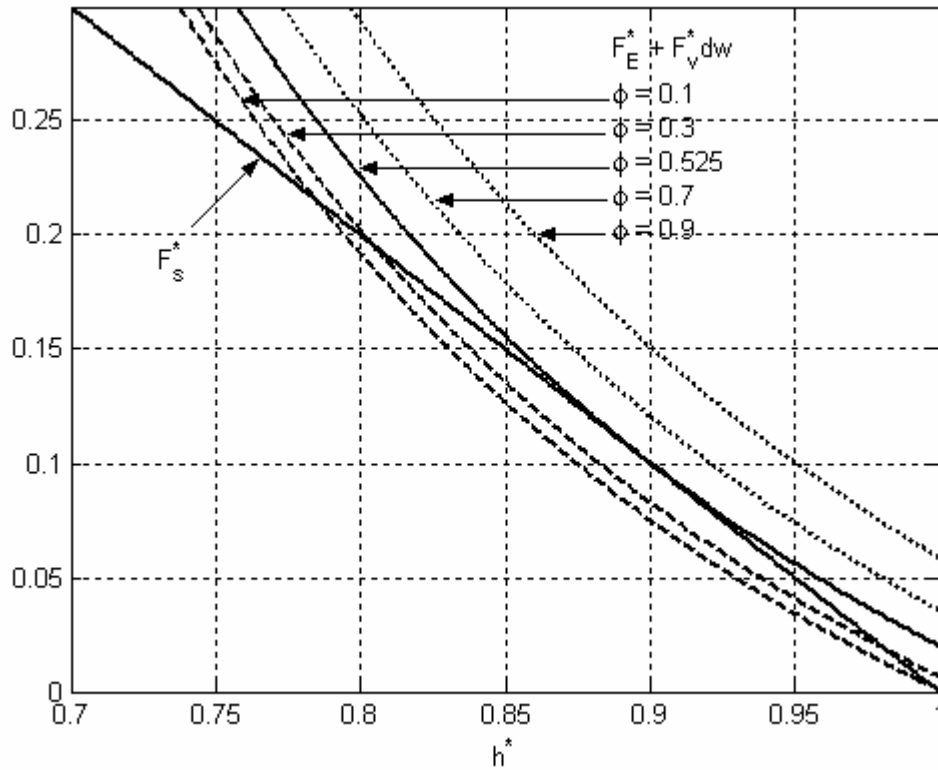
Fig. 14. Non-dimensional force vs. non-dimensional distance (h^*) with respect to ϕ

for given $\xi_0 = 5$, $A_h^* = 0.2$, and $K^* = 20$.

Intersections of the non-dimensional elastic spring force and summation of non-dimensional double layer interaction force and van der Waals interaction force indicate the equilibrium positions. Only one equilibrium point can exist on summation of non-dimensional double layer interaction force and van der Waals interaction force corresponding to the non-dimensional critical pull-in potential (ϕ), 0.525. Below this potential, the moving electrode has two equilibrium positions so moving electrode goes to a stable equilibrium position, that is one of two equilibrium positions; above this potential the attractive double layer interaction force dominates the elastic spring force

and the moving electrode goes to and contact the fixed electrode without equilibrium position.

The non-dimensional potential can be obtained explicitly as

$$\phi = \sqrt{\frac{K^*}{\xi_0^2}\left\{\left(1-h^*\right)-A_h^*\left(\frac{1}{h^{*3}}-1\right)\right\}\frac{\sinh^2\left(\xi_0 h^*\right)}{1+\cosh\left(\xi_0 h^*\right)}} \; . \tag{71}$$

Using above (71), potentials for the equilibrium position of moving electrode can be obtained for each non-dimensional parameter like Fig. 15, Fig. 18, or Fig. 21. The non-dimensional critical distance $\left(h_{cri}^*\right)$ can be obtained using derivative of non-dimensional potential with respect to non-dimensional distance like:

$$\frac{d\phi}{dh^*} = 0 \tag{72}$$

Then the non-dimensional critical potential $\left(\phi_{cri}\right)$ can be obtained by substituting the non-dimensional critical distance $\left(h_{cri}^*\right)$ into (71).

In (71), the elastic spring force must be always greater than the van der Waals force, that is:

$$K\left(h_0-h\right) > \frac{AA_h}{6\pi}\left(\frac{1}{h^3}-\frac{1}{h_0^3}\right) \tag{73}$$

or

$$A_h^* < \left(1 - h^*\right)\left(\frac{1}{h^{*3}} - 1\right)^{-1}.$$
(74)

The right hand side equation of the above inequality has the range from 0 to 1/3.

Therefore, A_h^* must be less than 1/3.

Fig. 15 shows the equilibrium position of moving electrode for the each potential as K^* changes. The points having maximum non-dimensional potential are the critical points, and non-dimensional distances at these critical points are non-dimensional critical distances $\left(h_{cri}^*\right)$. Fig. 16 shows h_{cri}^* with respect to K^* for given A_h^* and ξ_0. K^* has no effect on h_{cri}^* for given A_h^* and ξ_0. And h_{cri}^* is function of A_h^* and ξ_0. This phenomenon can be expected by following mathematical procedure:

$$\begin{aligned}
\frac{d\phi}{dh^*} &= \frac{d}{dh^*}\left(\sqrt{\frac{K^*}{\xi_0^2}\left\{\left(1 - h^*\right) - A_h^*\left(\frac{1}{h^{*3}} - 1\right)\right\}}\frac{\sinh\left(\xi_0 h^*\right)}{1 + \cosh\left(\xi_0 h^*\right)}\right) \\
&= \sqrt{\frac{K^*}{\xi_0^2}}\frac{d}{dh^*}\left(\sqrt{\left\{\left(1 - h^*\right) - A_h^*\left(\frac{1}{h^{*3}} - 1\right)\right\}}\frac{\sinh\left(\xi_0 h^*\right)}{1 + \cosh\left(\xi_0 h^*\right)}\right) = 0
\end{aligned}.$$

In the last parenthesis, there exist A_h^* and ξ_0 as parameters. Therefore, h_{cri}^* satisfied with this equality must be function of A_h^* and ξ_0, not function of K^*. Fig. 17 shows ϕ_{cri} is proportional to the square root of K^* for fixed ξ_0.

Fig. 15. Non-dimensional distance (h^*) vs. non-dimensional potential (ϕ) with respect to K^* for given $\xi_0 = 2$ and $A_h^* = 0.2$.
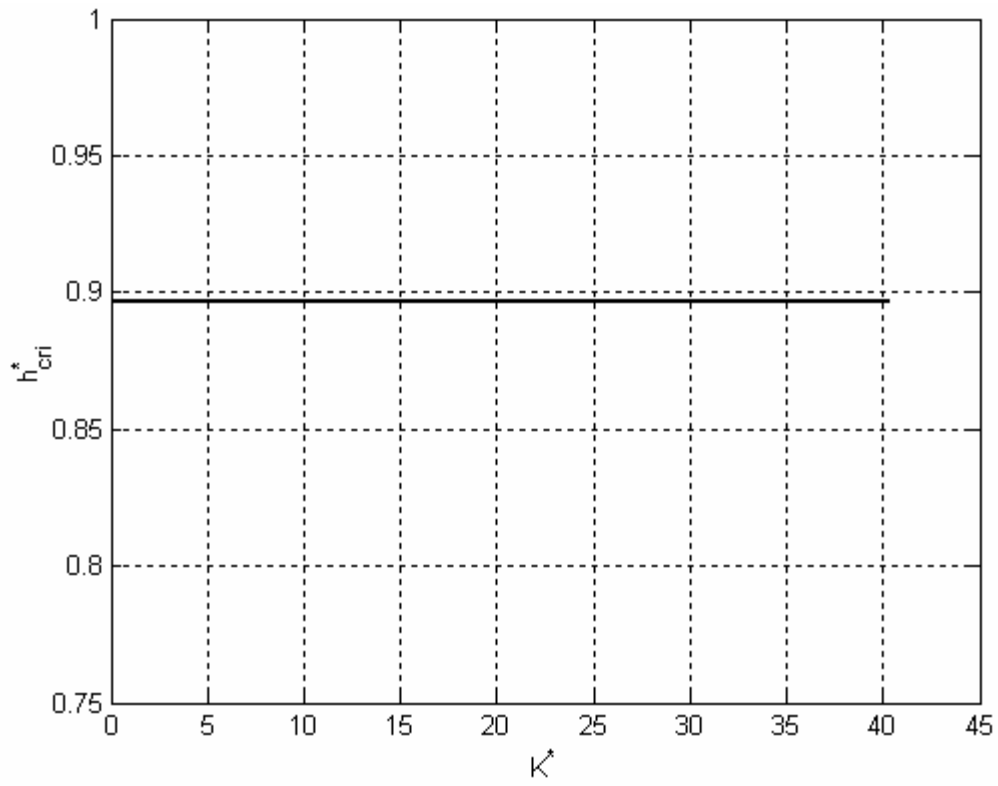
Fig. 16. Non-dimensional critical distance (h_{cri}^*) vs. non-dimensional spring constant

(K^*) for given $A_h^* = 0.2$, $\xi_0 = 2$.

Fig. 17. Non-dimensional critical potential (ϕ_{cri}) vs. non-dimensional spring constant

(K^*) for given $A_h^* = 0.2$, $\xi_0 = 2$.

Fig. 18 show the equilibrium position of the moving electrode for the each potential as ξ_0 changes for given K^* and A_h^*. The points having maximum non-dimensional potential are the critical points, and non-dimensional distances at these points are non-dimensional critical distances. Fig. 19 shows h_{cri}^* with that respect to ξ_0. h_{cri}^* does not go to 2/3, which is the same as the non-dimensional distance of a normal electrostatic capacitor, as ξ_0 goes to zero because there exists attractive van der Waals force. h_{cri}^* increases as ξ_0 increases. That means the motion range of moving electrode $\left(h_0 - h_{cri}\right)$

becomes smaller as the bulk concentration (n_∞) increases for given initial distance. Fig. 20 shows that ϕ_{cri} increases for given A_h^* and K^* as ξ_0 increases.
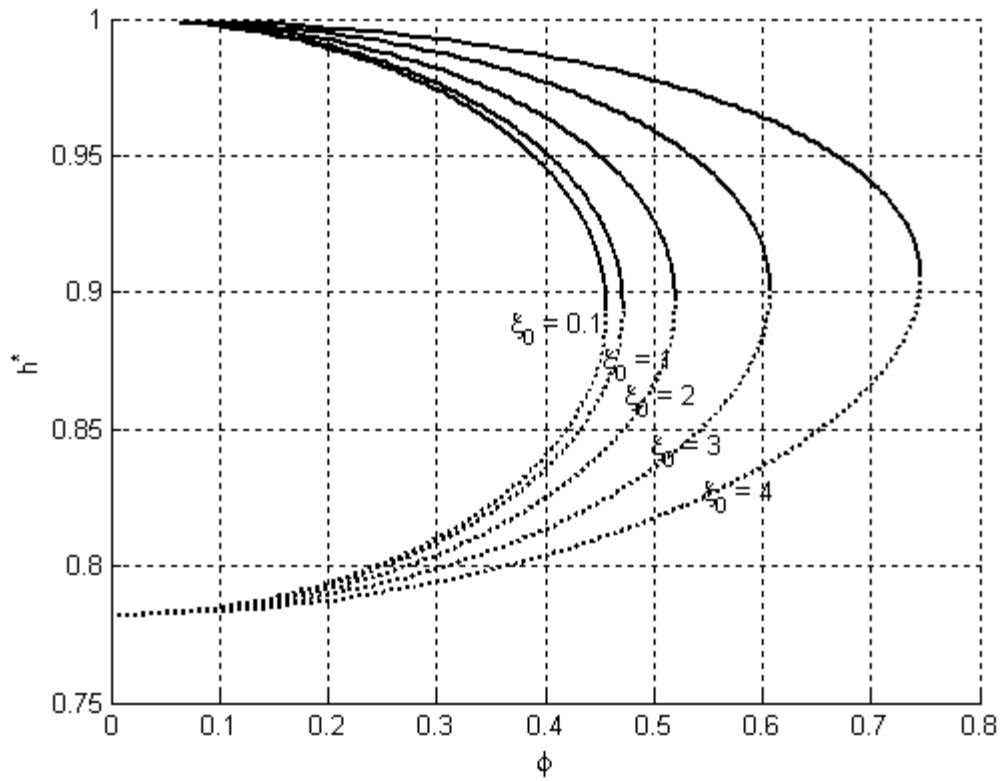
Fig. 18. Non-dimensional distance (h^*) vs. non-dimensional potential (ϕ) with respect to ξ_0 for given $K^* = 20$ and $A_h^* = 0.2$.
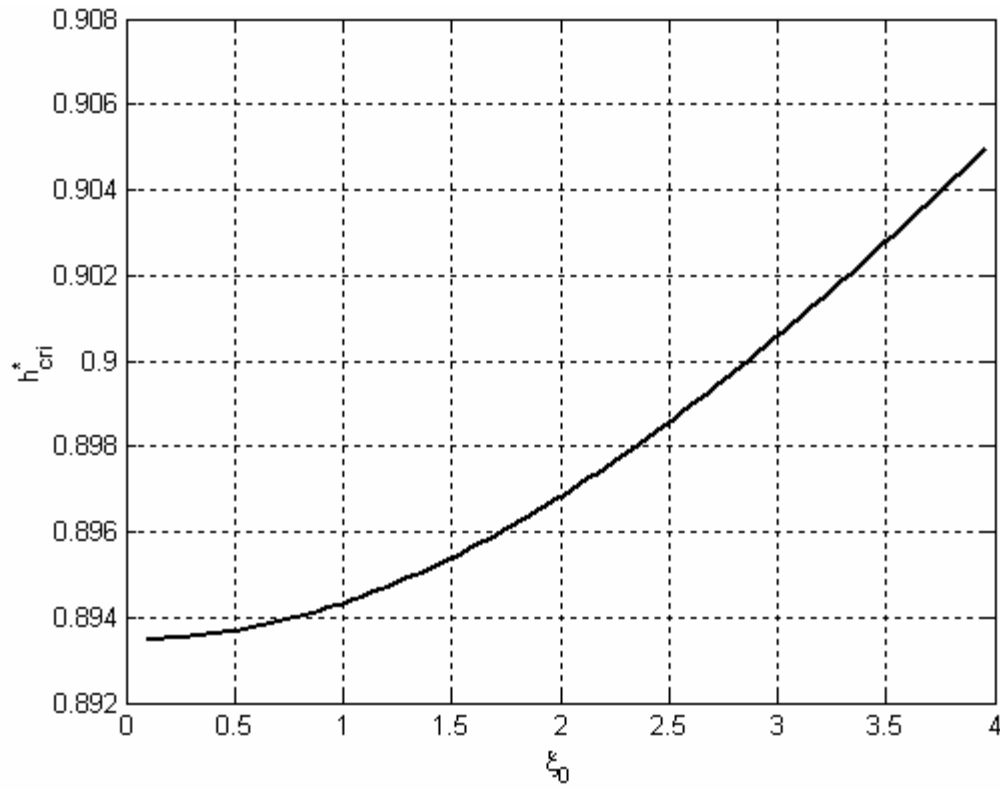
Fig. 19. Non-dimensional critical distance (h_{cri}^*) vs. non-dimensional initial distance (ξ_0)
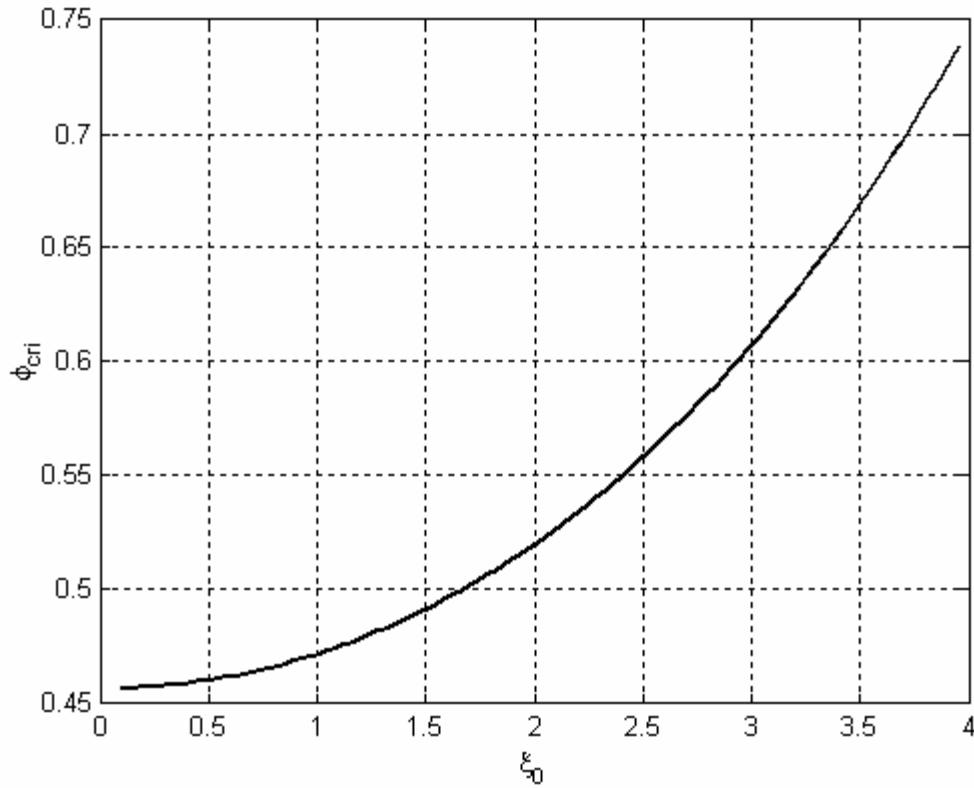
for given $A_h^* = 0.2$, $K^* = 20$.

Fig. 20. Non-dimensional critical potential (ϕ_{cri}) vs. non-dimensional initial distance

(ξ_0) for given $A_h^* = 0.2$, $K^* = 20$.

Fig. 21 shows the electrode separation for each potential as A_h^* changes for given K^* and ξ_0. The points having maximum non-dimensional potential are the critical points, and non-dimensional separations at these points are non-dimensional critical separations. Fig. 22 shows that h_{cri}^* increases because attractive van der Waals force increases as A_h^* increases. The stroke of the moving electrode grows smaller as van der Waals force increases for given initial distance. Fig. 23 shows that ϕ_{cri} decreases as A_h^* increases.
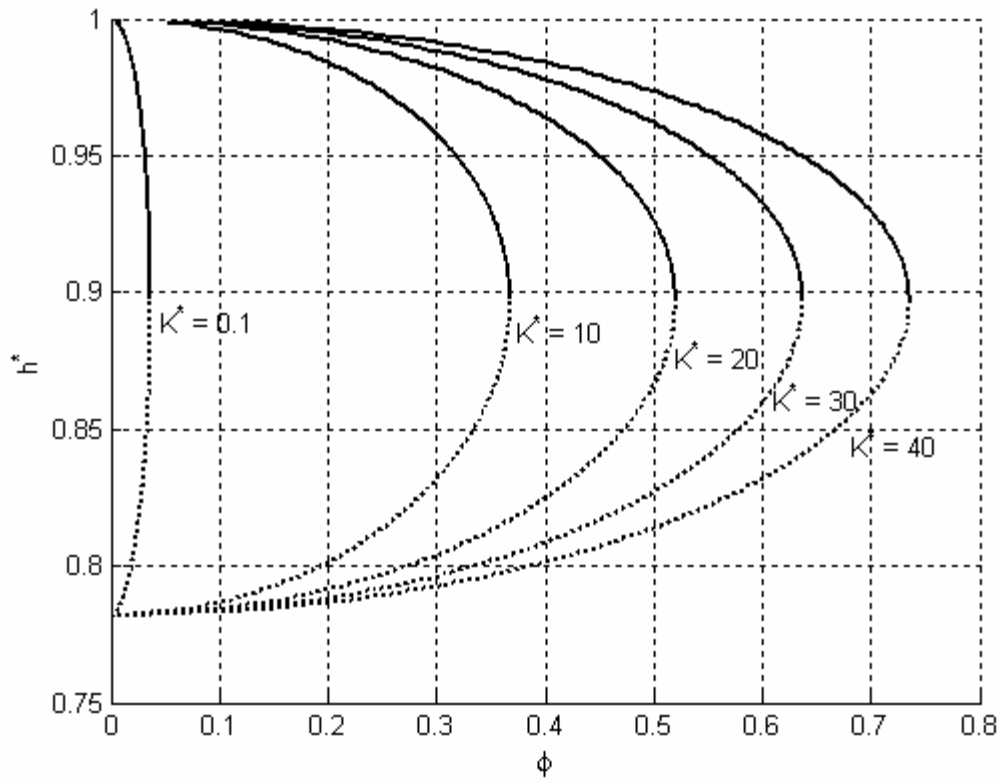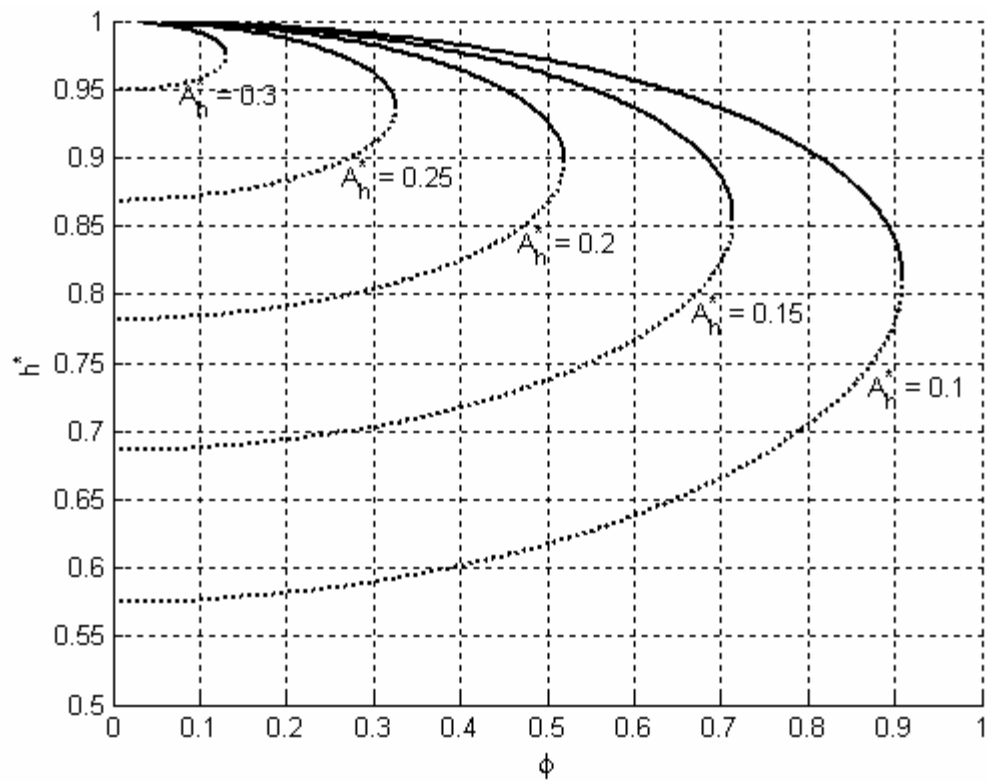
Fig. 21. Non-dimensional distance (h^*) vs. non-dimensional potential (ϕ)

with respect to A_h^* for given $\xi_0 = 2$ and $K^* = 20$.
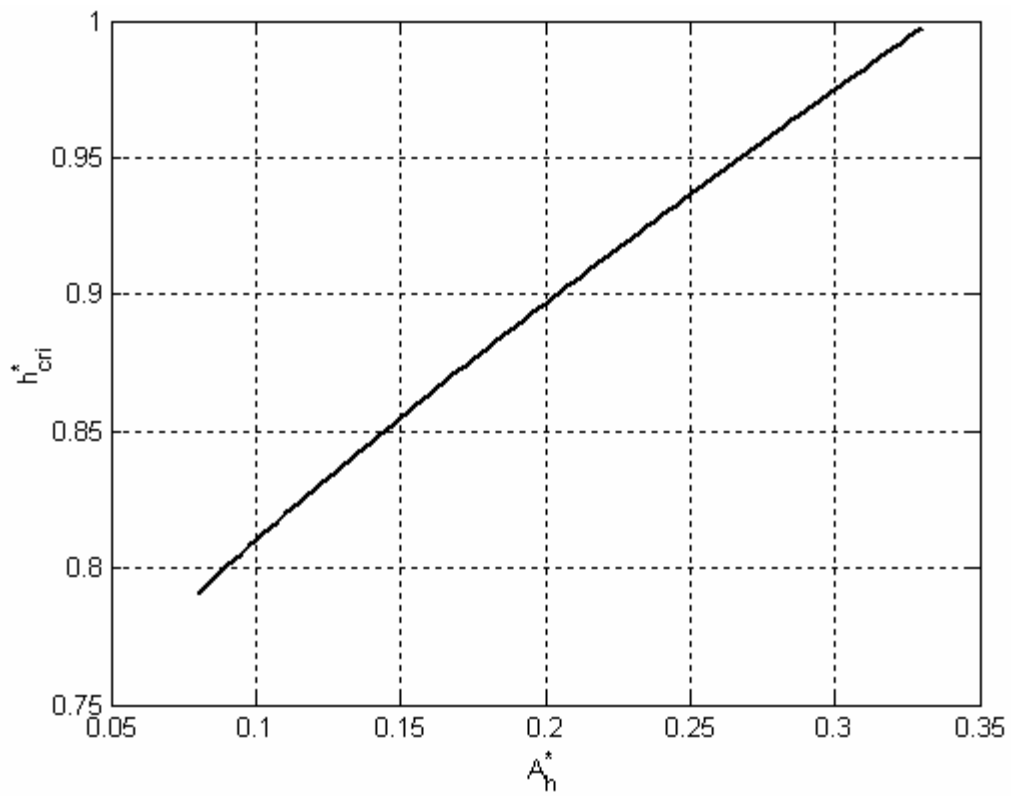
Fig. 22. Non-dimensional critical distance (h^*_{cri}) vs. non-dimensional Hamaker constant (A^*_h) for given $K^* = 20$, $\xi_0 = 2$.
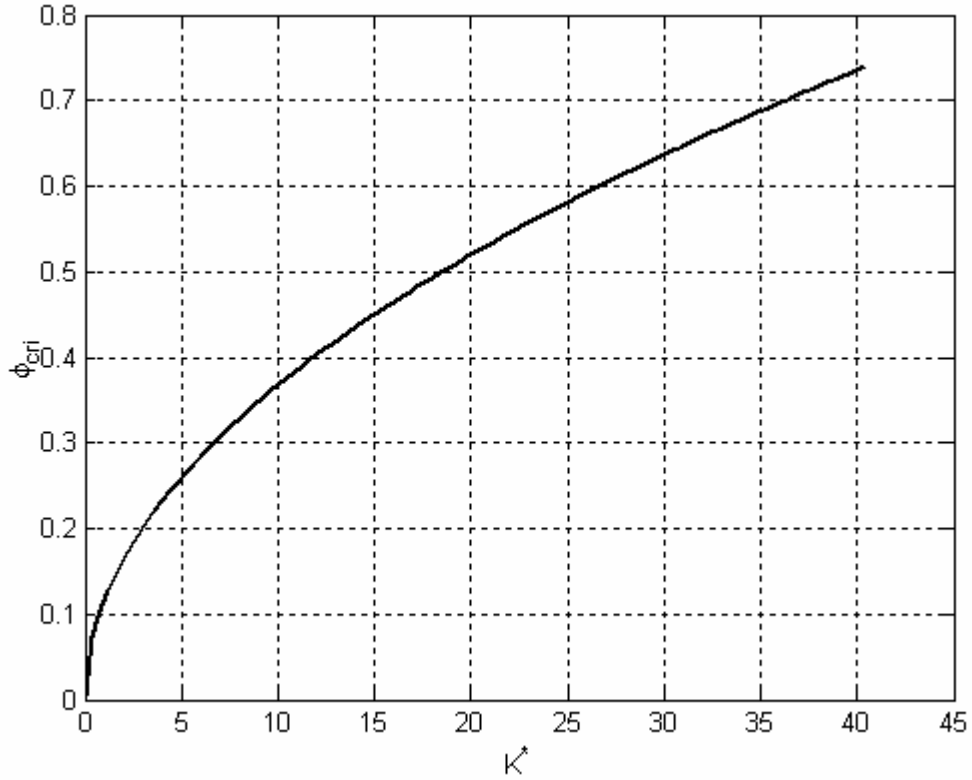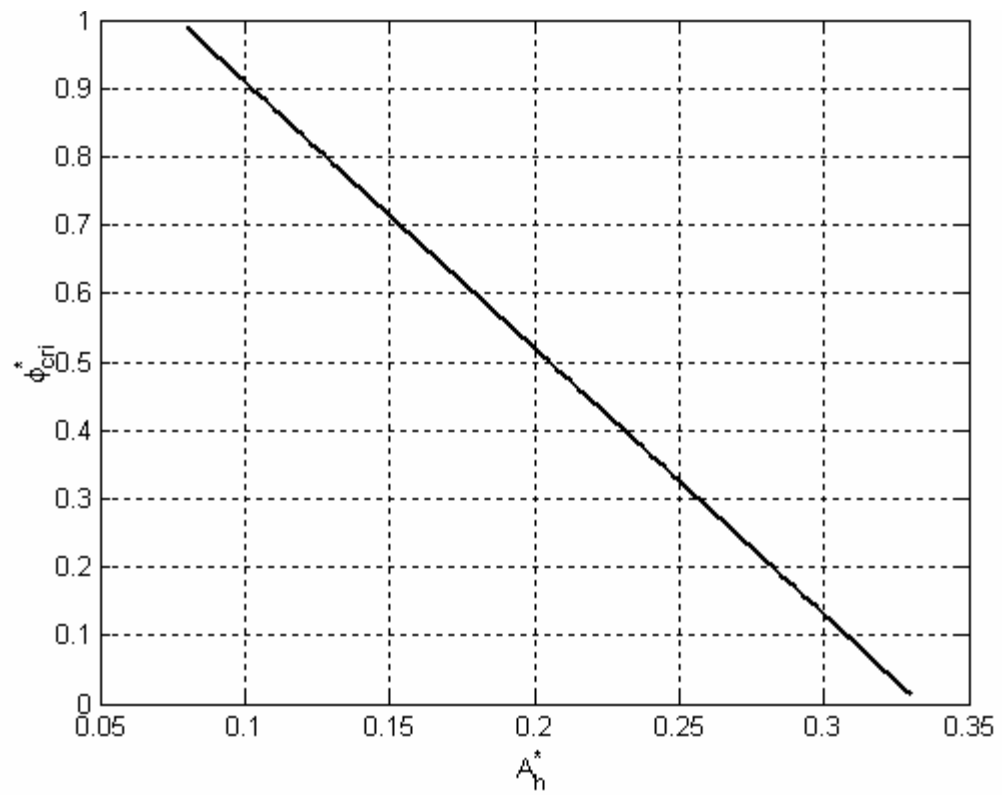
Fig. 23. Non-dimensional critical potential (ϕ_{cri}^*) vs. non-dimensional Hamaker constant

(A_h^*) for given $K^* = 20$, $\xi_0 = 2$.

4) Stored energy

Equation (55) was used for the electrochemical stored energy. Using this equation, the stored energy of a normal capacitor may be calculated assuming that the bulk concentration (n_∞) goes to zero:

$$\Pi_{(n_\infty=0)} = \lim_{n\to 0} \Pi_{(n_\infty>0)} = \lim_{\kappa\to 0} \Pi_{(n_\infty>0)}$$

$$= \lim_{\kappa\to 0} \frac{\varepsilon A}{2}\left[\left(\psi_1^2+\psi_2^2\right)\frac{\kappa}{\sinh\kappa h}\cosh\kappa h - 2\psi_1\psi_2 \frac{\kappa}{\sinh\kappa h}\right]$$

$$= \frac{\varepsilon A}{2}\left(\psi_1^2+\psi_2^2-2\psi_1\psi_2\right)$$

$$\Pi_{(n_\infty=0)} = \frac{1}{2}\frac{\varepsilon A}{h}\left(\psi_1-\psi_2\right)^2.$$

Equation (55) can be reduced because the boundary condition is that $\psi_2 = -\psi_1$ in this paper:

$$\Pi_E = \varepsilon\kappa A\psi_1^2\left(\coth\kappa h+\mathrm{cosech}\,\kappa h\right). \tag{75}$$

Or for non-dimensional form,

$$\Pi_E = \frac{2}{\kappa}kTn_\infty\phi_1^2\left(\coth\left(\xi_0 h^*\right)+\mathrm{cosec}\left(\xi_0 h^*\right)\right). \tag{76}$$

For a given potential and geometry, the electrochemical stored energy density (π_E) increases as the bulk concentration (n_∞) increases and the initial distance (h_0) decreases as shown in Fig. 24. Also, the electrochemical stored energy density increases with the square root of the bulk concentration and exponentially increases as separation increases as shown in (75). With this analysis, we can conclude that the double layer capacitor may store more energy than a normal capacitor for a given geometry and potential at the boundary because a normal capacitor corresponds to a capacitor with zero bulk concentration. This energy is the same as the energy of a system which has two fixed electrodes with given separation, therefore the spring constant is not included in (76).
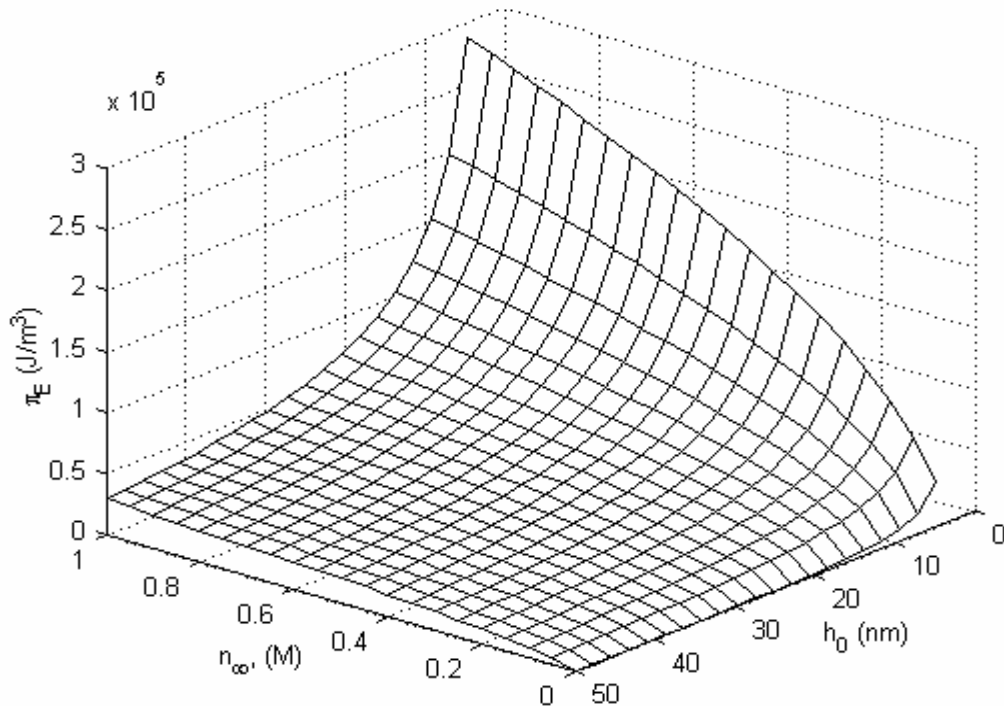
Fig. 24. Electrochemical stored energy density (π_E) in double layer system vs. bulk concentration (n_∞) and initial distance (h_0) for given $\psi_I = 25$ mV.

The electrochemical stored energy can be non-dimensionalized using the elastic spring energy at h_0:

$$\Pi_E^* = \frac{\Pi_E}{\Pi_s(h_0)} = \frac{\frac{2}{\kappa}kTAn_\infty\phi^2\left\{\coth\left(\xi_0 h^*\right)+\cos ech\left(\xi_0 h^*\right)\right\}}{\frac{1}{2}Kh_0^2} . \qquad (77)$$

The non-dimensional electrochemical stored energy has a maximum value at the critical point within stable region in Fig. 25, where a solid line represents the stable region and dotted line represents the unstable region. The electrochemical stored energy of system increases as the moving electrode goes to the fixed electrode up to the critical distance and as the potentials at the boundaries increase. In Fig. 25, the moving electrode can move toward the fixed electrode up to the critical distance and at this distance this system has the maximum stored energy within the stable region. As the potential at the fixed electrode increases, the moving electrode goes to the fixed electrode closely but above critical voltage it contacts the fixed electrode suddenly. Nano electromechanical systems in this paper for given geometry can have the maximum electrochemical stored energy at the critical distance and critical potential $\left(h = h_{cri},\ \phi = \phi_{cri}\right)$ because moving electrode can go to the fixed electrode with the equilibrium distance stably below critical potential or above critical distance as mentioned before while above critical potential or below critical distance, it can not.
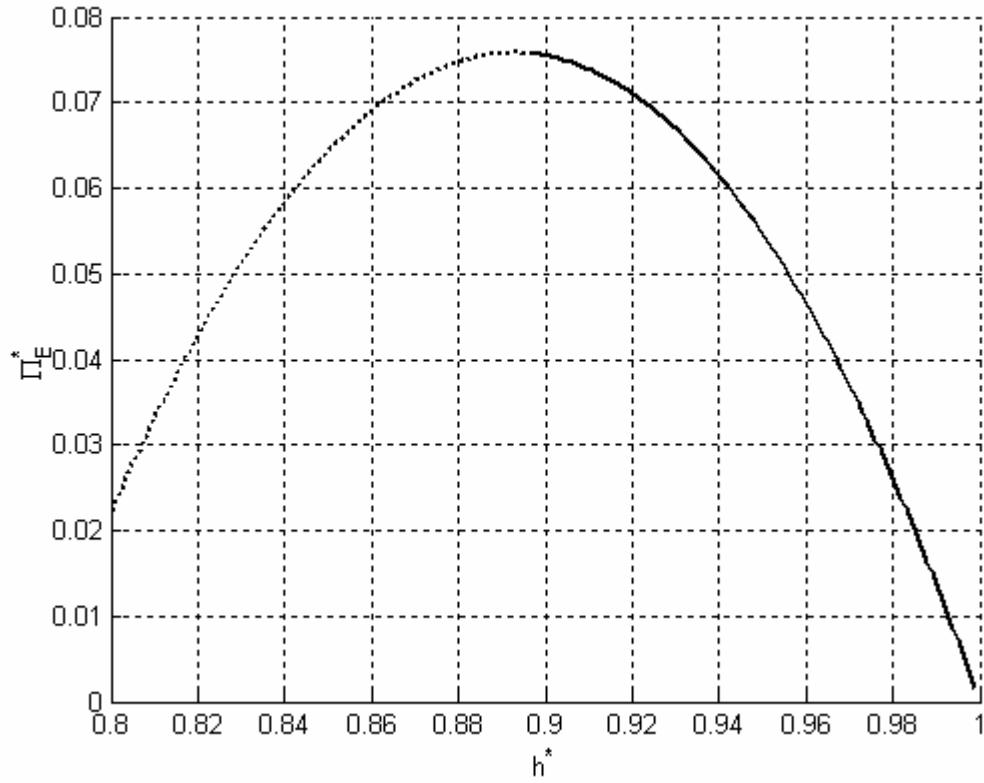
Fig. 25. Non-dimensional electrochemical stored energy in double layer system at

equilibrium $\left(\Pi_E^*\right)$ vs. h^* for given $K^* = 5$, $\xi_0 = 2$ and $A_h^* = 0.2$.

The non-dimensional maximum electrochemical stored energy in the double layer
system can be expressed with energy stored in elastic spring at h_0 like:

$$Max\left(\Pi_E^*\right) = \frac{Max\left(\Pi_E\right)}{\Pi_s\left(h_0\right)} = \frac{\frac{2}{\kappa}kTAn_\infty\phi_{cri}^2\left\{\coth\left(\xi_0 h_{cri}^*\right) + \cos ech\left(\xi_0 h_{cri}^*\right)\right\}}{\frac{1}{2}kh_0^2} \tag{78}$$

$Max\left(\Pi_E^*\right)$ is the ratio of maximum electrochemical stored energy in double layer system at the critical point to elastic energy stored in spring at h_0. Using (71), $Max\left(\Pi_E^*\right)$ can be function of h_{cri}^*, A_h^* and ξ_0, therefore can be simplified like:

$$Max\left(\Pi_E^*\right) = \frac{2}{\xi_0}\left\{\left(1 - h_{cri}^*\right) - A_h^*\left(\frac{1}{h_{cri}^{*3}} - 1\right)\right\}\sinh\left(\xi_0 h_{cri}^*\right) \tag{79}$$

The non-dimensional energy difference stored in the elastic spring can be expressed with energy stored in elastic spring at h_0 like:

$$\Delta\Pi_s^* = \frac{\Delta\Pi_s}{\Pi_s\left(h_0\right)} = \frac{\frac{1}{2}K\left(h_0 - h_{cri}\right)^2}{\frac{1}{2}Kh_0^2} = \left(1 - \frac{h_{cri}}{h_0}\right)^2 \tag{80}$$

or

$$\Delta\Pi_s^* = \left(1 - h_{cri}^*\right)^2. \tag{81}$$

$\Delta\Pi_s^*$ is the ratio of energy difference stored in elastic spring to energy stored in elastic spring at h_0.

Also, the non-dimensional van der Waals interaction energy can be obtained with energy stored in elastic spring at h_0 like:

$$\Delta\Pi_{vdw}^* = \frac{\Delta\Pi_{vdw}}{\Pi_s\left(h_0\right)} = \frac{\dfrac{A_h A}{12\pi}\left(\dfrac{1}{h_0^2} - \dfrac{1}{h_{cri}^2}\right)}{\dfrac{1}{2}K h_0^2} = \frac{A_h A}{6\pi K h_0^4}\left(1 - \frac{1}{\left(h_0 \Big/ h_{cri}\right)^2}\right) \qquad (82)$$

or

$$\Delta\Pi_{vdw}^* = A_h^*\left(1 - \frac{1}{h_{cri}^{*2}}\right). \qquad (83)$$

$\Delta\Pi_s^*$ is the ratio of van der Waals interaction energy difference to energy stored in the elastic spring at h_0.

R_1 is the ratio of the non-dimensional energy difference stored in the elastic spring to the non-dimensional maximum electrochemical stored energy, or energy difference stored in elastic spring to maximum electrochemical stored energy:

$$R_1 = \frac{\Delta\Pi_s^*}{Max\left(\Pi_E^*\right)} = \frac{\Delta\Pi_s}{Max\left(\Pi_E\right)} = \frac{\left(1 - h_{cri}^*\right)^2}{\dfrac{2}{\xi_0}\left\{\left(1 - h_{cri}^*\right) - A_h^*\left(\dfrac{1}{h_{cri}^{*3}} - 1\right)\right\}\sinh\left(\xi_0 h_{cri}^*\right)}. \qquad (84)$$

As the bulk concentration and the Hamaker constant go to zero, R_1 goes to 1/4 , which is the same result as a normal electrostatic capacitor,

$$\lim_{\substack{n_\infty \to 0 \\ A_h \to 0}} R_1 = \lim_{\substack{\xi_0 \to 0 \\ A_h^* \to 0}} R_1 = \lim_{\substack{\xi_0 \to 0 \\ A_h^* \to 0}} \frac{\xi_0 \left(1 - h_{cri}^*\right)^2}{2\left\{\left(1 - h_{cri}^*\right) - A_h^*\left(\dfrac{1}{h_{cri}^{*3}} - 1\right)\right\} \sinh\left(\xi_0 h_{cri}^*\right)} = \frac{1}{4}.$$

R_2 is the ratio of the non-dimensional van der Waals interaction energy difference to non-dimensional maximum electrochemical stored energy, or the van der Waals interaction energy difference to maximum electrochemical stored energy:

$$R_2 = \frac{\Delta\Pi_{vdw}^*}{Max\left(\Pi_E^*\right)} = \frac{\Delta\Pi_{vdw}}{Max\left(\Pi_E\right)} = \frac{A_h^*\left(1 - \dfrac{1}{h_{cri}^{*2}}\right)}{\dfrac{2}{\xi_0}\left\{\left(1 - h_{cri}^*\right) - A_h^*\left(\dfrac{1}{h_{cri}^{*3}} - 1\right)\right\} \sinh\left(\xi_0 h_{cri}^*\right)}. \qquad (85)$$

R_3 is the ratio of non-dimensional van der Waals interaction energy difference to the non-dimensional energy difference stored in the elastic spring, or the van der Waals interaction energy difference to energy difference stored in the elastic spring:

$$R_3 = \frac{\Delta\Pi_{vdw}^*}{\Delta\Pi_s^*} = \frac{\Delta\Pi_{vdw}}{\Delta\Pi_s} = \frac{A_h^*\left(1 - \dfrac{1}{h_{cri}^{*2}}\right)}{\left(1 - h_{cri}^*\right)^2} = -\frac{A_h^*\left(1 + h_{cri}^*\right)}{h_{cri}^*\left(1 - h_{cri}^*\right)}. \qquad (86)$$

These non-dimensional energies and ratios are functions of ξ_0, K^*, and A_h^* because h_{cri}^* is function of these parameters. Fig. 26 shows $Max\left(\Pi_E^*\right)$ increase as ξ_0 increase. Physically, the more bulk concentration exists for given geometry, the much more

energy can be stored electrochemically. Fig. 27 shows that K^* has no effect on $Max\left(\Pi_E^*\right)$ because h_{cri}^* is not function of K^* for given A_h^* and ξ_0. Fig. 28 shows $Max\left(\Pi_E^*\right)$ goes down as A_h^* increases because h_{cri}^* increases and ϕ_{cri} decreases as A_h^* increases for given K^* and ξ_0.
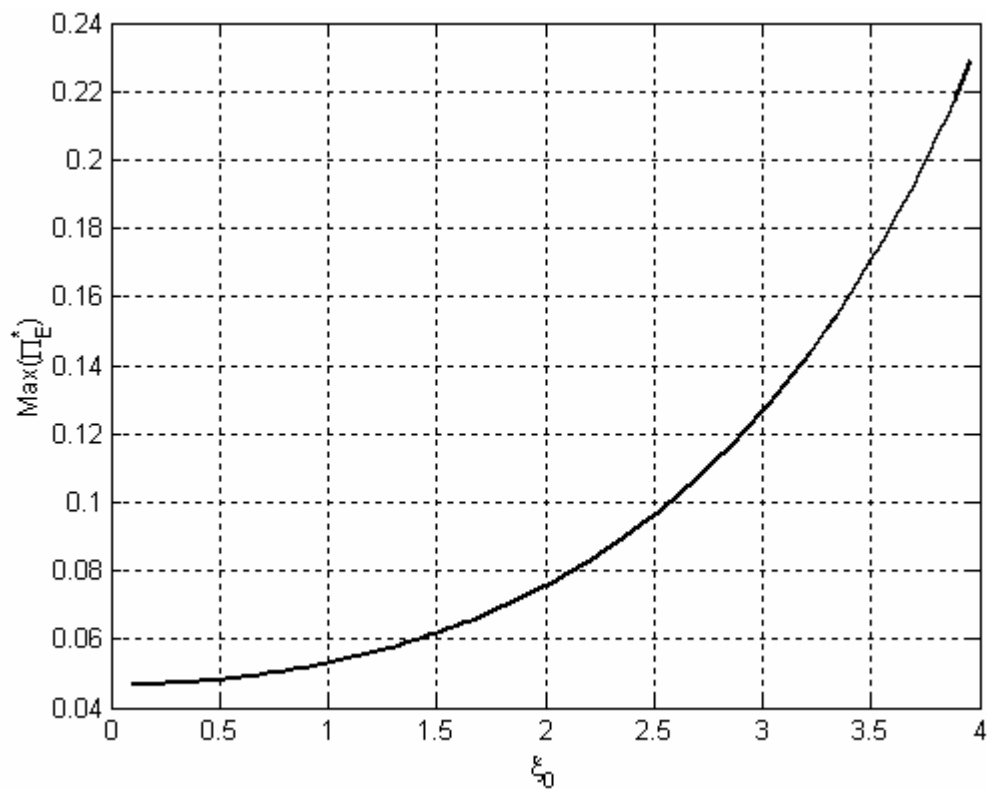
Fig. 26. Maximum non-dimensional electrochemical stored energy $\left(Max\left(\Pi_E^*\right)\right)$ vs. ξ_0
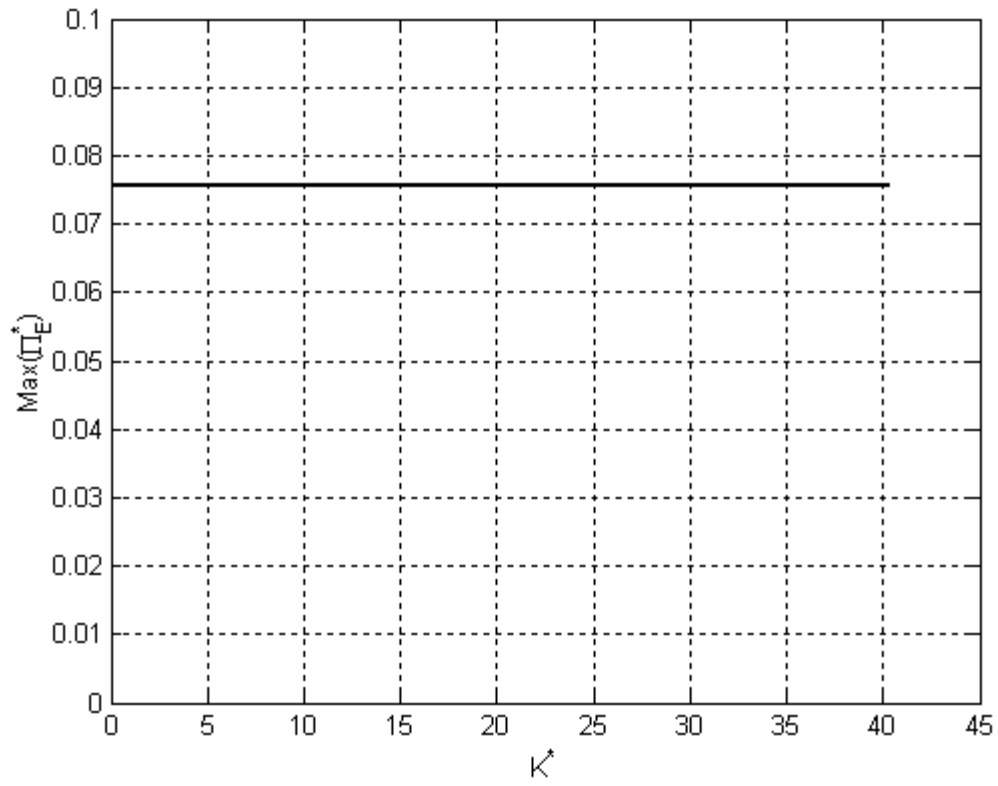
for given $A_h^* = 0.2$, $K^* = 20$.

Fig. 27. Maximum non-dimensional electrochemical stored energy $\left(Max\left(\Pi_E^*\right)\right)$ vs. K^*

for given $A_h^* = 0.2$, $\xi_0 = 2$.
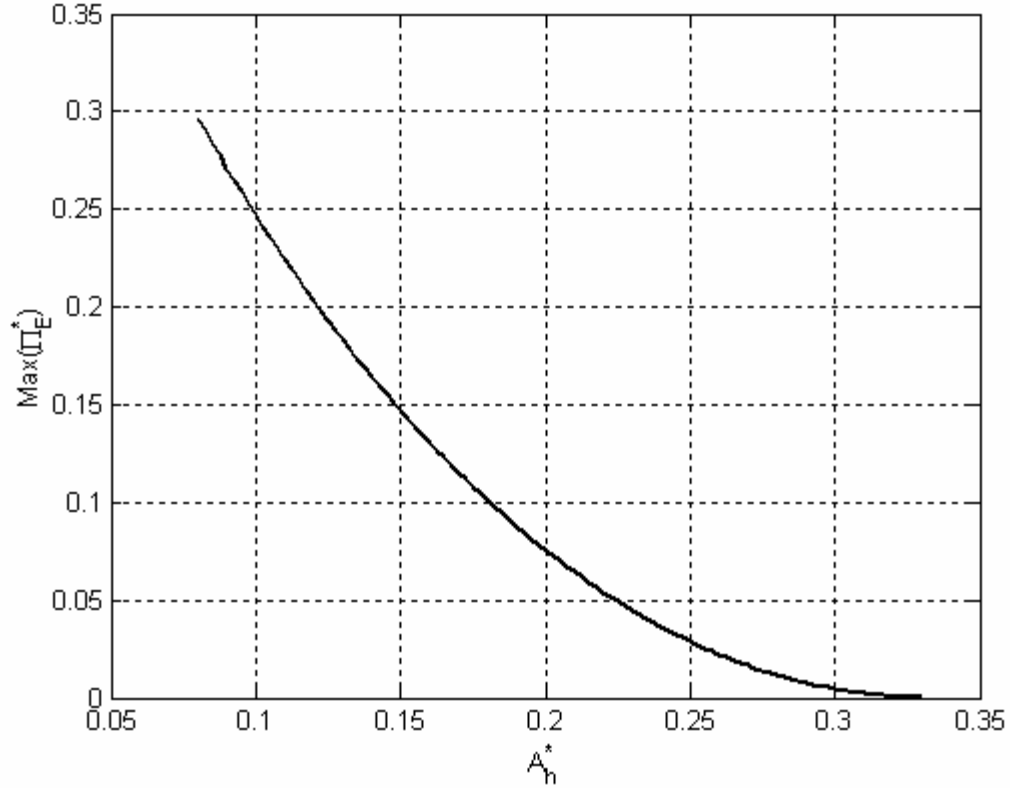
Fig. 28. Maximum non-dimensional electrochemical stored energy $\left(Max\left(\Pi_E^*\right) \right)$ vs. A_h^*

for given $K^* = 20$, $\xi_0 = 2$.

In Fig. 29, $R_1 \left(\dfrac{\Delta\Pi_s^*}{Max\left(\Pi_E^*\right)}$ or $\dfrac{\Delta\Pi_s}{Max\left(\Pi_E\right)} \right)$ decreases because $Max\left(\Pi_E^*\right)$ increases and

$\Delta\Pi_s^*$ decreases as ξ_0 increases. As ξ_0 increases h_{cri}^* increases and then it makes $\Delta\Pi_s^*$

decrease. The absolute value of $R_2 \left(\dfrac{\Delta\Pi_{vdw}^*}{Max\left(\Pi_E^*\right)}$ or $\dfrac{\Delta\Pi_{vdw}}{Max\left(\Pi_E\right)} \right)$ decreases because

$Max\left(\Pi_E^*\right)$ increases and absolute value of $\Delta\Pi_{vdw}^*$ decreases as ξ_0 increases. $\Delta\Pi_{vdw}^*$ is

very dominant at the small ξ_0 region. The absolute value of R_3 $\left(\dfrac{\Delta\Pi_{vdw}^*}{\Delta\Pi_s^*} \text{ or } \dfrac{\Delta\Pi_{vdw}}{\Delta\Pi_s} \right)$

increases as ξ_0 increases. R_1, R_2, and R_3 are function of h_{cri}^* for given A_h^* and ξ_0. And

h_{cri}^* is constant regardless of K^* for given A_h^* and ξ_0. So Fig. 30 shows that R_1, R_2, and

R_3 are constant with respect to K^*. Fig. 31 shows that the absolute values of R_2 and R_3

increase because of the large van der Waals interaction energy compared to the

maximum stored energy in double layer system and the energy stored in elastic spring.

And R_1 decreases slightly as A_h^* increases.
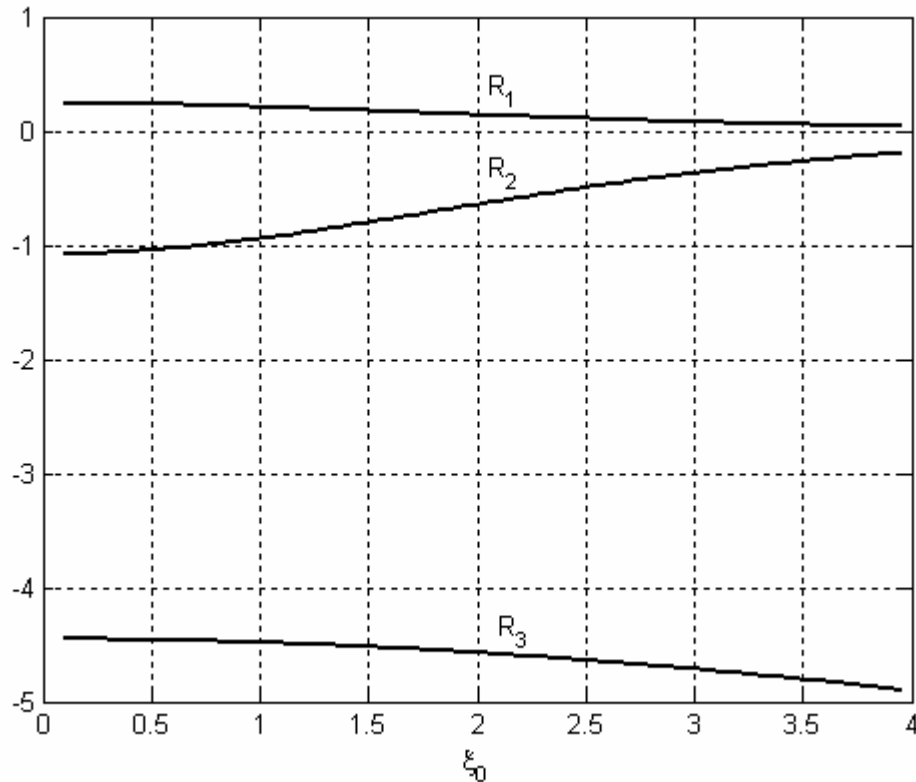
Fig. 29. R_1, R_2, and R_3 vs. ξ_0 for given $A_h^* = 0.2$, $K^* = 20$.
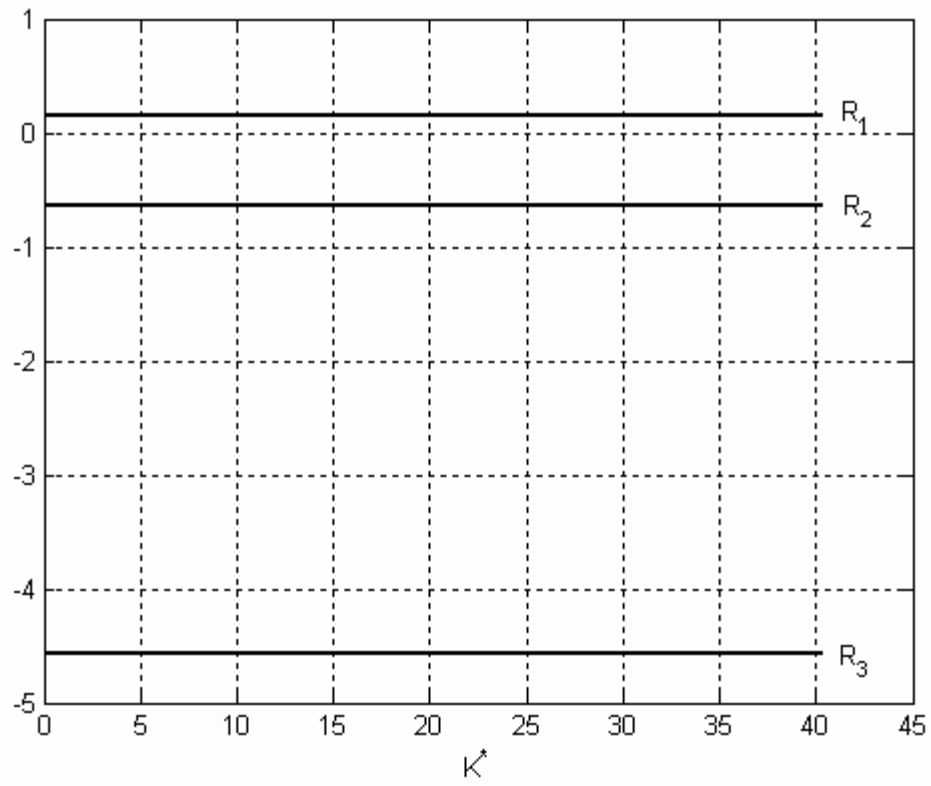
Fig. 30. R_1, R_2, and R_3 vs. K^* for given $A_h^* = 0.2$, $\xi_0 = 2$.
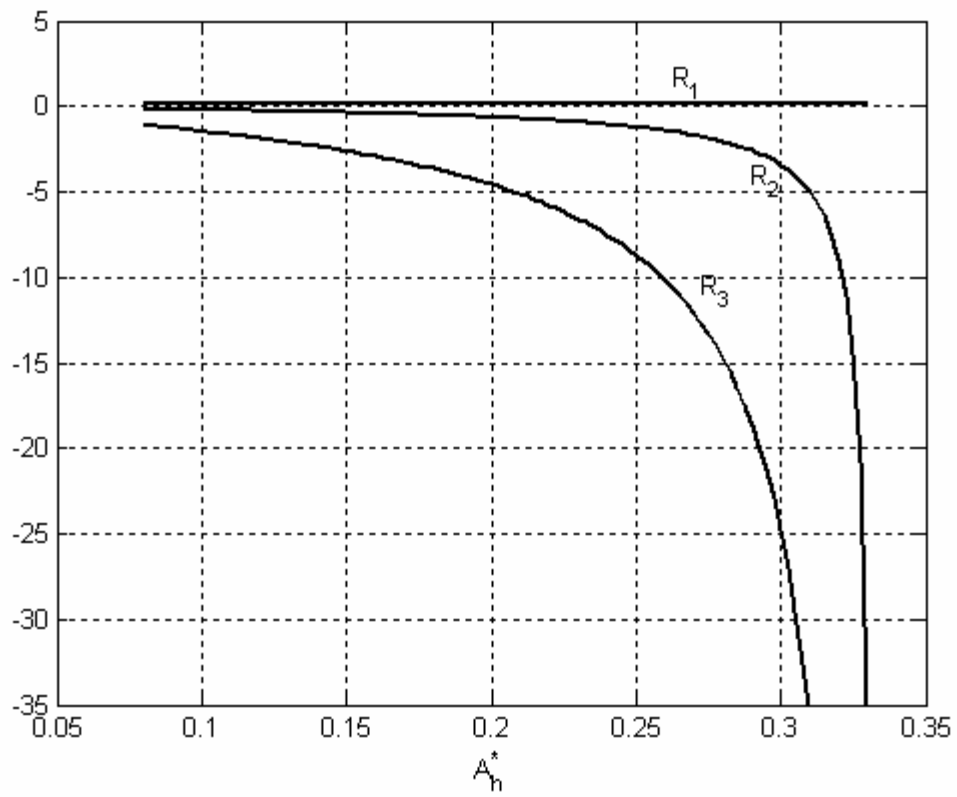
Fig. 31. R_1, R_2, and R_3 vs. A_h^* for given $K^* = 20$, $\xi_0 = 2$.

III. EXPERIMENT

A. *Literature review*

Many experiments have been done in order to explain the double layer interaction forces in an aqueous electrolyte. These forces play an important role in physical chemistry, biology, engineering, and many industrial processes. Double layer forces stabilize colloids or emulsions, preventing the flocculation of particles. They are one of the reasons for the swelling of clays, and they influence the conformation and function of biomolecules. In addition, the double layer force contains valuable information about the behavior of the chemical nature double layer itself [26].

The advent of the atomic force microscope (AFM), modified to measure forces in liquids, has enabled easier studies of the structure and behavior of various electrochemical interfaces. Experimentalists have used the AFM to measure the force versus separation curves between surfaces in liquid electrolytes, but to our knowledge, no one has experimentally determined the electric potential versus separation curves [27].

For example, Ishino in 1994 controlled the electrical potential of a gold-coated cantilever and measured forces between the cantilever and the glass substrates covered with different monolayers [28]. Hillier in 1996 varied the potential of a gold substrate and measured its interaction with a silica particle, showing that forces followed Derjaguin-Landau-Verwey-Overbeek (DLVO) theory; they also studied the relationship

between the point of zero force and the point of zero charge as a function of external

potentials [29]. Raiteri in 1996 applied electrical potential on a gold substrate and

measured its interaction with a nonconducting silicon nitride tip with high electric

potentials in aqueous electrolyte solution using AFM. They investigated surfaces at high

potentials and observed a very steep increase in forces over a small potential window

[26]. Later Raiteri in 1997 measured the force between a gold sample and a gold sphere

attached to the end of AFM cantilever to measure interaction forces between surfaces

with same high electric potentials in aqueous electrolyte solutions [27]. A similar effect

was seen by Arai and Fujihira (1996), who controlled the potential of both interacting

surfaces; however, their theoretical fits indicated values of surface potential higher than

expected [30]. Frechette and Vanderlick in 2001 studied force between mica and

polycrystalline gold under potential control using SFA (Surface Force Apparatus). The

interactions were a strong function of the applied electrode potential [31].

Doppenschmidt and Butt in 1999 measured interaction forces between surfaces of highly

oriented pyrolytic graphite (HOPG), which served as the working electrode, and a

silicon nitride tip with high electric potentials in aqueous electrolyte solution using AFM

[32]. Barten in 2003 measured the electric double layer interactions between a gold

electrode and a spherical silica probe using AFM. The double layer properties of the

gold/solution interface were varied through the pH and salt concentration of the

electrolyte, as well as by externally applying an electric potential [33]. Gold surfaces

were studied in aqueous solutions by streaming potential measurements and colloidal-

probe AFM force measurement for understanding the effect of externally applied

potentials on the adsorption behavior of charged species [34]. The surface charge at the interface of an Au electrode with a $KClO_4$ solution was measured by in situ AFM [35]. Ederth in 2001 studied long-range hydrophobic interactions with hydrophobic surfaces onto gold. For very stable hydrophobic surfaces the contact angle is sufficient to predict the presence of an attraction in excess of van der Waals, in which case the attraction is caused by the coalescence of microscopic bubbles on the surfaces. For the less-stable hydrophobic films, the properties of the adsorbed layer are important for the qualitative nature of the interaction. For such surfaces different-and as yet unknown-mechanism cause the attraction [36].

In this study, we will study the electrostatic actuator in liquid electrolytes using AFM like Fig. 32 and find the critical separation and critical applied potential. The AFM cantilever, gold sphere on the AFM cantilever, and flat gold plate in experiment play same role in elastic spring, moving electrode, and fixed electrode. Nano scale separation between two electrodes can be obtained using the AFM.
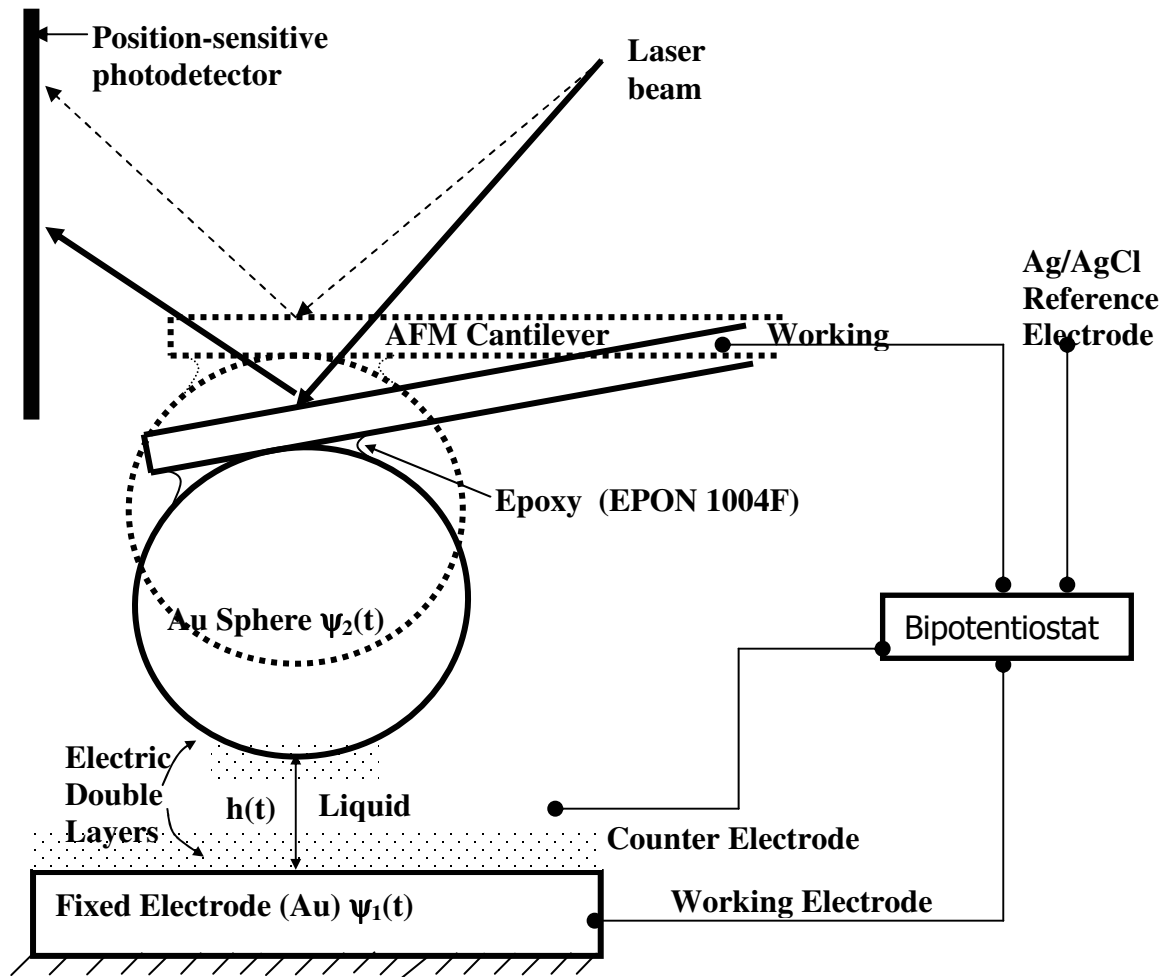
Fig. 32. Schematic drawing of experiment.

B.   Experimental description

The deflection at the end of AFM cantilever-applied potentials measurements in this study were performed using a DI (Digital instruments Inc., Santa Barbara, CA) Nanoscope III atomic force microscope equipped with a standard fluid cell and a piezo scanner "E" (x, y range 12.5 μm x 12.5 μm).

Generally AFM consists of a piezoelectric scanner, a probe, a laser, and a detection system like Fig. 33. The piezoelectric scanner may be considered the most important part. The capability of this scanner to move the sample in three directions at sub-nanometer resolution provides the basis of the AFM technique. The other key feature of the AFM is the probe or tip. In contrast to radiation-based microscopy techniques, like scanning electron microscopy or classical optical microscopy, where the resolution of the images is determined by the wavelength of the radiation, in AFM the resolution is determined mainly by the size and geometry of the tip. The magnitude of deflection of AFM can be measured with the standard beam-bounce system. A laser beam reflects off the back of the cantilever onto a position-sensitive photodetector (PSPD). As the cantilever bends, the position of the laser beam on the detector shifts. The PSPD itself can measure displacements of light as small as 10 angstroms. The ratio of the path length between the cantilever and the detector to the length of the cantilever itself produces a mechanical amplification. As a result, the system can detect sub-angstrom vertical movement of the cantilever tip. A fluid cell of AFM (Nanoscope III, Digital Instruments) is used. This fluid cell was composed of a lower plate mounted on the piezo scanner, an upper lid with a colloid probe, and a silicon O-ring in between.
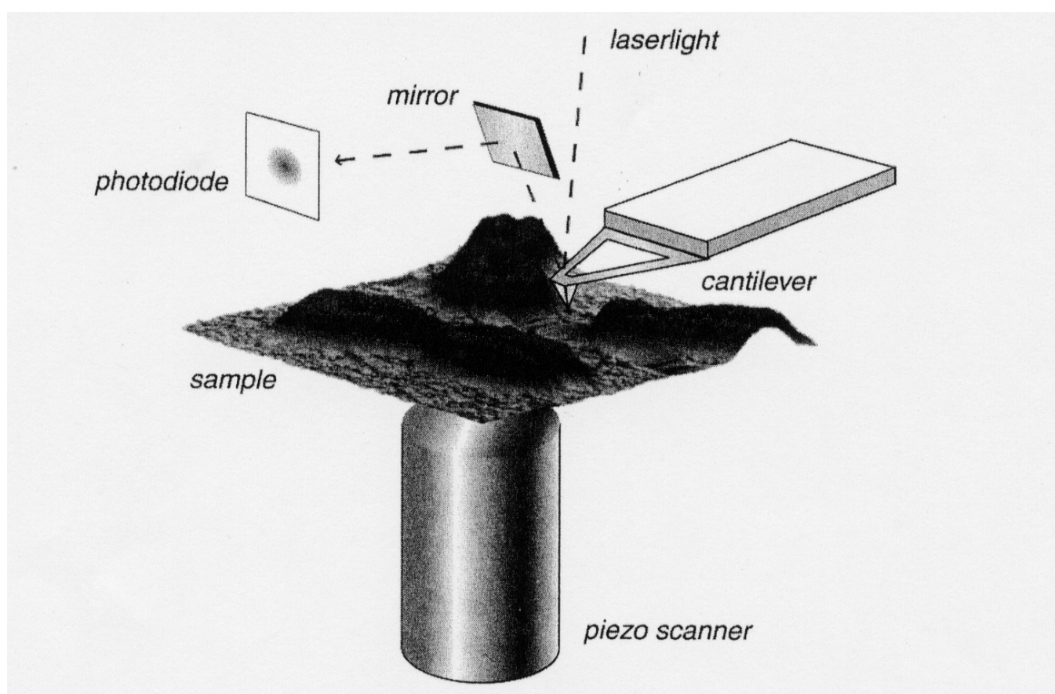
Fig. 33. Diagram of the most common AFM set-up [37].

The spheres with appropriate diameters were produced using two gold wires connected to power supply and briefly creating a short circuit (40V, max. 0.2 A). This was done under nitrogen at atmospheric pressure to avoid chemical reactions and contamination. It could be caught in a small container and consisted of gold spheres with a wide size distribution in the micrometer range. The chamber, gold wire (0.5 mm diameter), and 20 mL beaker was cleaned using cleaner (20 mL Micro 20 and 1 L DI water). The chamber with 20 mL beaker inside and two Al electrodes was prepared. The electric wires and gas inlet and outlet were connected. The gold wires were connected to the ends of two Al electrodes. The cap was close. The nitrogen gas was flown in 10 minutes and stopped at 1 atm. The potential (40 V, 0.2 A) was applied to two electrodes

using power supplier. The distance between two gold wires was controlled rotating two Al electrodes. Small spark was produced when two gold electrodes came closer. A small aerosol cloud will be produced in the spark. It can be caught in 20 mL beaker and consisted of cold spheres with a wide size distribution in the micrometer range. Acetone liquid was used to get together the gold spheres distributed everywhere on the beaker. Acetone liquid made the adhesion between gold spheres and beaker small. When the acetone liquid was stirred, the gold spheres in the acetone liquid got together in the middle of beaker. Acetone liquid was evaporated on the heater (100°C). Many gold spheres can be seen with optical microscope like Fig. 34.
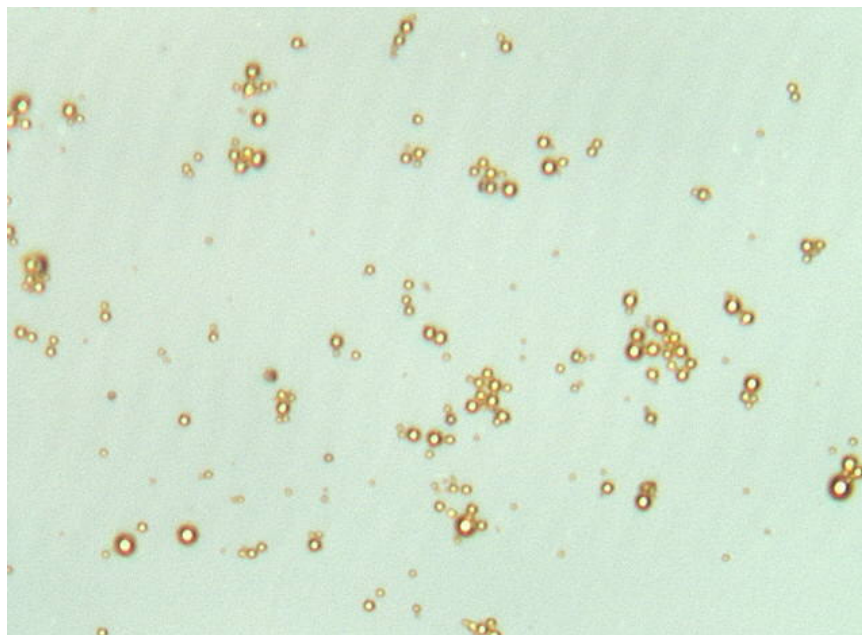
Fig. 34. Optical micrograph of the gold spheres.

Gold spheres were attached on the AFM cantilever (Veeco Instrument Inc., Santa Barbara, CA) using epoxy resin. The glue used for this purpose was an epoxy resin, EPON 1004F (Shell) which has a melting point of about 100 °C and is highly insoluble in water.

To glue a gold sphere to a cantilever, first a tungsten wire (0.25 mm diameter) was etched by immersing one end in 1 M KOH (1 L DI water and 56 g KOH) and applying an a.c. voltage of about 20 volts between the wire and a platinum circular electrode placed in the solution. The tungsten wire was etched at the surface of solution until the end was only about 2 μm thick like Fig. 34 (c). After etching the wire was rinsed in ethanol, dried in a stream of nitrogen and clamped in the micromanipulator like Fig. 35 (b).

A small heater was fixed between two glass slides using scotch tape like Fig. 35 (b). As Fig. 35 (c) is shown, an epoxy resin particle, a cantilever and a lot of gold spheres are prepared within 5mm x 5mm area on the glass slide, which was placed on the small heater under the microscope. The heating glass slide was kept at a temperature of about 150 °C (a.c. 65 V), sufficient to melt the glue particles. It takes almost 30 minutes. Using the micromanipulator the sharp tungsten wire was dipped into one of the small glue droplets on the glass slide and some glue is attach to sharp end of the tungsten wire. The amount of glue on the wire can be reduced by letting it touch a clean part of the glass slide. This was repeated until only a tiny amount of glue was left on the wire. Now, the cantilever was rubbed with the glue-loaded wire tip exactly on the spot where the particle will be placed. In this way some of the glue on the wire was transferred to the

cantilever. Even if there was no glue visible on the cantilever under the microscope, there was probably enough present to hold a particle. The next step is to bring a small number of colloidal probe particles onto a clean glass slide under the microscope. The micromanipulator provided with another tungsten wire was used to bring a single particle to the cantilever. Generally, the particle was readily picked up when touched as a result of capillary adhesion between the thin water films on the wire and the particle, which are always present under ambient conditions. But in my experiment, the particle was hard to pick up and place because the particle moves away from the tungsten wire on the hot glass slide surface.
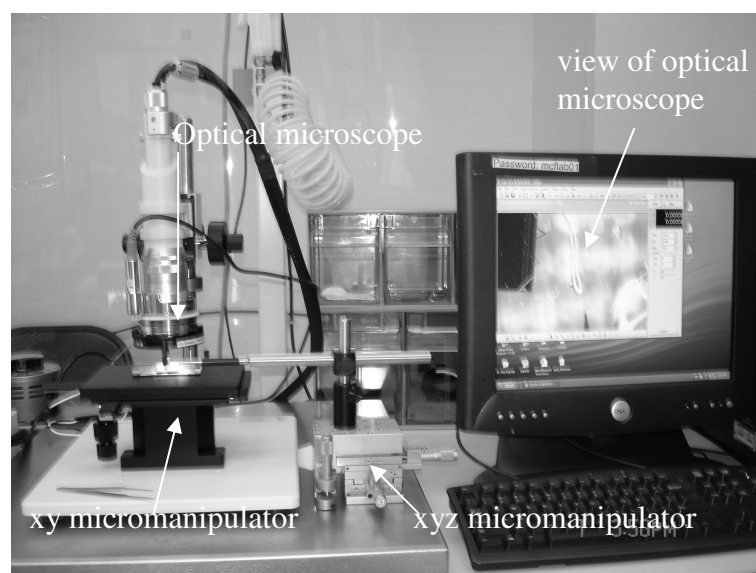
(a)

Fig. 35. (a) The set-up used to glue particles to the end of the AFM cantilever, (b) closer view under the optical microscope, and (c) microscope view
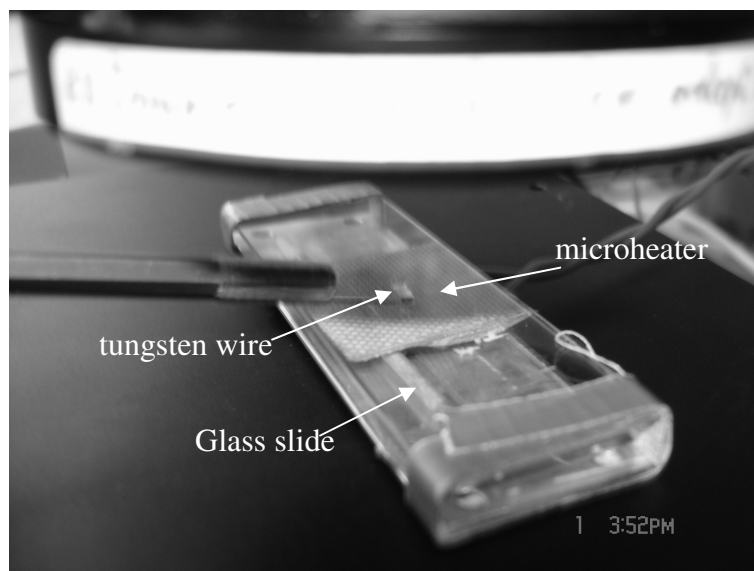
(b)
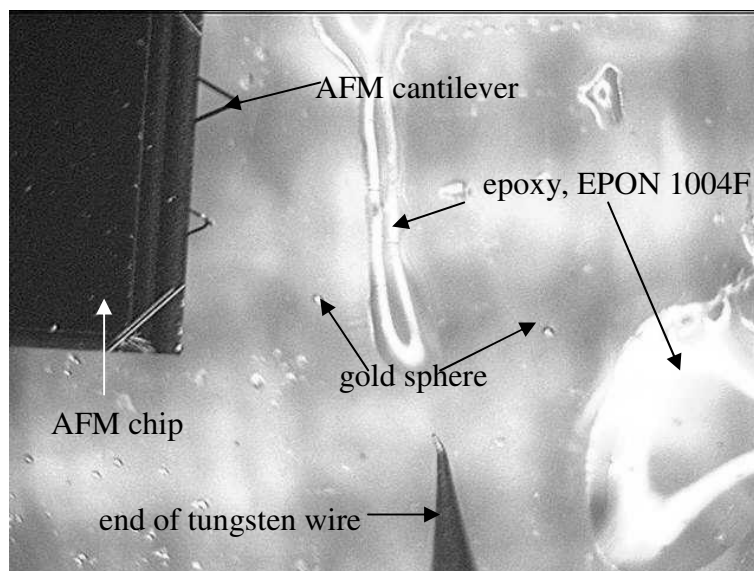
(c)

Figure 35 continued.

Next, the particle was carefully maneuvered onto the glue on the cantilever where it sticks. Finally, the cantilever was removed from the heating stage, after which the glue

hardens. It is important to attach a sphere at the same location on the cantilever tip for the excellent reproducibility. Fig. 36 shows the AFM cantilever with a gold sphere.

Roughly 10 nm of gold is sputtered onto the cantilever and the attached sphere in order to create a conductive path to the metallic spring clip, which holds the cantilever clip. Care was taken to avoid coating the reflective gold side of the cantilever.

A well-defined geometry simplifies the modeling of the probe/sample interaction (the main drawback is a loss in lateral resolution). The Langbein approximation is used for the effective area. The Langbein approximation is valid when the radius of gold sphere is much larger than the separation between the gold sphere and gold flat plate.
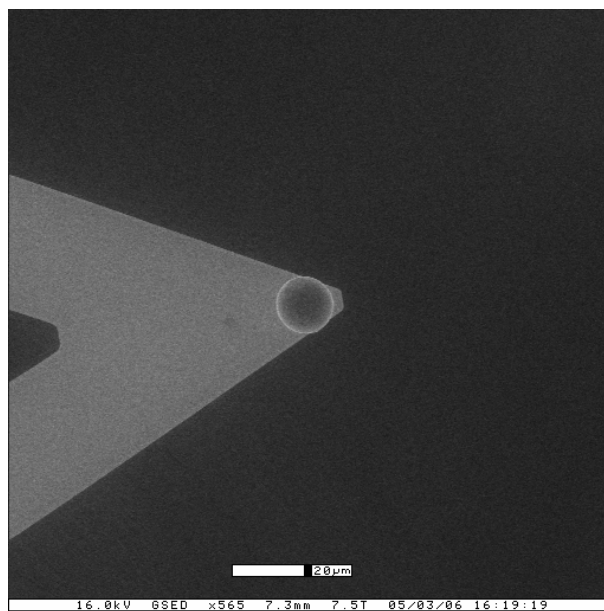
(a)

Fig. 36. (a), (b) Scanning electron micrographs, (c) optical micrograph of gold particles attached to AFM cantilevers.
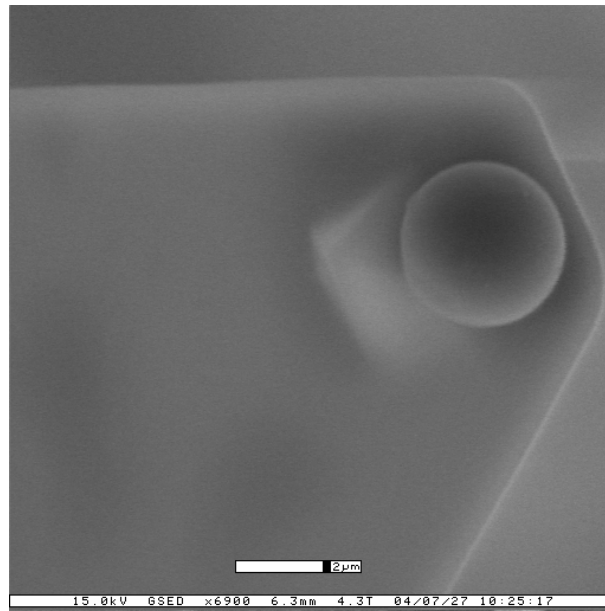
(b)
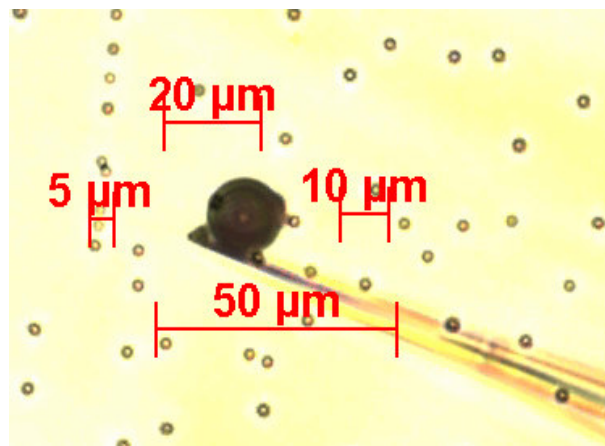
(c)

Figure 36 continued.

According to Langbein approximation, the effective area will be $2\pi R h_0$ (R is the radius of gold sphere, h_0 is the initial separation between two electrodes).

The cantilevers used throughout this work were obtained from Digital Instruments (Santa Barbara CA, USA). The cantilevers are mounted on a substrate or chip. Four types of cantilevers are provided on one substrate: 100 µm long wide-legged, 100 µm long narrow-legged, 200 µm long wide-legged, and 200 µm long narrow-legged. Digital Instruments specifies the spring constants of the various cantilever types, but the values provided are only approximate. Some variations in thickness, width, and length of the cantilever may results into large differences in the spring constants of cantilevers of the same type. Therefore, for accurate force measurements and comparison with theory is necessary to precisely determine the spring constant of each individual cantilever.

In this research, the Cleveland method was used for the spring constant K of each AFM cantilevers [38]. The V-shaped cantilevers can be well approximated by two rectangular beams in parallel. Two obvious sources are the measurement of the gold sphere diameters and the fact that the spheres were only positioned within 20 µm of the integrated tip (where forces will be applied during imaging). Both these errors could be minimized by the use of precalibrated masses (e.g., monodisperse spheres) and more careful positioning [38]. The spring constant of an end-loaded cantilever beam of rectangular cross section is given by $K = \dfrac{Et^3 w}{4l^3}$, where E is the elastic modulus, t is thickness, w is the width, and l is the length. This effective mass is $m^* \approx 0.24 m_b$ where m_b is the mass of the beam. When an end mass M is added, the resonant frequency is given by $v = \dfrac{\varpi}{2\pi} = \dfrac{1}{2\pi}\sqrt{\dfrac{K}{M + m^*}}$ or $M = K(2\pi v)^{-2} - m^*$. This equation shows that if

several known end masses are added to a cantilever and the new resonance frequencies are measured, a linear plot of added masses versus $(2\pi v)^{-2}$ should give a straight line, the slope being the spring constant and the negative y intercept the effective mass. The unloaded resonant frequency ($M = 0$) can be written using $m_b = \rho wtl$,

$$v_0 \approx \frac{t}{4\pi l^2}\left(\frac{E}{0.24\rho}\right)^{\!1/2} \approx \frac{t}{2\pi l^2}\left(\frac{E}{\rho}\right)^{\!1/2}.$$ Using measurements of the unloaded resonant

frequency v_0 and the resonant frequency v_1 with one added mass M_1, these two equations,

$0 = K(2\pi v_0)^{-2} - m^*$ and $M_1 = K(2\pi v_1)^{-2} - m^*$ are obtained. Finally spring constant and

effective mass can be determined like, $K = 4\pi^2 \dfrac{M_1}{\left(1/v_1^2\right) - \left(1/v_0^2\right)}$ and $m^* = M_1 \dfrac{v_1^2}{v_0^2 - v_1^2}$.

In principle, measuring the resonance frequencies of the unloaded cantilever and the loaded cantilever for just on value of M would suffice to calculate K. However, in practice more measurements are needed to reduce the effect of experimental errors, in particular those related to determine the precise size of the gold particle. The resonance frequency of the cantilever can be easily determined making use of the NanoScope software. First the resonance frequency v_0 of the unloaded cantilever is determined. After this a particle of known mass is attached to the cantilever, and the resonance frequency is again measured. Attaching the end mass is done in much the same way as with the colloidal probes, only this time no glue is used (in air the particles stick due to capillary adhesion). As end masses, gold spheres with diameters in the range 7 ~ 25 μm were used. The masses of the gold spheres were calculated from the sphere radii and the density of gold (19.3×10^3 kg/m^3). The diameter of each gold sphere was measured using optical

microscope (Hirox microscope, 600× magnification) in the lab. 5 resonance frequencies for 5 different gold spheres were obtained, and then the spring constants of each AFM cantilever were determined. Fig. 37 shows an example of typical cantilever calibration plot.
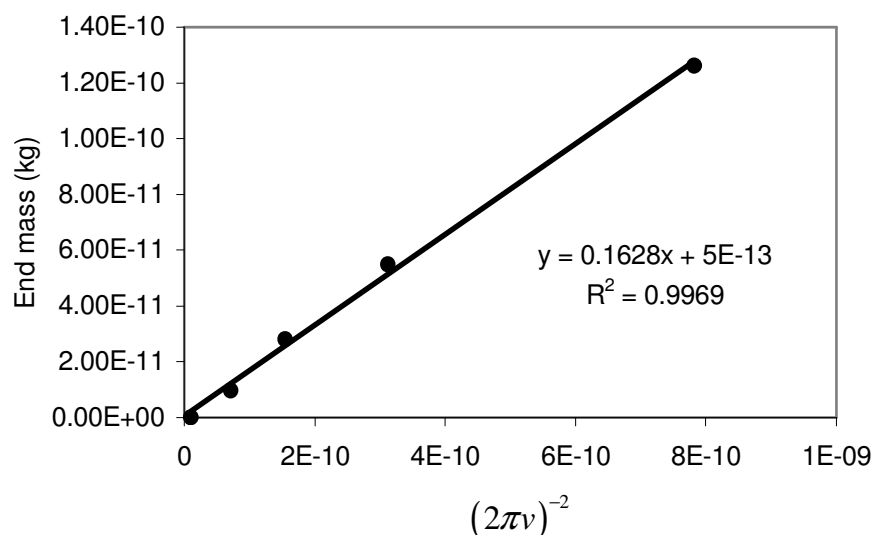
Fig. 37. Typical cantilever calibration plot for a standard 115 μm narrow-legged Vecco cantilever. Spring constant 0.163 N/m and correlation coefficient 0.9969.

Flat gold electrode surfaces were prepared by evaporating about 5 nanometers of chromium to prevent gold detaching from the silicon substrate (100) in water and 50 nanometers of gold over silicon substrate like Fig. 38. Gold source (Au 99.999%) is from CERAC. In order to apply the external potentials, 200 μm conducting wire was connected to each flat gold electrode using conducting epoxy.
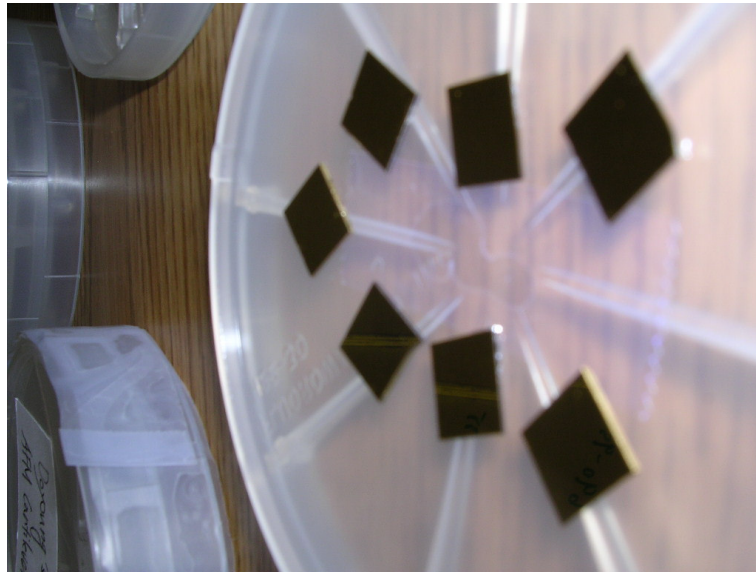
Fig. 38. Flat gold samples.

The surface roughness of the flat gold electrode surfaces and the gold sphere was measured using an AFM. To measure the surface roughness of gold spheres, 10 nm gold surface on the dummy silicon (100) was used instead of the surfaces of gold spheres. This gold surface was deposited at the same condition as the thin gold layer was deposited using sputtering. The surface roughness was determined by AFM in imaging mode and defined as the root mean square (rms) of the height differences on the surface over an area of 1 μm^2. The AFM image indicated that the root-mean-square roughness over a 1×1 μm^2 area was about 1 nm for the relatively flat gold surfaces and the peak-to-peak roughness was about 20 nm. Fig. 39 shows an example of a gold surface roughness and in this case, rms roughness is about 1 nm and peak from the average height is about 7.4 nm.

(a)

(b)

Fig. 39. A example of roughness analysis of flat gold surface. (a) 2-D view, (b) 3-D view.

Scan area: 1 μm^2, rms roughness: 1.063 nm, peak from average height: 7.366 nm.

An aqueous solution of 1 mM salt (NaCl) and deionized pure water were used. Nitrogen was bubbled through the solution for at least 30 minutes to deaerate the solution and to remove dissolved CO_2 which would decrease the pH. After this, the measured pH was 5.7 ± 0.05 at 25 ºC (298 K). Approximately 10 mL of the solution was rinsed through the AFM cell, after which the inlet and outlet of the cell were closed.

The Teflon tubing and the electrochemical cell were rinsed with ethanol and DI water. The flat gold surfaces were cleaned by immersion into a piranha solution, i.e., a hot mixture of 30 % H_2O_2 and concentrated H_2SO_4, for 2 mins, which resulted in a surface with a zero contact angle with water. To avoid detachment of the gold-coated particles from the cantilever, these were not cleaned with piranha solution but in plasma cleaner. The flat gold surfaces and the cantilever with the gold sphere were put under the UV light (254 nm) in the clean room for at least 15 minutes then were washed in distilled ethanol, rinsed with purified water and then blown dry with nitrogen.

The zero of force was chosen where the deflection was constant (where the particle and flat were far apart), and the zero of distance was chosen to occur when the cantilever deflection was linear with respect to sample displacement assuming there is no interaction between the particle and flat sample (in real, there exist always repulsive or attractive interaction between them). As the sample is driven toward the sphere, the cantilever deflects, and this is registered by the photodiode. At some point, the output of the diode becomes a linear function of the sample displacement because the particle is in contact with the surface and thus the changes in displacement of the sample are equal to changes in deflection of the cantilever. This linear region of deflection is called the

region of constant compliance. In this experiment, the zero of distance was chosen by the intersection of the extended line of the region of constant compliance and the extended line of the zero of force.

A platinum counter electrode and an Ag/AgCl (in 3 M KCl) reference microelectrode will be put into the inlet and outlet of the AFM fluid cell and connected to the bipotentiostat (Model 700B series Electrochemical Analyzer, CH instruments Inc., Austin, TX) like Fig. 40. The first working electrode was connected to the flat gold plate on the AFM cantilever and the second electrode was connected to the gold sphere. The purpose of the reference electrode is to maintain a constant reference potential regardless of change in pH or other ionic activity in the solution. All the potentials applied to an electrode can only be referred to a reference electrode. In experiments where iR_s may be high, a three-electrode cell arrangement is preferable. In this arrangement the current is passed between the working electrode and a counter electrode. The device used to measure or monitor the potential difference between the working electrode and the reference electrode has high input impedance so that a negligible current is drawn through the reference electrode. Since essentially no current is passed through the reference electrode, its potential will remain constant and equal to its open-circuit value.
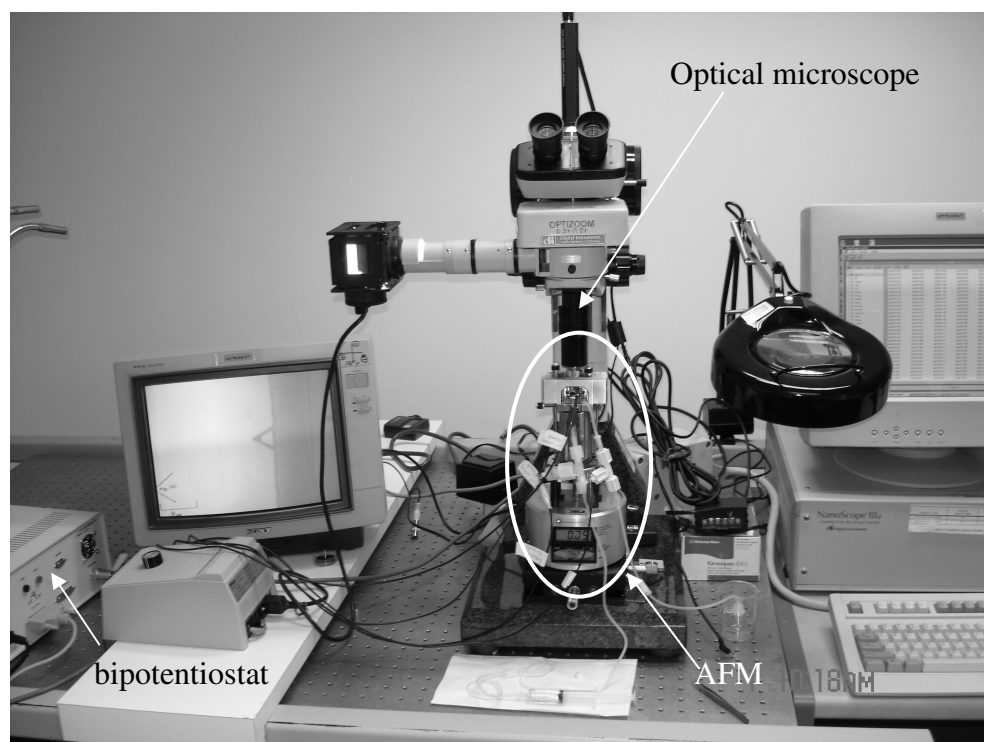
(a)
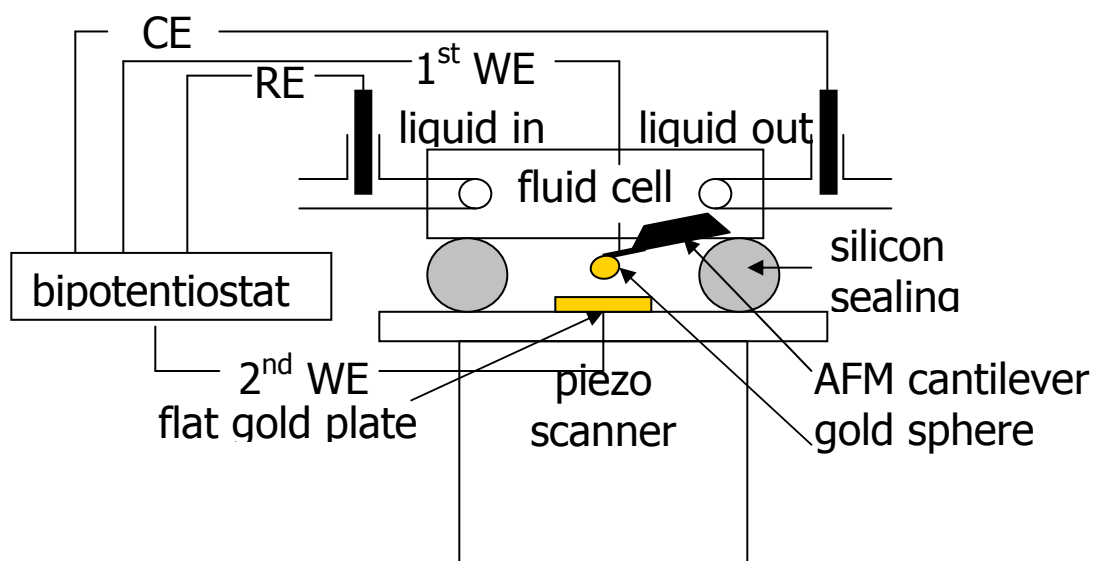
(b)

Fig. 40. (a) Experimental set up picture, (b) schematic drawing of experimental set up,

and (c) AFM and electrodes.
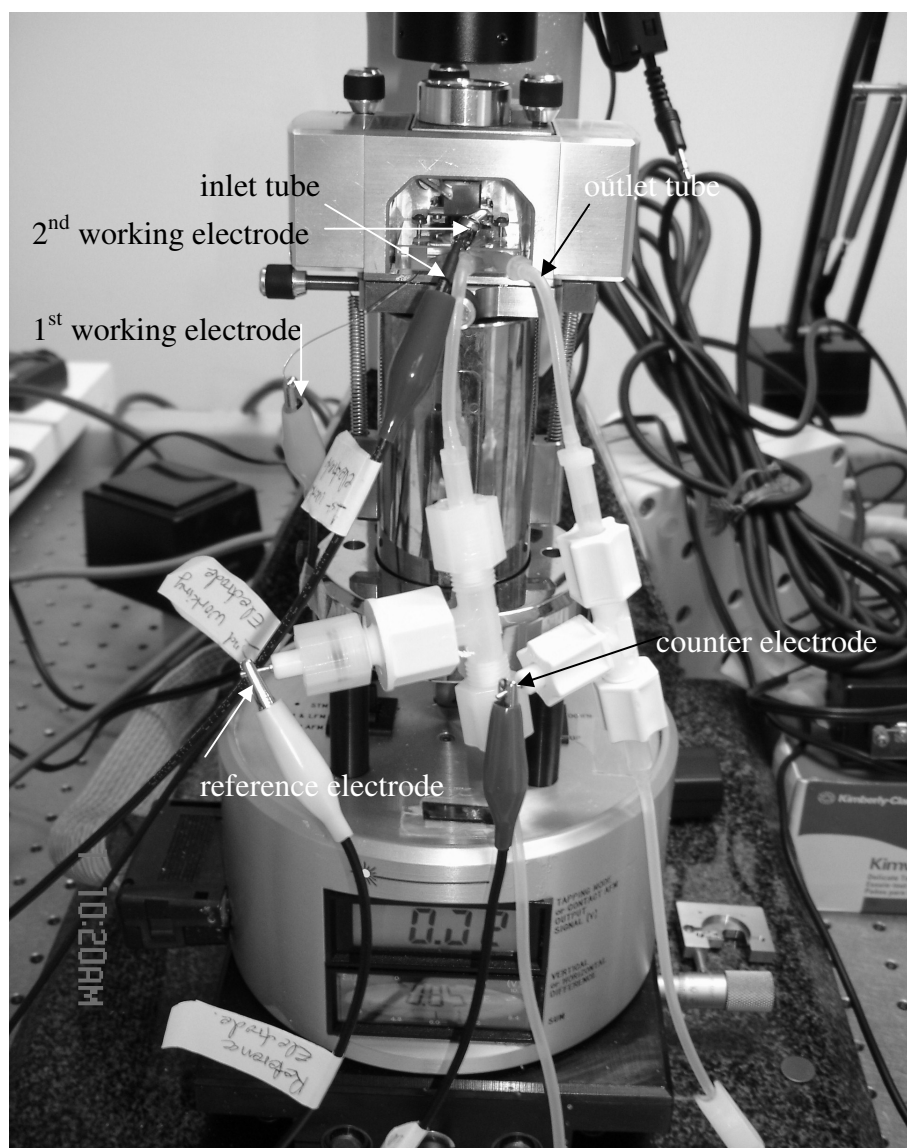
(c)

Figure 40 continued.

First, without external potentials, the continuous force measurements with a frequency of 5 Hz to get the position of gold sphere on the AFM cantilever from the flat

gold sample and deflection sensitivity which represents the cantilever deflection signal versus voltage applied to the piezo and is normally set from the force plot mode in AFM.

During force measurements in the AFM, the tip (with or without a colloidal probe) and a flat surface are continuously brought into contact and separated again. The piezo element moves only in the z-direction; the x and y positions are fixed. Since the flat surface was mounted on the piezo element, the flat surface was brought towards the cantilever rather than the cantilever towards the surface. Forces acting between the surfaces will cause the cantilever to deflect. The deflection of the cantilever was monitored and plotted in a graph is shown in Fig. 41. On the vertical axis the output of the photodiode was plotted and horizontal axis gives the position of the piezo. The curve I-II-III gives the interaction on approach and the other (with the deep minimum) corresponds to the interaction upon retraction. At large distance (I) no force acts on the particle. When bringing the surface closer the particle feels an attraction or a repulsion which causes the cantilever to bend towards or away from the surface (II) (in Fig. 41, an attraction is depicted). When the particle and flat surface have come into contact (provided the surfaces do not indent – or do not indent anymore), the particle movement complies to the movement of the piezo. This implies that when the piezo is moved upwards over a certain distance the probe is moved upwards over the same distance (III). Consequently, the measured deflection is linear with the piezo movement which shows up as a linear region in the force plot. This part of the curve is called the constant compliance region. At the end of this constant compliance region the piezo movement is reversed. If there is an adhesion between the surfaces a force is needed to separate them.

This is illustrated in Fig. 41: on retraction the surfaces are in contact beyond the point where initial contact was made (IV). As the piezo is moved further downwards the surfaces are separated again. At larger distances the force between the tip or probe and the surface is again zero (V) [37].
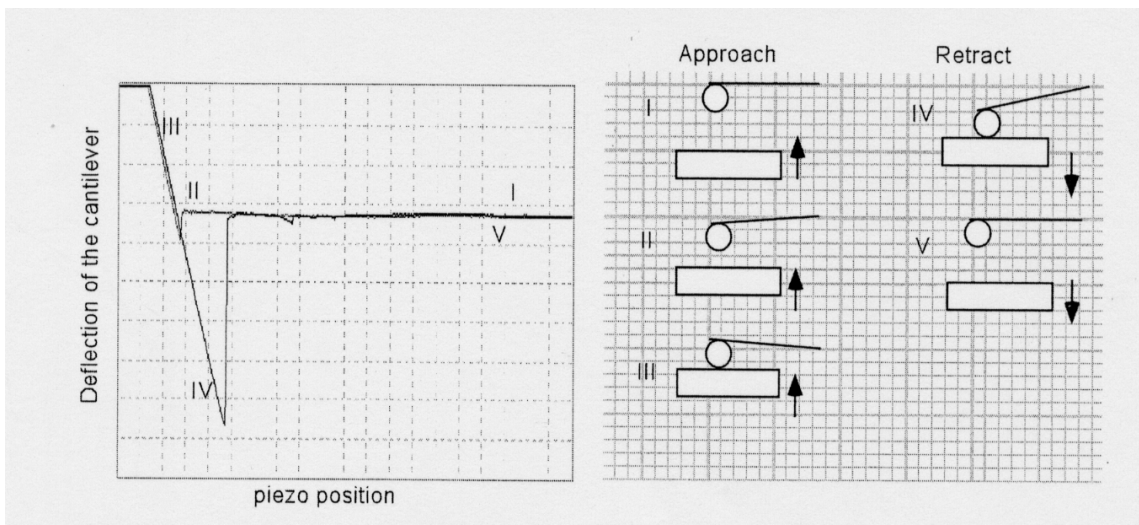
Fig. 41. A typical force graph in which the deflection of the cantilever is plotted against the piezo position. On the right, the position of the colloidal probe and the flat surface on the piezo are shown for several points of the curves, indicated by Roman numerals [37].

The deflection sensitivity is equal to the slope of the force curve when the cantilever is in contact with the sample surface. So, this sensitivity can be expressed in terms of the photodiode voltage versus the distance traveled by the piezo, or the photodiode voltage versus the voltage applied to the piezo. Therefore we can know how many voltages of deflection signal are produced by a given deflection of the cantilever tip. The sensitivity will change for different cantilever lengths and styles and with the position of laser on

the cantilever and the quality of the laser beam reflection from the cantilever. During the acquisition of a force curve and deflection of end of cantilever, the measured experimental parameters are the output signal of the photodiode (in volts) which is directly related to the tip deflection. This can be calibrated by comparing the detector signal to the piezo displacement in the constant compliance region and the substrate displacement in nanometers [33]. This sensitivity was measured 10 times for each experiment and the average was used for the deflection sensitivity. Using the step motor of AFM, initial separation between gold sphere on the AFM cantilever and flat gold sample was set and then the ramp size of AFM scanner under the flat gold sample was set to zero to get the fixed electrode. With these processors, we have two electrodes, that was, a gold sphere on the AFM cantilever as movable electrode and a flat gold plate as fixed electrode with separation, h_0.

Then potentials are applied to electrodes using staircase among bipotentiostat functions. The positive potential to the movable electrode has initial potential of zero, increment of potential of each step of 10 mV or 50 mV, and a potential step period of 100 seconds. The negative potential to fixed electrode has initial potential of zero, decrement of potential of each step of 10 mV or 50 mV, and a potential step period of 100 seconds. These potentials are with respect to the Ag/AgCl reference electrode. The output voltage of the deflection of each applied potential was measured and this output voltage was converted into the deflection using deflection sensitivity. Finally, the deflections of the end of the AFM cantilever versus the applied potentials for different AFM cantilevers and different gold spheres on the AFM cantilever were measured.

All the potentials applied to an electrode can only be referred to a reference electrode. On the other hand, in the analytical calculation, the surface potential, which is referred to the bulk of the solution, is relevant.

There are systematic errors and errors in the data analysis presented here which limit the resolution. Therefore, a sensitivity analysis of the individual parameters was performed. In this experiment, the spring constant of the AFM cantilever, distance between gold sphere and flat gold plate, potentials applied to two electrodes, and radius of gold sphere are very important parameters rather than other parameters like permittivity of water, valence of each ions, temperature and bulk concentration, which have very small errors.

The true value of a measurand is the real world value. Because our instruments do not perfectly measure this real world value, the true value of the measurand is never known. The indicated value of the measurand is the value given by the instrument. The error is the difference between the indicated value and the true value. Because the true value is never known, the error is also never known. Therefore, we define a term called the uncertainty, which is a range in which we believe the error to lie.

Given the uncertainty in the measurands, we must calculate the uncertainty in a function of those measurands, i.e. we must calculate how the uncertainty propagates. Generally, the uncertainty of the measurement is estimated analytically using uncertainty propagation methods [39]. This method is a special application of Taylor's series and can be expressed as

$$f\left[(x_1+\Delta x_1),(x_2+\Delta x_2),\cdots,(x_n+\Delta x_n)\right]=f(x_1,x_2,\cdots,x_n)+\Delta x_1\frac{\partial f}{\partial x_1}$$

$$+\Delta x_2\frac{\partial f}{\partial x_2}+\cdots+\Delta x_n\frac{\partial f}{\partial x_n}+\text{ higher-order term}$$

where the x_n's are variables and the Δx_n's are determined or assumed incremental variations in the respective x_n's. The higher-order terms are neglected. This equation can be rewritten, changing the Δx_n's to u_n's merely to represent uncertainties better:

$$f\left[(|x_1|+|u_1|),(|x_2|+|u_2|),\ \cdots\ ,(|x_n|+|u_n|)\right]-f\left[|x_1|,|x_2|,\ \cdots\ ,|x_n|\right]$$

$$=u_f=\left|u_{x_1}\frac{\partial f}{\partial x_1}\right|+\left|u_{x_2}\frac{\partial f}{\partial x_2}\right|+\ \cdots\ +\left|u_{x_n}\frac{\partial f}{\partial x_n}\right|\qquad . \qquad (87)$$

Equation (88) evaluates the overall maximum uncertainty of the function.

First, a scanning electron microscope was used to measure the radii of each gold sphere attached on the AFM cantilever. Three times measurements of radii were always the same to within the 2.5 % resolution.

Distance ($h = D.S \times V_{out}$) between the gold sphere and the flat gold plate is equal to the deflection sensitivity ($D.S$) times the output voltage of the photodiode (V_{out}). Therefore, maximum relative uncertainty of distance with respect to measured distance (U_h/h) is like

$$\frac{u_h}{h}=\frac{u_{D.S}}{D.S}+\frac{u_{vout}}{V_{out}}$$

where $u_{D.S}$ is uncertainty of deflection sensitivity and u_{vout} is uncertainty of output voltage of photodiode. The relative uncertainty of the deflection sensitivity ($U_{D.S}$ / $D.S$) is about 6 %. The relative uncertainty of the output voltage of the photodiode (U_{vout} / V_{out}) is about 0.3 %. So, the maximum relative uncertainty of distance is about 6.3 %.

For the spring constant (K) of the AFM cantilever, the Cleveland method was used and the method of least squares was used for the data analysis. Therefore, the spring constant can be expressed like

$$K = \frac{N\sum x_i y_i - \sum x_i \sum y_i}{N\sum x_i^2 - \left(\sum x_i\right)^2}$$

where $x_i = (2\pi v_i)^{-2}$ and $y_i = 3/4\pi R_i^3 \rho_{AU}$ from the Cleveland method, N is the number of data and ρ_{AU} is the density of gold. So, the spring constant is a function of ith radius of gold sphere (R_i) and i[th] resonant frequency (v_i) and maximum relative uncertainty of spring constant (u_K / K) can be expressed like

$$\frac{u_K}{K} = \frac{1}{K}\left\{\left|u_{R_1}\frac{\partial K}{\partial R_1}\right| + \cdots + \left|u_{R_7}\frac{\partial K}{\partial R_7}\right| + \left|u_{v_1}\frac{\partial K}{\partial v_1}\right| + \cdots + \left|u_{v_5}\frac{\partial K}{\partial v_7}\right|\right\}$$

where u_{R_i} is uncertainty of ith radius of gold sphere and u_{vi} is uncertainty of ith resonant frequency. Relative uncertainty of the radius of gold sphere is within 2.5 % and the

relative uncertainty of the resonant frequency is within 0.63 %. As a result, maximum

relative uncertainty of spring constant of AFM cantilever is about 5.74 %.

C. Results

1) Natural double layer repulsion

Fig. 42 shows a cantilever deflection-distance curve of gold-gold interaction in 1 mM NaCl electrolyte without externally applied electric potentials. In Fig. 42, the deflection (y-axis) is calculated using the multiplication of the displacement sensitivity (nm/V) and photodiode output (V). With this curve, the distance between the gold sphere on the AFM cantilever and flat gold sample can be obtained, and the deflection versus this actual electrode separation is shown in Fig. 43.

The gold sphere on the AFM cantilever encountered a repulsive force that decayed exponentially with decay length similar to the Debye length because two gold surfaces have same negative charges and same negative potentials with respect to that of bulk concentration in the same liquid electrolytes.
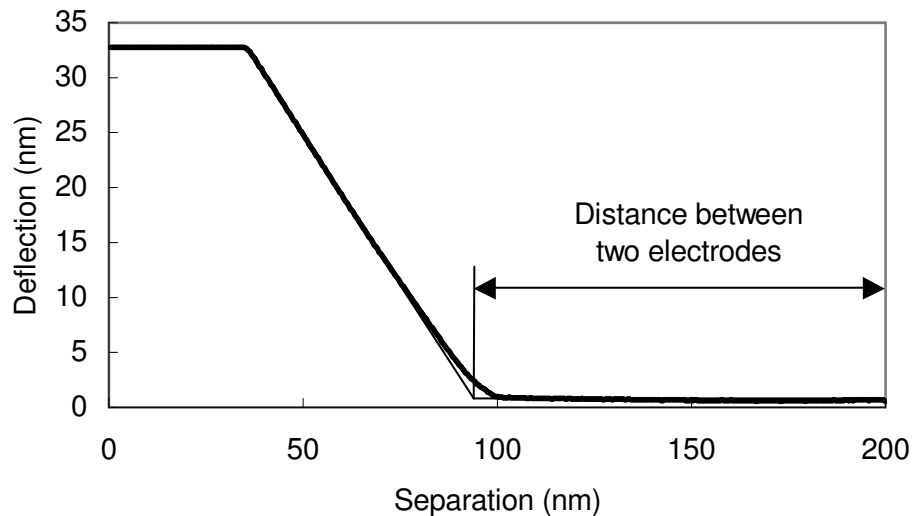
Fig. 42. The raw deflection-separation curve of gold-gold interaction in 1 mM NaCl

electrolyte without external applied potential.
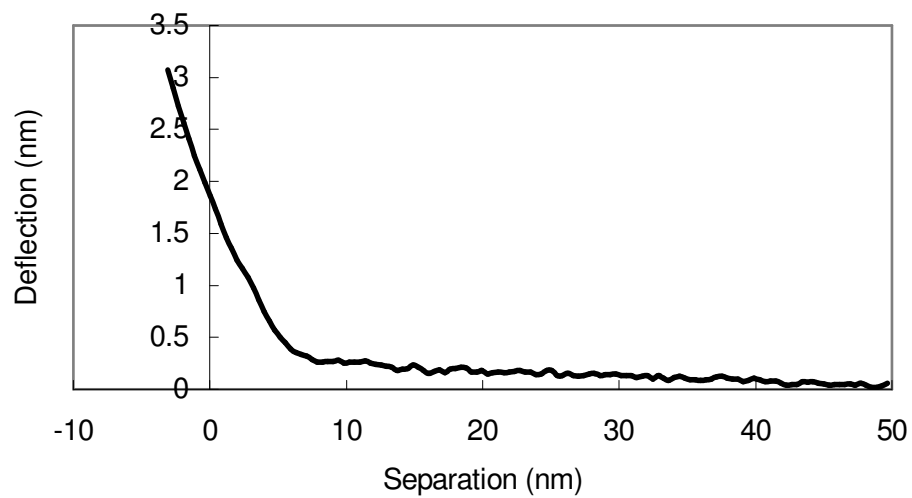
Fig. 43. The deflection versus electrode separation curve converted from Fig. 42.

The results reported herein are qualitatively similar to other results [33]. But there is a quantitative difference between our results and published results. Giesbers in 2002 mentioned that the charge and the potential of gold surfaces in solution are determined by specific ion adsorption and are highly dependent on the solution composition and presence of impurities. Furthermore, the preparation and cleaning procedure of a gold surface may affect its chemical properties (presence of oxide layers) and clean gold surfaces readily adsorb contaminants from the air. It is therefore no surprise that in literature practically no consistent data on the potential of gold surface can be found [33].

In principle, one can find the spring force from the cantilever deflection, and then set this force equal to the sum of the van der Waals force and electrochemical force like (65) in the analysis section to solve for the electric potential on the electrode. This potential is the natural potential between gold and the electrolyte. However, this is not possible in this case because our mechanical equilibrium analysis is based on the linearized Poisson-Boltzmann equation, which assumes small potentials. The natural double layer potentials of the gold surface are larger than the maximum potential of linearized Poisson-Boltzmann equation.

2) Results with externally applied electric potential

Fig. 44, Fig. 45, Fig. 46, and Fig. 47 show the deflections of the AFM cantilever versus the externally applied electric potentials, including both experimental results and the analytical results for the conditions matching the experiments.

Part (b) of these figures, the separation vs. external potentials, were obtained from analytically using the linear momentum equation at equilibrium (67). The potentials

analytically applied to electrode 1 and electrode 2 are given by $\psi_1 = -215 + \psi_1'$ and $\psi_2 = -215 - \psi_1'$, where ψ_1' is the experimentally applied external potential. The shift of potential by -215mV accounts for two phenomena: the natural double layer potential, and the effect of the Ag/AgCl electrode used in the experiment.

Ducker and Ederth measured the natural double layer potential to be –65mV for Au electrodes in 1mM NaCl aqueous solution [40], [36]. In the experiment we apply electrode potentials with respect to the Ag/AgCl electrode, whereas in the analysis we apply the electrode potentials with respect to the bulk solution potential. Barten in 1993 mentioned in his research that all potentials applied with respect to the Ag/AgCl reference electrode are shifted by –150 mV to express these with respect to the potential of the bulk solution [33]. Therefore, we use -215mV (= -65mM – 150mV) in the analytical model.
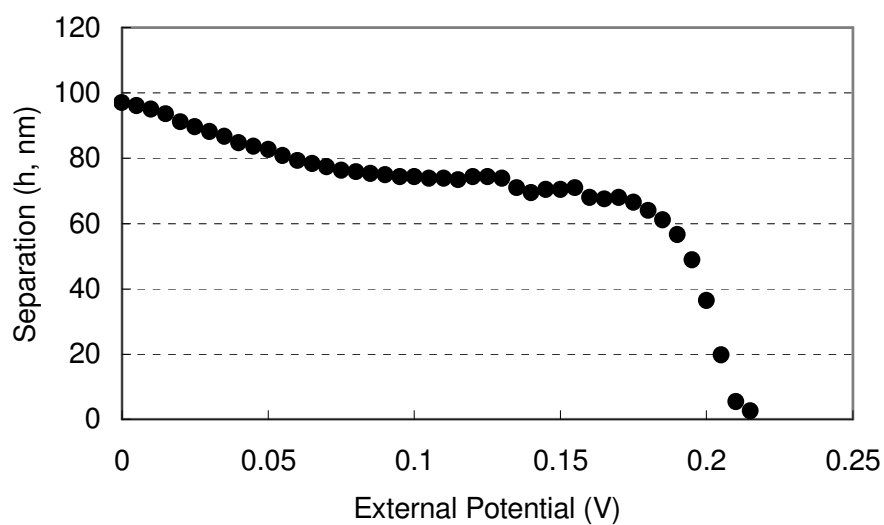
(a)
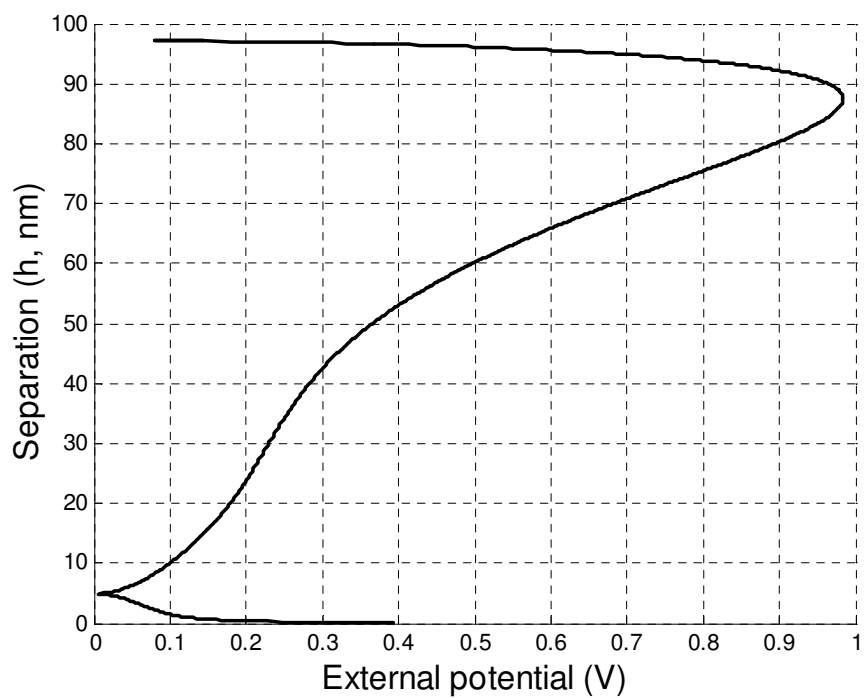
(b)

Fig. 44. The separation-external potential curve in case that $K = 0.2748$ N/m, $h_0 = 97$ nm,

and $R = 2.83$ μm. (a) experimental result, (b) analytical result.
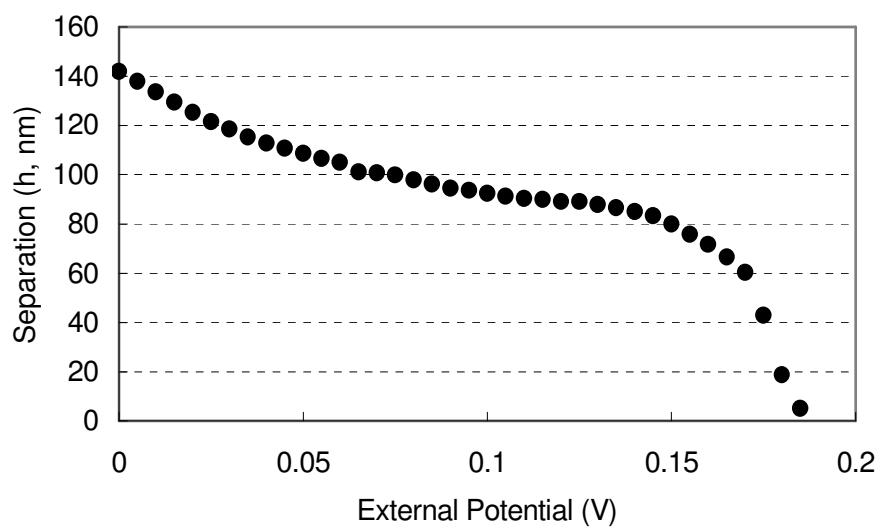
(a)
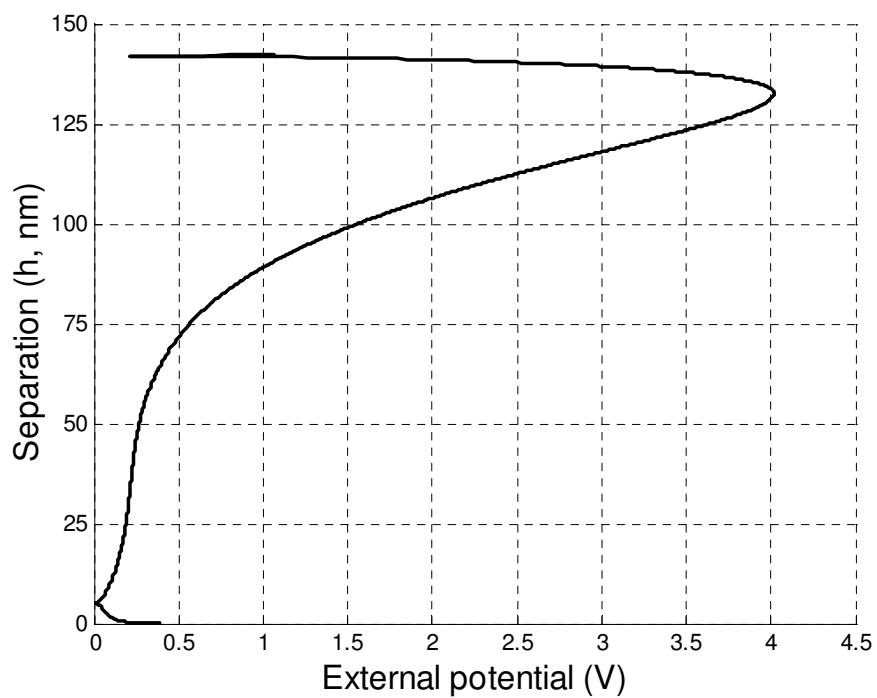
(b)

Fig. 45. The separation-external potential curve in case that $K = 0.1134$ N/m, $h_0 = 142$

nm, and $R = 9.94$ μm. (a) experimental result, (b) analytical result.
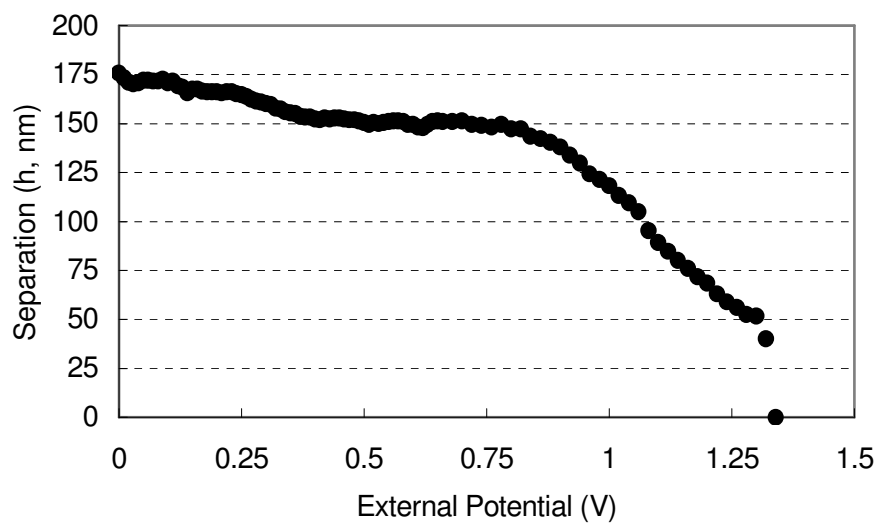
(a)
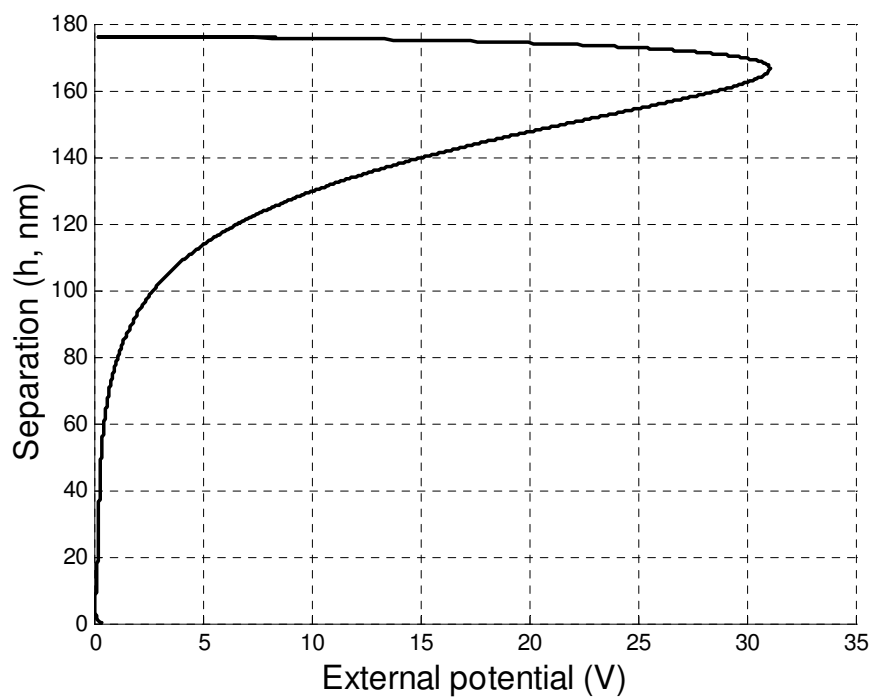
(b)

Fig. 46. The separation-external potential curve in case that $K = 0.2092$ N/m, $h_0 = 176$

nm, and $R = 8.60$ μm. (a) experimental result, (b) analytical result.
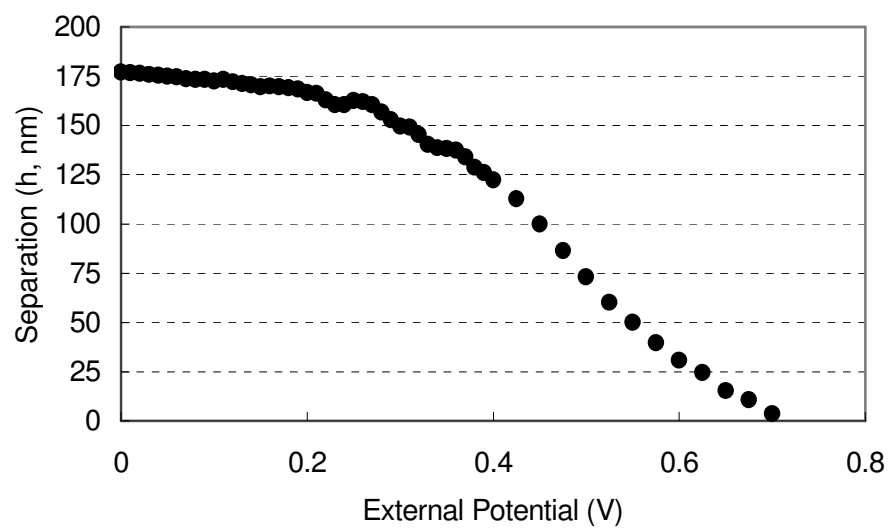
(a)
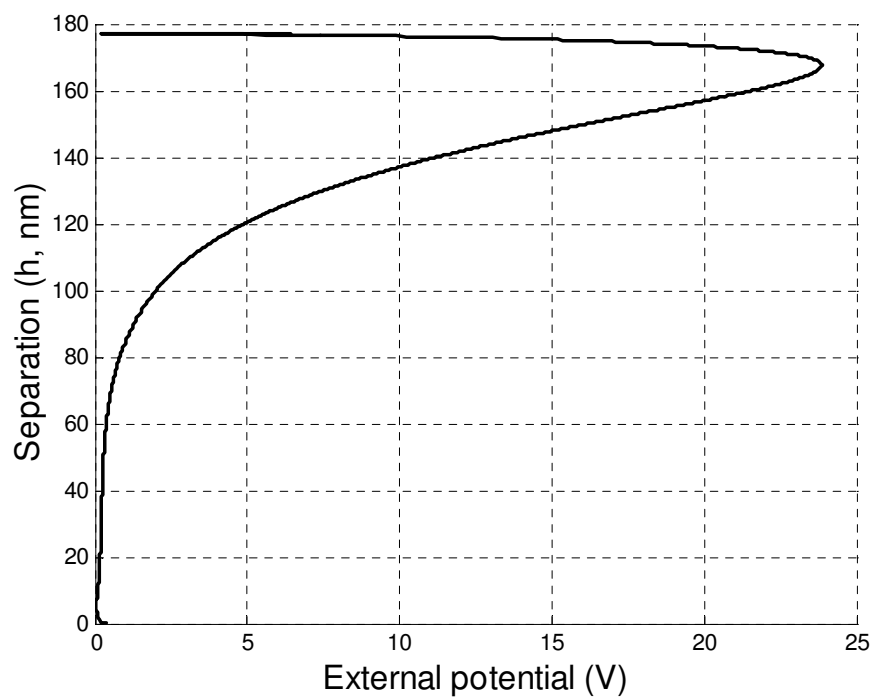
(b)

Fig. 47. The separation-external potential curve in case that $K = 0.1628$ N/m, $h_0 = 177$ nm, and $R = 12.51$ μm. (a) experimental result, (b) analytical result.

In Fig. 44 (a), we measured spring constant of 0.2748 N/m, initial separation between the gold sphere and the flat gold sample of 97 nm, and a radius of gold sphere on the AFM cantilever of 2.83 μm with which we can get the effective area of 1.7 μm^2 using the Langbein approximation. In the experiment, the critical point, where the moving electrode collapses onto the fixed electrode, cannot be found but the point at which the slope changes exists. This point might be the critical point and occurs around the 0.18 V and 64.04 nm. Fig. 44 (b) shows the analytical result on same conditions (K = 0.1134 N/m, R = 2.83 μm, h_0 = 142 nm, A_h = 40×10-20 J for gold-water-gold, $\varepsilon\varepsilon_0$ = 78 for water, and n_∞ = 1 mM) and critical potential of 0.98 V and critical separation of 87.5 nm. In this curve, the solid lines represent the stable equilibrium separations and the dotted lines represent the unstable separations.

In Fig. 45 (a), measured spring constant is 0.1134 N/m, initial separation is 142 nm, and radius of gold sphere on AFM cantilever is 4.97 μm (effective area is 4.4 μm^2). And the slope-changing point is around 0.16 V and 71.65 nm. Fig. 45 (b) shows the critical potential is 4.08 V, and critical separation is 132.4 nm on same condition of experiment.

In Fig. 46 (a), measured spring constant is 0.2092 N/m, initial separation is 176 nm, and radius of gold sphere on AFM cantilever is 4.3 μm (effective area is 4.75 μm^2). And the slop-changing point is around 0.84 V and 143.6 nm. Fig. 46 (b) shows the critical potential is 31.07 V, and critical separation is 166.4 nm.

In Fig. 47 (a), measured spring constant is 0.1628 N/m, initial separation is 177 nm, and radius of gold sphere on AFM cantilever is 6.26 μm (effective area is 7.0 μm^2). And

the slop-changing point is around 0.27 V and 160.48 nm. Fig. 47 (b) shows the critical

potential is 23.86 V, and critical separation is 167.4 nm.

In the same condition, the analytical results show that the critical potential is higher

and the stable separation range from the initial separation to the critical separation is

smaller compared the experimental results. And the critical points of the analytical

results are apparent but those of experimental results are not.

C. Discussion of results

The analytical results were not verified by the experiments. Relative to the analysis,

the experiments did not show distinct critical points, and the experiments showed less

electrode separation for a given applied electric potential. The experiments did show

points at which the separation versus potential plots rapidly changed slope, which may

be instability points. The following discussion will attempt to explain the difference

between the analytical and experimental results.

1) The Poisson-Boltzmann equation

The Poisson-Boltzmann equation assumes an ideal solution, meaning a dilute

solution. But near the electrode there is a very high concentration of ions. In addition,

the Poisson-Boltzmann equation assumes that the ions are infinitesimal points, which are

infinitesimally small. In reality, of course, the ions have some finite size.

The analytical results are based on the linearized Poisson-Boltzmann equation.

However, in Figures 44 (b) though 47 (b), the critical potentials are greater than 200mV,

which is too large for the linear theory to be valid. Approximately 25 mV is the limitation of linearized Poisson-Boltzmann equation.

However, the analysis will deviate from the experiments even more if the nonlinear Poisson-Botlzmann equation is used. With the nonlinear Poisson-Boltzmann equation, the critical potential and critical separation will increase because the double layer interaction force from the nonlinear Poisson-Boltzmann equation is smaller than that from the linearized Poisson-Boltzmann, as indicated in Table I. In Table I, the double layer interaction force is proportional to C + 2 according to $F_E = -n_\infty kTA(C+2)$. C + 2 of the nonlinear Poisson-Boltzmann equation can be obtained using the thesis by Devereux and Bruyn [22] and that of linearized Poisson-Bolzmann equation can be obtained with the solution of linearized Poisson-Boltzmann equation (28) and $C + 2 = \left(\dfrac{d\phi}{dX} \right)^2 - \phi^2$.

Table I. Comparison of C + 2 from the nonlinear Poisson-Boltzmann equation and the linearized P-B equation.

Potential in case ξ = 10 (or n_∞ = 1 mM, $h = 96$ nm)	C + 2	
	General P-B equation	Linearized P-B equation
2.6 mV	0	0.000002
15.5 mV	0.00006	0.000065
25.9 mV	0.00017	0.000182
129.3 mV	0.00209	0.00454
258.6 mV	0.00283	0.018162
517.2 mV	0.00291	0.072646

2) The bulk potential is unknown

In the model, the electrode potentials are applied with respect to the bulk potential, which is assumed to be zero. But in the experiment, the applied electrode potentials are with respect to the Ag/AgCl reference electrode, and the bulk potential is unknown.

3) Surface roughness and asperities

Surface roughness is not taken into account in traditional (Derjaguin-Landau-Verwey-Overbeek) DLVO theory even though most surfaces and colloid particles, including our electrodes, have a certain degree of roughness. As described in a recent review by Walz, divergence between DLVO theory and experiments involving rough particles is often explained by surface roughness [41]. Generally rough surfaces between two conductors make the attractive electrostatic force decrease. So, the double layer interaction force in the analytical study is greater than that in the experiment. But asperities due to conducting particles deposited during evaporation makes electrostatic interaction increase. Therefore we can explain our experimental results not with surface roughness effect but with existence of asperities [41], [42].

4) Hydrophobic effects

Long-range attractive hydrophobic force exists between hydrophobic surfaces. Clean gold is a hydrophilic surface. It has a small contact angle (<70 degrees), meaning that water will spread onto its surface. Therefore, hydrophobic forces were not included in the analytical model. However in the lab, gold surfaces may become hydrophobic because of organic films depositing onto the surface from the environment. So clean

surfaces are hydrophilic, but some gold surface sitting around can become hydrophobic. Gold surfaces cleaned in piranha solution are hydrophilic, but organic films get on the clean gold spontaneously from the air. There are organics in the air and then they stick to the clean gold surface. Also, Biggs in 1994 mentioned that gold surfaces are notoriously hard to clean and during the experiments readsorption of organic contaminant did take place [43]. Therefore, the gold sphere and the flat gold surface may be hydrophobic in our experiment.

The interaction force between hydrophobic surfaces in water has been a debated issue for a long time because the strength and range do not coincide among a large number of experimental data, although the force has been confirmed to be long-ranged and strongly attractive. Much to the wonder of many scientists, ensuing experiments with different types of hydrophobized surfaces generated not only quantitatively different results, but also interactions that were qualitatively different [44]. Doppenschmidt in 1999 observed one surprising result at positive sample potentials. The decay length of the attractive force was significantly larger than the Debye length. Such a large decay length cannot be explained by the double layer interaction force. They suspected that a hydrophobic force acts between surfaces of large contact angle. A possible explanation of the long-range attraction is an indirect hydrophobic effect: It could be possible that the sample became hydrophobic at positive potentials. This could be due to hydrocarbon-containing contaminants, which might selectively absorb at positive potentials. Alternatively, the surface might become hydrophobic due to electrochemical reactions [32]. Two hydrophobic surfaces in water attract each other

over a long-range up to several hundred nm. Highly Oriented Pyrolytic Graphite (HOPG) is hydrophobic. Silicon nitride should be hydrophilic. Even in this unsymmetrical situation (HOPG and silicon nitride) hydrophobic attraction is expected. In addition, any tiny amount of hydrocarbons adsorbed to the surface might cause a significant increase of the hydrophobic attraction. The decay length of roughly 15 nm was significantly larger than the Debye length. Doppenschmidt has yet no explanation or interpretation for this long-range attraction [32]. Raitai in 1996 observed a long-range attractive force between a platinum or gold sample and a silicon nitride tip at high positive potentials. This component could be fitted with an exponential function with typical decay lengths of 50 nm. They have yet no explanation or interpretation for this long-range attraction. Only the long-range hydrophobic force is of significant magnitude at such large separations. At high positive sample potentials the cantilever was bent away from the sample by typically a few tens of nanometers. An attractive force that decayed with the Debye length was never observed in their experiment. Instead, a long-range attraction was observed that could not be explained with Poisson-Boltzmann theory [26]. Hillier in 1996 observed the attractive forces between silica sphere and gold electrode when the electrode is made positive. In 1 mM solutions, the force vs. separation interaction extends past 30 nm separation, while in 10 mM solutions, the interaction force decays within the first 8 nm from the electrode surface. This behavior is consistent with the difference in the calculated Debye length for these solutions, κ^{-1} = 9.62 nm at 1mM and κ^{-1} = 3.04 nm at 10 mM [29]. Ducker and Senden in 1992 found the attractive force between a gold sphere and a flat gold plate at large separation even

though they have same negative charges on their surface. They considered several possible reasons for this: 1) the effective radius may be smaller than the radius of 3.5 μm obtained from SEM, 2) organic material has probably adsorbed at the gold surface, possibly producing hydrophobic interactions, and 3) some of the charge on each surface may be situated at a negative surface separation Although most of the charge on a conducting surface would be concentrated on the asperities, charge on adsorbed material may lie beyond the point of closest approach [40]. Aston and Berg in 2000 observed the long-range attraction between hydrophobic materials in aqueous media has long been exploited in separations. There appears at present to be no established theory that completely explains the collective results in a unified manner. Though a single explanation would be desirable, the most reasonable arguments suggest there may be several 'hydrophobic effects', distinctly different the mechanism for long-range non-DLVO interactions. Significantly long-range attractions are often measured that these seem to be influenced more by surface structure or mobility rather than macroscopic hydrophobicity [45]. Also, Butt in 1995 measured monotonic attractive forces of longer range (100 nm) and greater magnitude than van der Waals forces. These occur between surfaces which generally exhibit high water contact angles (e.g. hydrocarbon and fluorocarbon surfaces) and are usually known as hydrophobic forces [46].

The theoretical understanding of the long-ranged exponentially decaying interaction is still unsatisfactory, although some progress has been made. A current list of possible mechanisms includes solvent structuring (the self-association of water being the most common), dipolar-van der Waals and electrostatic correlation forces, submicroscopic

bridging bubbles, cavitation, bridging macromolecules, and contact region capillary condensates [45].

Submicroscopic bridging bubbles cannot be dismissed as a possible hydrophobic interaction mechanism, where the range of attraction would be essentially fixed by the size of the bubble. A pre-formed bubble can pull two hydrophobic surfaces together in aqueous media. Sufficiently large gas bubbles trapped on submerged surfaces may persist for hours or even months without careful de-aeration, though any bubbles of colloidal dimensions are predicted to dissolve within microseconds and could not be a cause for attraction [45]. As for hydrophobized surfaces dried in air, it was found recently that nanobubbles are attached to surfaces and cannot be removed completely by immersing them in water. When two surfaces are so close that bubbles remaining on surfaces coalesce each other a gas bridge will be formed between them like Fig. 48. The long-range and strong attraction is then generated between surfaces, because of the surface tension at the gas-water interface and the low gas pressure [44].

Tyrrell in 2001 obtained images of nanobubbles on hydrophobic glass surfaces in water with tapping mode AFM (Atomic Force Microscopy). These images show that these hydrophobic surfaces are covered with soft domains, apparently nanobubbles which have a radius of curvature of the order of 100 nm, and height above the substrate of 20 – 30 nm. Also they estimated the adhesion of these nanobubbles as 64 – 102 nN from the jump-out distance of the retract force curves. This is consistent with a capillary adhesion for a bubble between a flat and a sphere with contact angles of 101° and 80°-82° respectively. So, these images coupled with force curves provide powerful evidence

of the existence of nanobubbles and of their bridging as the cause of the long-range attractions measured between macroscopic hydrophobic surfaces [47].
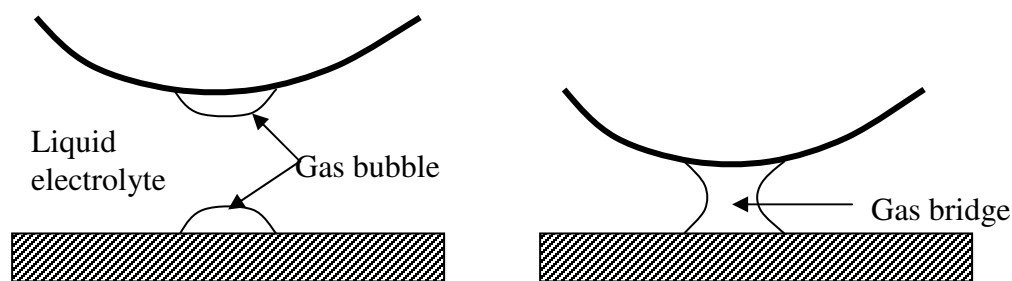
Fig. 48. Formation of gas-bridge.

Generally, the roughness of the gold substrate causes scatter in the adhesion data, because the effective surface area upon contact varies over the surfaces due to presence of the gas-bridge, but it might also have implications for the hydrophobic forces. The effect of roughness on the interactions between hydrocarbon layers covalently attached to the gold has been discussed previously, with particular emphasis on the role of surface imperfections at grain boundaries as nucleation sites or traps for gas bubbles. The surface imperfections might work more like traps for air bubbles, rather than as bubble nucleation sites [36]. At present there is no clear understanding of the mechanism of these forces. The large magnitude and range and the lack of theoretical understanding make the study of hydrophobic forces important in surface science.

Christenson and Claesson in 1988 suggest that the results of long-range attractive hydrophobic force can be ordered in the following three major categories: 1) strongly attractive forces between stable surfaces, 2) attractions of varying strength and range

caused by bridging of bubbles, and 3) long-range attractive forces with exponential decay. The surfaces are stable and have high contact angles (generally $\langle$ 100°), but the variation of the force onset separation with distance is significant, from about 10 nm to about 200 nm. Even though the Poisson-Bolzmann theory predicts the same decay length for repulsive and attractive electrostatic force, a significantly longer decay length in the attractive regime observed [36].

First, the long-range attractive hydrophobic force makes the critical separation smaller than the critical separation without hydrophobic forces (Fig. 49). In Fig. 49, F_s is the elastic spring force, F_E is the double layer interaction force, F_{vdw} is the van der Waals force, and F_{lrh} is the long range hydrophobic force. Below the critical potential, there are two intersections of the elastic spring force and other external forces. These two intersections are equilibrium points; one near the initial separation is stable the equilibrium point and another far away from the initial separation is the unstable equilibrium point. Fig. 49 (a) shows the short decay length of the summation of double layer interaction force and van der Waals force from the analytical study. This short decay length is the Debye length and this phenomenon makes the stable region of the free electrode from the initial separation to critical separation short even though the critical potential is high. But Fig. 49 (b) shows the long-range decay length of the summation of the double layer force, van der Waals force, and long-range hydrophobic force. According to some literature, this long-range length is from several tens of nanometer to several hundreds nanometers. This situation makes the critical separation at the lower critical potential far away from the initial separation and the stable region of

free electrode larger. This phenomenon can explain why all our experimental results

have the much larger stable region from the initial separation to critical separation than

that of analytical results.
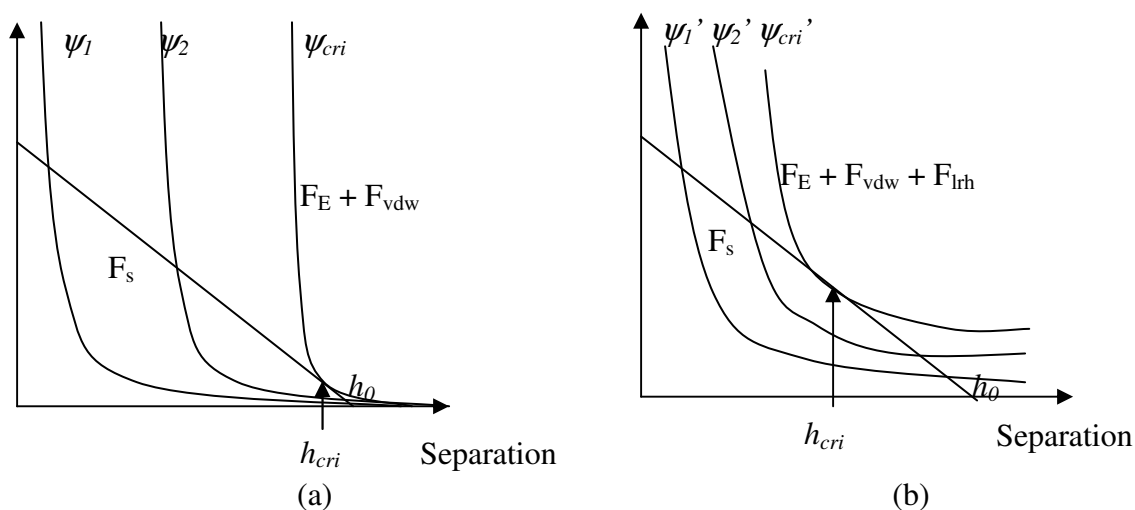
Fig. 49. (a) Short decay length (analysis) and (b) large decay length with strong

attractive force (experiment).

Second, there exists another "strong" attractive force (long-range strong attractive

hydrophobic force) in the experiment. That means critical points can occur with the

small summation of double layer interaction force and van der Waals force and this

means critical points can occur with small external potential because of long-range

"strong" attractive hydrophobic force. So, the critical potential, ψ_{cri}', in the experimental

results is much smaller than the critical potential, ψ_{cri}, in the analytical results like Fig.

49. This phenomenon and long-range decay phenomenon can explain the reason our

experimental results have much smaller critical potentials than those of analytical results.

5) Van der Waals force

Generally speaking, the charging mechanism of the gold surface probably depends on how the gold surface was prepared and cleaned, and on solution conditions and the presence of impurities. The lack of an abrupt collapse of the separation in the experiment may be due to a weaker than expected van der Waals force. Because of the limited thickness of the gold films, the van der Waals attraction between these surfaces is much lower than between bulk gold objects [34]. Most probably the van der Waals forces are obscured by non-DLVO short-range interactions, in particular repulsive hydration forces, and by surface roughness effects. These repulsive forces at small separation also might play a role in disappearance of collapsing two electrodes in unstable region.

IV. CONCLUSIONS AND FUTURE WORK

A.   Conclusions

The objective of this dissertation is to analytically model a parallel plate electrostatic actuator operating in a liquid electrolyte and experimentally verify the analysis.

The analytical model consisted of an electrochemical force derived from the linearized Poisson-Boltzmann equation, a linear spring force, and van der Waals force. The electrode separation versus applied electric potential is a function of the non-dimensional spring constant K^*, non-dimensional separation ξ_0, and non-dimensional Hamaker constant A_h^*.

1. The non-dimensional spring constant K^* has no effect on the critical separation. The critical potential is proportional to the square root of K^*.

2. The critical separation and critical potential increase as the non-dimensional separation ξ_0 increases.

3. The critical separation increases and the critical potential decreases as the non-dimensional Hamaker constant A_h^* increases.

4. The free electrode has a small stable displacement relative to their initial electrode separation. Thus, it may be impossible to effectively use parallel plate electrostatic actuators in liquid electrolytes.

5. The maximum stored energy in the system occurs at the critical point where the potential applied to the two electrodes is maximum and the separation between two electrodes is minimum in the stable region.

6. The maximum stored energy increases as the non-dimensional separation ξ_0 increases and the non-dimensional Hamaker constant $A_h{}^*$ decreases. The non-dimensional spring constant has no effect on the maximum stored energy.

The analytical results were not verified by the experiment. Relative to the analysis, the experiments did not show distinct critical points, and the experiments showed less electrode separation for a given applied electric potential. The experiments did show points at which the separation versus potential plots rapidly changed slope, which may be instability points.

This phenomenon may be due to long-range attractive hydrophobic forces which exist in the experiment, but not in the model. Although clean gold surfaces are hydrophilic, gold surfaces may become hydrophobic due to impurities. For hydrophobized surfaces dried in air, nanobubbles could be attached to the surfaces. When two surfaces are so close that bubbles on the surfaces coalesce, a gas bridge will be formed between them. The long-range and strong attraction could be then generated

between surfaces, because of the surface tension at the gas-water interface and the low gas pressure.

B. Future work

Future work should consider the following ways to make the model more closely match the experiment:

1) The model should include chemical potentials for non-ideal solutions.

2) The model should include a numerical solution of the nonlinear Poisson-Boltzmann equation.

3) The model should include the effects of finite ion size.

4) The model should include the effects of attraction between hydrophobic surfaces.

Future experiments should:

1) Ensure than the gold electrode surfaces are hydrophilic during use.

2) Develop a method to ensure that no gas remains on the electrode surfaces.

3) Attempt to measure the electric potential of the bulk electrolyte during the experiment.

In general, the research reported herein in near the limit of the contributions that can be made by someone with a classical continuum mechanics education. Future work towards designing electrostatic actuators to work in liquid electrolytes should be performed with a team consisting of persons with the following skills: continuum mechanics, electrochemistry, and molecular hydrodynamics.

REFERENCES

[1] H. Helvajian, *Microengineering Aerospace Systems*, El Segundo, CA: The Aerospace Press, 1999.

[2] T. Tsuchiya, and H. Funabashi, "A z-axis differential capacitive SOI accelerometer with vertical comb electrodes," *Sensors and Actuators*, vol. A116, pp. 378-383, Jul. 2004.

[3] Sandia National Laboratories, "An example of micro electrostatic actuator," [Online]. Available: http://mems.sandia.gov/.

[4] D. Hah, S. T. Huang, J. Tsai, H. Toshiyoshi, and M. C. Wu, "Low-voltage, large-scan angle MEMS analog micromirror arrays with hidden vertical comb-drive actuators," *J. of Microelectromechanical Syst.*, vol 13, no. 2, pp. 297-289, Apr. 2004.

[5] H. D. Nguyen, D. Hah, P. R. Patterson, R. Chao, W. Piyawattanametha, E. K. Lau, and M. C. Wu, "Angular vertical comb-driven tunable capacitor with high-tuning capabilities," *J. of Microelectromechanical Syst.*, vol 13, no. 3, pp. 406-413, Jun. 2004.

[6] D. L. Dickensheets and G. S. Kino, "Silicon-micromachined scanning confocal optical microscope," *J. of Microelectromechanical Syst.*, vol. 7, no. 1, pp. 38-47, Mar. 1998.

[7]   M. Douglass, "DMD reliability: A MEMS success story," in Proc. SPIE, San Jose, CA, Jan. 27,, 2003, pp. 1-11.

[8]   Texas Instruments, "Three pictures of DLP (Digital Light Processing)," [Online]. Available: http://www.dlp.com/.

[9]   O. Bochobza-Degani, E. Socher, A. Lipson, T. Leitner, D. J. Setter, S. Kaldor, and Y. Nemirovsky, "Pull-in study of an electrostatic torsion microactuator," *J. of Microelectromechanical Syst.*, vol. 7, no. 4, pp 373-379, Dec. 1998.

[10]   Y. Nemirovsky, and O. Bochobza-Degani, "A methodology and model for the pull-in parameters of electrostatic actuators," *J. of Microelectromechanical Syst.*, vol. 10, no. 4, pp. 601-615, Dec. 2001.

[11]   O. Bochobza-Degani, and Y. Nemirovsky, " Modeling the pull-in parameters of electrostatic actuators with a novel lumped two degrees of freedom pull-in model," *Sensors and Actuators*, A97-98, pp. 569-578, Nov. 2002.

[12]   O. Bochobza-Degani, and Y. Nemirovsky, "Design considerations of rectangular electrostatic torsion actuators based on new analytical pull-in expressions", *J. of Microelectromechanical Syst.*, vol. 11, no. 1, pp. 20-26, Feb. 2002.

[13]   O. Bochobza-Degani, and Y. Nemirovsky, "Experimental verification of a design methodology for torsion actuators based on rapid pull-in solver," *J. of Microelectromechanical Syst.*, vol. 13, no. 1, pp. 121-130, Feb. 2004.

[14]   P. Kim, and C. M. Lieber, "Nanotube Nanotweezers," *Science*, vol. 286, pp. 2148~2150, Dec. 1999.

[15] S. Akita, and Y. Nakayama, "Nanotweezers consisting of carbon nanotubes operating in an atomic microscope," *Appl. Phys. Lett.*, vol. 79, no. 11, pp. 1691-1693, Sept. 2001.

[16] M. Dequesnes, S. V. Rotkin, and N. R. Aluru, "Calculation of pull-in voltages for carbon-nanotube-based nanoelectromechanical switches," *Nanotechnology*, vol. 13, pp. 120-131, Jan. 2002.

[17] T. L. Sounart and T. A. Michalske, "Electrostatic actuation without electrolysis in microfluidic MEMS," in *Proc. 12th International Conf. Solid State Sensors, Actuators, and Microsystems*, Boston, MA, Jun. 8-12, 2003, pp. 615-618.

[18] A. J. Bard and L. R. Faulkner, *Electrochemical methods: Fundamentals and Applications*, New York: John Wiley & Sons, Inc., 2001.

[19] W. B. Russel, D. A. Saville, and W. R. Schowalter, *Colloidal Dispersions*, Cambridge: Cambridge University Press, 1989.

[20] J. Israelachvili, *Intermolecular and Surface Forces*, New York: Academic Press, 1992.

[21] B. V. Derjaguin, "A theory of the heterocoagulation, interaction and adhesion of dissimilar particles in solutions of electrolytes," *Discuss, Faraday Soc.*, vol. 18, pp. 85-98, Aug. 1954.

[22] O. F. Devereux, and P. L. de Bruyn, *Interaction of Plane-Parallel Double Layers*, Ph.D. dissertation, M.I.T. Press, Boston, Aug. 1963.

[23] R. Hogg, T. W. Healy, and D. W. Fuerstenau, "Mutual coagulation of colloidal dispersions," *Trans. Faraday Soc.*, vol. 62, pp. 1638-1651, Sep. 1965.

[24] E. J. W. Verwey and J. T. G. Overbeek, *Theory of the Stability of Lyophobic Colloids*, Mineola, New York: Dover Publications, Inc., 1999.

[25] M. H. Nayfeh, and M. K. Brussel, *Electricity and Magnetism*, New York: John Wiley & Sons, 1985.

[26] R. Raitai, M. Grattarola, and H. Butt, "Measuring electrostatic double layer forces at high surface potentials with the atomic force microscope," *J. Phy. Chem.*, vol. 100, pp. 16700-16705, Jul. 1996.

[27] R. Raitai, M. Preuss, M. Grattarola, and H. Butt, "Preliminary results on electrostatic double layer force between two surfaces with high surface potentials," *Colloids and Surfaces*, vol. 136, pp. 191-197, Oct. 1998.

[28] T. Ishino, H. Hieda, K. Tanaka and N. Gemma, "Electrical double-layer forces measured with an atomic force microscope while electrochemically controlling surface potential of the cantilever," *Jpn. J. Appl. Phys*, vol. 33, pp. 1552-1554, Oct. 1994.

[29] A. C. Hillier, S. Kim, and A. J. Bard, "Measurement of double-layer forces at the electrode/electrolyte interface using the atomic force microscope: Potential and anion dependent interactions," *J. Phys. Chem.*, vol. 100, pp. 18808-18817, Aug. 1996.

[30] T. Arai, and M. Fujihira, "Effect of tip shape on force-distance curves for AFM in aqueous electrolytes," *J. of Electroanalytical Chem.*, vol. 374, pp. 269-273, May 1994.

[31] J. Frechette and T. K. Vanderlick, "Double layer forces over large potential ranges as measured in an electrochemical surface forces apparatus," *Langmuir*, vol. 17, pp. 7620-7627, Sep. 2001.

[32] A. Doppenschmidt and H. Butt, "Measuring electrostatic double-layer forces on HOPG at high surface potentials," *Colloids and Surfaces*, vol. 149, pp. 145-150, Jun. 1999.

[33] D. Barten, J. M. Kleijn, J. Duval, H. P. Leeuwen, J. Lyklema, and M. A. Stuart, "Double layer of a gold electrode probed by a AFM force measurements," *Langmuir*, vol. 19, pp. 1133-1139, Oct. 2003.

[34] M. Giesbers, J. M. Kleijn, and M. A. Stuart, "The electrical double layer on gold probed by electrokinetic and surface force measurements," *J. of Colloid and Interface Science*, vol. 248, pp. 88-95, Feb. 2002.

[35] J. Wang and A. J. Bard, "Direct atomic force microscopic determination of surface charge at the gold/electrolyte interface-the inadequacy of classical GCS theory in describing the double layer charge distribution," *J. Phys. Chem. B*, vol. 105, pp. 5217-5222, Jan. 2001.

[36] T. Ederth, "Substrate and solution effects on the long-range "Hydrophobic" interactions between hydrophobized gold surfaces," *J. Phys. Chem. B*, vol. 104, pp. 9704-9712, Jul. 2000.

[37] M. Giesbers, *Surface Forces Studied with Colloidal Probe Atomic Force Microscopy*, Ph.D. dissertation, Wageningen University, Jun. 2001.

[38] J. P. Cleveland, S. Manne, D. Bocek, and P. K. Hansma, "A nondestructive method for determining the spring constant of cantilever for scanning force microscopy," *Rev. Sci. Instrum.*, vol. 64, pp. 403-405, Oct. 1993.

[39] T. G. Beckwith, N. L. Buck, and R. D. Marangoni, *Mechanical Measurements,* New York: Addison-Wesley, Inc., 1982.

[40] W. A. Ducker and T. J. Senden, "Measurement of forces in liquids using a force microscope," *Langmiur*, vol. 8, pp. 1831-1836, Apr. 1992.

[41] J. Y. Walz, "The effect of surface heterogeneities on colloidal forces", *Adv. Colloid Interface Science*, vol. 74, pp. 119-168, 1998.

[42] T. R. Anthony, "Anodic bonding of imperfect surface," *J. Appl. Phys.*, vol. 54, pp. 2419-2428, Jan. 1983.

[43] S. Biggs and P. Mulvaney, "Measurement of the forces between gold surfaces in water by atomic force microscopy," *J. Chem. Phys.*, vol. 100, pp. 8501-8505, Feb. 1994.

[44] N. Ishida, N. Sakamoto, M. Miyahara, and K. higashitani, "Static method to evaluate interaction forces by AFM," *J. of Colloid and Interface Science*, vol. 235, pp. 190-193, Sep. 2001.

[45] D. E. Aston, and J. C. Berg, "Long-range attraction between silanated silica materials studied by an electrolyte titation with atomic force microscopy," *Colloids and Surfaces*, vol. 163, pp. 247-263, Jun. 2000.

[46] H. Butt, M. Jaschke, and W. Ducker, "Measuring surface forces in aqueous electrolyte solution with the atomic force microscope," *Bioelectrochemistry and Bioenergetics*, vol. 38, pp. 191-201, Jun. 1995.

[47] J. W. G. Tyrrell and P. Attard, "Images of nanobubbles on hydrophobic surfaces and their interactions," *Physical Review Letters*, vol. 87, no. 17, pp. 176104-1 – 176104-4, Oct. 2001.

VITA

Doyoung Kim was born in Jongno-gu, Seoul, South Korea on August 23, 1970, the son of Jongsun Kim and Youngsoon Choi. He graduated from Posong High School in February 1989. In March of 1991, He entered Korea University in Seoul and received a Bachelor of Science degree in mechanical engineering in August 1996. In February 1997, he entered the graduate school of Korea University in mechanical engineering and received a Master of Science degree in February 1999. The following May, he was employed by Samsung Advanced Institute of Technology (SAIT) as an assistant researcher. He joined the Department of Aerospace Engneering at Texas A&M University and received his Doctor of Philosophy in December 2005.

His permanent address is: Tanhyun-dong, Tanhyun APT. #1201, Koyang-shi, Kyounggi-do, South Korea.